**Hybrid Quantum-Classical Simulation of Silicon Based Material
on Parallel Machine and Visualization Tool**

（並列計算機を用いたシリコン系材料の
ハイブリッド量子古典シミュレーションと
可視化ツール）

Takahisa Kouno

2018

Abstract

With the recent significant development of computers, the use of computer simulation is rapidly spreading not only to basic research fields such as bio, material, fluid, and structure, but also to industrial application fields. Supercomputers are state-of-the-art numerical computing machines for science and technology. Due to various constraints relating to hardware and materials, the majority of supercomputers are shifting to the distributed memory type. And multi-core CPUs and many-core accelerators are progressively used. Such supercomputers are often called as the massively parallel type. The development of novel simulation methods that can utilize the massively parallel supercomputer is highly expected. In particular, the technique utilizing the real space grid instead of the wavenumber space has attracted wide attention recently because it can achieve high parallelism on the massively parallel machine.

In atomistic simulation of materials, either the classical molecular dynamics method using empirical interatomic force or the first-principles molecular dynamics method using the atomic force obtained by performing electronic state calculation every step is usually used. In the case of the electronic state calculation, the scope of the applicable target systems is wide and highly accurate, but the required calculation times can be huge. Hence, a long-term simulation of a system with chemical reactions is often difficult even using a supercomputer. The hybrid quantum-classical simulation method that we used in this thesis is designed so that the target system is divided into regions and either the electronic state calculation or the classical calculation is assigned to each region in parallel. This hybrid method is unique in that it can simulate large-scale systems with high accuracy. In this thesis, the hybrid quantum-classical simulations are executed on supercomputers for two themes that are interested in industries. We visualize the complex output data using our original software, to find new microscopic mechanisms.

The hybrid quantum-classical simulation method can be stated as a new type of the molecular dynamics one composed of different types of domains: one for the classical molecular dynamics calculation and another for the electronic state calculation. For the hybrid quantum-classical simulation, we introduce a new data format suitable to visualization and software development. The resultant data in the hybrid quantum-classical simulation consist of the particle data representing atoms and ions and the grid data representing electron density. It is necessary to efficiently handle and visualize these data sets with different characters. In the past, the particle data and lattice point data are

often handled separately. Such a handling is not suited to the hybrid quantum-classical simulation. In order to solve this problem, a file format that combines particle and lattice data is proposed. Furthermore, we develop a visualization software that reads and visualizes the file. We use this visualization software for the data analysis of the hybrid quantum-classical simulation and find (1) and (2) explained below.

(1) As device miniaturization advances, stress caused by defects and structures in the crystal has a greater influence on the entire system. A hybrid quantum-classical simulation studied the diffusion of oxygen atoms in silicon crystals as to how the external stress field changes the electronic state and further influences the physical property value. In order to reproduce a realistic stress field, a relatively large-scale silicon system is required. Also, an oxygen atom in the silicon crystal migrates while recombining bonds. In the hybrid quantum-classical method, the oxygen atom and its surrounding region are calculated by electron density functional calculation method, and in other regions, classical atomic structure is calculated, and both regions are dynamically connected and simulated simultaneously and in parallel did. In addition, the nudged elastic band method was used to obtain the minimum energy path of oxygen atom diffusion. Based on the simulation results, we found that the diffusion barrier energy of oxygen atom varies depending on the strain direction of silicon type and the magnitude of strain.

(2) High purity silica (SiO_2) glass is a material with high durability and mechanical strength. In addition, it is used as an industrially important material such as optical fiber and semi-permanent storage device due to characteristics such as optical characteristics and heat resistance. SiO_2 glass has relatively high water resistance, but many Si-OH is produced by reaction between water molecule and Si-O bond, and characteristics change. Therefore, it is important to theoretically understand the conditions and reaction process of Si-O bond breaking by water molecules. We simulated the Si-O bond breaking reaction by water molecules in SiO_2 glass using hybrid quantum-classical simulation. In the case of compression, Si-O bond breaking reaction was observed by water molecules in the dimer state. It was found that the bond breaking reaction occurred in three processes of Si-O bond breaking reaction of SiO_2 glass by water molecules. (i) Proton transfer occurs between two water molecules in the dimer state. Is adsorbed to Si, and five-coordinated Si is produced. (ii) Si-O bond of five-coordinated Si breaks. (iii) react with O of Si-O where the bond breaks. On the other hand, in the water molecule in the monomer state, no reaction of bond breaking occurred. Examining the

barrier energy of the bond breaking reaction of the Si-O bond by water molecule, it was found that the barrier energy at the time of water molecule in the dimer state is smaller than that at the time of water molecule in the monomer state. It was also found that the barrier energy is reduced by compression. Finally, the diffusion of water molecules in the SiO_2 glass was investigated from the void distribution in the glass. From the visualization results of the voids, it is considered that the voids in the SiO_2 glass are large in size and the voids are connected, so that the water molecules diffuse inside and become a dimer state.

Contents

1 Introduction

With the rapid development of computers in recent years, the use of computer simulation is rapidly spreading not only to basic research fields such as bio, material, fluid, and structure, but also to industrial application fields. Supercomputers, which are leading edge computers for science and technology, have changed to memory-distributed parallel computers in order to obtain higher calculation performance. In recent years, supercomputers have been changing to a massively parallel architecture as the use of CPUs and accelerators equipped with multi-core and many-core in the node computer. Development of a simulation method that can utilize the supercomputer having this new architecture is expected. Particularly, the technique using the real space grid is attracting wide attention because it can achieve high parallelism with the distributed memory type supercomputer.

In the atomistic simulation on materials, either classical molecular dynamics method using empirical interatomic force or first principle molecular dynamics method using atomic force obtained by performing electronic state calculation every step is usually used. In the electronic state calculation, the scope of the applicable target system is wide and it is highly accurate, but since it requires a large amount of calculation, long-term simulation including large scale reactions and chemical reactions is often difficult even using supercomputer.

The hybrid quantum classical simulation method which I use in this research is a method to simulate particle dynamics by applying electronic state calculation or classical molecular dynamics calculation to a divided region in a divided target system. It is unique that we can simulate the dynamics of large atomic systems with high precision of electronic level. In Chapter 2, an algorithm for stably obtaining temporal evolution of the particle groups from the force acting on many atoms and ions will be described in detail including its accuracy.

In the hybrid quantum classical simulation, we set the region where the temporal change of the electronic state is large in the target system to the "quantum" region where electrons are directly calculated by the density functional method (DFT). Other area is classical region.

In research to investigate chemical reaction dynamics, it is necessary to simulate several tens of thousands of steps or to simulate many cases with different

settings, and it is necessary to speed up the simulation code. In the hybrid quantum classical simulation, the DFT applied to the quantum domain requires calculation time several orders of magnitude longer than the calculation time of the classical domain. the speed-up of DFT calculation leads to faster hybrid quantum classical simulation. In general, in order to speed up the calculation on a supercomputer, it is necessary to consider not only the operation but also the memory access and the inter-node communication. In Chapter 3, we explain the outline of the DFT method and the speeding technique applied to the standard orthogonalization by the Gram-Schmidt method of the electron orbital function, which is particularly computationally intensive. We will also describe the technique for speeding up the differential calculation by the difference method introduced in the DFT using the real space grid.

Due to the development of computers, numerical data obtained by computer simulation is enormous. It is necessary to make input and output data easy to understand for human beings, and support software such as visualization is important. In the hybrid quantum classical simulation described above, the target system is divided into regions, and it consists of an area to which the electronic state calculation is applied and a domain to which the classical interaction calculation is applied. In the electronic state calculation, data on ions and fixed grid points related to electron density are outputted, and classical interaction calculation outputs atoms data. It is necessary for analysis to visualize these two types of data collectively.

In hybrid quantum classical simulation, it is important to connect the quantum domain and the classical domain in a seamless manner. In chapter 4, the buffered cluster method used in this study will be explained.

It is not easy to use existing visualization software for this use. Visualization with proprietary software is useful for elucidating the microscopic mechanism from the result of hybrid quantum classical simulation. I made easy to analyze hybrid quantum classical simulation by developing a new data format for hybrid quantum classical simulation and developing software to visualize it using that data format. In chapter 5, we will explain this visualization software developed independently.

Two cases applying the hybrid quantum classical simulation are described in Chapter 6 and Chapter 7, respectively. One is the evaluation of the diffusion of oxygen atoms in the Si crystal, and the other is the bond breaking reaction by the water molecules in the silica glass. In these studies, we performed a large-scale simulation using the hybrid

quantum classical simulation method, taking into consideration the influence such as distortion which could not be done by a small system so far.

[Application 1] As the miniaturization of devices such as semiconductors has progressed, the influence of the stress due to defects and structures in the crystal on the entire system has become greater. A simulation using a computer studied diffusion of oxygen atoms in the silicon crystal as to how the external stress field changes the electronic state and further influences the physical property value. In order to reproduce a realistic stress field, a relatively large-scale silicon system is required. Oxygen atoms in the Si crystal migrate while recombining O-Si bonds.

It is difficult to accurately represent this reaction using classical interactions. When handling chemical bonds, electronic state calculation is required. However, it is not practical to calculate the electronic state in terms of computational resources to apply it to a large-scale system like this research. I want to make the size of the system that calculates the electronic state small. Therefore, using the hybrid quantum classical simulation method, the electron density functional theory calculation is applied to the oxygen atoms and their peripheral regions, and the calculation of the classical atomic structure is applied to the other regions. We simulate the diffusion of oxygen atoms in a large-scale system by dynamically connecting these regions and computing them simultaneously and in parallel. In diffusion of oxygen atoms, the diffusion path of oxygen atoms in the Si crystal and its barrier energy are clarified using the Nudged Elastic Band (NEB) method in order to find the minimum energy path, and the dependence of diffusion on strain is investigated.

[Application 2] High purity silica glass is a material with high durability and mechanical strength. Further, it is used as an industrially important material such as optical fiber and semi-permanent storage device due to characteristics such as optical characteristics and heat resistance. Silica glass has relatively high water resistance. However, reaction of water molecules with Si-O bonds produces more Si-OH and the properties of the glass change. Therefore, it is important to theoretically understand the conditions and reaction processes of Si-O bond destruction by water molecules. In the simulation study of the reaction between SiO_2 and water molecules, a simulation using a relatively small system has been carried out. It is a study using a small periodic system or molecular model. In such a small system, it is considered that the random structure of SiO_2 glass is restricted and it is considered that the reaction with water molecules has the

influence of the strain of SiO_2 glass structure. In such a system, it is considered difficult to estimate the reaction with water molecules correctly. In this study, we simulate the reaction of bond breakage with water molecules in large scale SiO_2 glass. In order to simulate the reaction between SiO_2 glass and water molecules in large-scale SiO_2 glasses, a hybrid quantum classical simulation was carried out. In the hybrid quantum classical simulation, the electronic state calculation using the density functional method was performed in the peripheral region of the water molecule where the bond breakdown reaction occurs in the large scale SiO_2 glass system, and the classical interaction was used for the remaining region. By the simulation of this research, we will clarify the conditions and reaction process of the bond breakdown reaction by water molecules in silica glass.

2 Molecular Dynamics Simulation Method

2.1 Time Evolution Algorithms

Assume an ordinary differential equation with a given initial value for a variable must be solved numerically. The well-known Euler method or the fourth-order Runge-Kutta method could be used. However, in general, such a method is not suited for the time evolution problem of atoms that follow Newton's equation of motion in molecular dynamics (MD) simulation. The proper method for MD simulation should have the following features: (i) the ability to treat a large number of variables, which are in proportion to the number of atoms in a target system; (ii) the smallest number of force calculations per time step possible, i.e., one, because the force calculation is usually the most time-consuming part; (iii) high precision for both a single time step and long-time evolution; and (iv) uses a small amount of memory for the computer simulation. These features preclude the use of the fourth-order Runge-Kutta method, which requires five times the number of force calculations per time step and shows poor long-time stability. In recent years, the Verlet method, with accuracy comparable to that of the Runge-Kutta method (see below) despite the one force calculation per time step, has usually been used. In addition, its time reversibility provides long-time stability.

In section 2.1.1, we present a simple derivation of the Verlet method. In section 2.1.2, the velocity-Verlet method is rederived using the Liouville operator method in the statistical mechanics. The rederivation shows that the velocity-Verlet method preserves time reversibility and symplecticness. The atomic positions have the same trajectory in both the Verlet and the velocity-Verlet method; however, their orders of error appear to be different. In section 2.1.3, we explain the apparent contradiction.

2.1.1 Simple derivation of Verlet and velocity-Verlet methods

We derive the Verlet method using a Taylor expansion with time-step size h. The Taylor expansions of position $r(t)$ of an atom at time $t + h$ and $t - h$ are given by

$$r(t + h) = r(t) + hv(t) + \frac{h^2}{2}\frac{F(t)}{m} + \frac{h^3}{6}\dddot{r} + O(h^4), \tag{2.1}$$

$$r(t - h) = r(t) - hv(t) + \frac{h^2}{2}\frac{F(t)}{m} - \frac{h^3}{6}\dddot{r} + O(h^4). \tag{2.2}$$

Terms after $(h^3/6)\dddot{r}$ are represented by $O(h^4)$ as an order of error. Adding and subtracting equations (2.1) and (2.2) yields

$$r(t + h) = 2r(t) - r(t - h) + h^2\frac{F(t)}{m} + O(h^4), \tag{2.3}$$

$$v(t) = \frac{[r(t + h) - r(t - h)]}{2h} + O(h^2). \tag{2.4}$$

This is the Verlet method. Adding equations (2.1) and (2.2) cancels out the term $(h^3/6)\dddot{r}$, so the term $O(h^3)$ disappears. Thus, the order of error per step in the atomic position is $O(h^4)$. On the other hand, the order of error per step in the update of the velocity is $O(h^2)$. These errors are due to the truncation error of the Taylor expansion.

Equation (2.3) shows that the Verlet method evolves time by updating only the atomic position. The calculation of the next position of an atom involves the positions $r(t)$ and $r(t - h)$, where the atomic velocity is unnecessary. However, an actual simulation requires the kinetic energy to evaluate the total energy and other parameters, and the atomic velocity must be calculated. In addition, the velocity is updated at a time shifted by h as opposed to updating the position, which is difficult to use. It is difficult to provide the initial positions $r(t)$ and $r(t - h)$ of atoms at the start of the simulation.

The order of error $O(h^n)$ represents a truncation error, i.e., an error on the order of n to the time-step size h. As h decreases, the truncation error decreases on the order of h^n. When h is 0.1, the error $\leq(0.1)^n$.

Next, we present a simple derivation of the velocity-Verlet method, which is an improvement on the Verlet method, by converting the Taylor expansions of the Verlet method. The velocity-Verlet method is as accurate as the Verlet method, easy to use, and widely used in MD simulation.

The Taylor expansions of the atomic position $r(t)$ and velocity $v(t)$ at time $t + h$ are

$$\tag{2.5}$$

$$r(t + h) = r(t) + hv(t) + \frac{h^2}{2}\frac{F(t)}{m} + O(h^3),$$

$$v(t + h) = v(t) + h\frac{F(t)}{m} + \frac{h^2}{2}\frac{\dot{F}(t)}{m} + O(h^3).$$

(2.6)

Equation (2.5) is the updated position for the velocity-Verlet method. Substituting

$$\dot{F}(t) = \frac{[F(t + h) - F(t)]}{h} + O(h)$$

into equation (2.6) yields

$$v(t + h) = v(t) + \frac{h}{2}\left[\frac{F(t)}{m} + \frac{F(t + h)}{m}\right] + O(h^3),$$
(2.7)

which is the updated velocity. These equations show that the order of error for both position and velocity after one step is $O(h^3)$. In the velocity-Verlet method, the atomic position $r(t + h)$ at time $t + h$ is updated using the initial position $r(t)$ and velocity $v(t)$. Unlike with the Verlet method, it is easy to evaluate the total energy using the velocity-Verlet method because the position and velocity can be developed at the same time. The velocity-Verlet method can be derived not only from the Taylor expansion of the Verlet method but also by using the Liouville operator, which is a time evolution operator. This derivation is described in the next section.

2.1.2 Derivation of velocity-Verlet method using the Liouville operator

The velocity-Verlet method can be derived using the Liouville time evolution operator. If Newton's equations of motion are integrated, the formulation of the time evolution equation via Taylor expansion is sufficient. In MD simulation, a system with a large number of atoms is difficult to simulate, even using today's high-performance computers, and in a system with few atoms, it is difficult to control temperature and pressure. For the latter case, we define a new Hamiltonian with temperature controls, pressure controls, and constraint conditions between atoms and perform the simulation. In formulating the velocity-Verlet method using the Liouville time evolution operator, the order of error for the position and velocity of the atom is due to the error in the Trotter symmetrical decomposition of the time evolution operator. Time symmetry is evident from the symmetrical decomposition of the time evolution operator.

Below we derive the atomic position of the velocity-Verlet method using the Liouville time evolution operator. The time evolution of an arbitrary physical variable

$A(t) \equiv A(\{\vec{q}_1, \sim, \vec{q}_N, \vec{p}_1, \sim, \vec{p}_N\})$ is

$$\frac{\mathrm{d}A}{\mathrm{d}t} = \sum_j \left(\frac{\partial H}{\partial \vec{p}_j} \cdot \frac{\partial}{\partial \vec{q}_j} - \frac{\partial H}{\partial \vec{q}_j} \cdot \frac{\partial}{\partial \vec{p}_j} \right) A, \tag{2.8}$$

$$\dot{\vec{q}}_j = \frac{\partial H}{\partial \vec{p}_j}, \tag{2.9}$$

$$\dot{\vec{p}}_j = -\frac{\partial H}{\partial \vec{q}_j}, \tag{2.10}$$

where H is the Hamiltonian of the system and $\vec{q}_j$ and $\vec{p}_j$ represent generalized coordinates and momenta, respectively. The Liouville operator is defined as

$$iL \equiv \sum_j \left(\frac{\partial H}{\partial \vec{p}_j} \cdot \frac{\partial}{\partial \vec{q}_j} - \frac{\partial H}{\partial \vec{q}_j} \cdot \frac{\partial}{\partial \vec{p}_j} \right), \tag{2.11}$$

so equation (2.8) becomes

$$\frac{\mathrm{d}A}{\mathrm{d}t} = iLA. \tag{2.12}$$

The formal solution of equation (2.12) is

$$A(t) = \exp(iLt) \, A(0). \tag{2.13}$$

Applying the Taylor expansion to $\exp(iLt)$ in equation (2.13) yields

$$\exp(iLt) = 1 + iLt + \frac{t^2}{2!}(iL)^2 + \frac{t^3}{3!}(iL)^3 + \cdots. \tag{2.14}$$

If the Hamiltonian H is defined as

$$H(\{\vec{r}_1, \dots, \vec{r}_N\}, \{\vec{p}_1, \dots, \vec{p}_N\}) = \sum_{j=1}^{N} \frac{|\vec{p}_j|^2}{2m_i} + U(\{\vec{r}_1, \dots, \vec{r}_N\}), \tag{2.15}$$

the Liouville operator [equation (2.11)] can be decomposed as follows:

$$iL = \sum_j \left(\frac{\partial H}{\partial \vec{p}_j} \cdot \frac{\partial}{\partial \vec{r}_j} - \frac{\partial H}{\partial \vec{r}_j} \cdot \frac{\partial}{\partial \vec{p}_j} \right)$$

$$= iL_\mathrm{A} + iL_\mathrm{B}, \tag{2.16}$$

where

$$iL_A \equiv -\sum_j \frac{\partial H}{\partial \vec{r}_j} \cdot \frac{\partial}{\partial \vec{p}_j}, \tag{2.17}$$

$$iL_B \equiv \sum_j \frac{\partial H}{\partial \vec{p}_j} \cdot \frac{\partial}{\partial \vec{r}_j}. \tag{2.18}$$

If this decomposition holds true, the time reversal operator can be transformed by the Trotter formula as follows:

$$\exp(iLh) = \exp\left(i\frac{h}{2}L_A\right)\exp(ihL_B)\exp\left(i\frac{h}{2}L_A\right) + O(h^3). \tag{2.19}$$

The Trotter product formula is

$$\exp[t(A+B)] = \lim_{n\to\infty}\left[\exp\left(\frac{t}{n}A\right)\exp\left(\frac{t}{n}B\right)\right]^n \tag{2.20}$$

and contains the order of error $O(t^2/n)$ for a finite n. The Trotter product formula by symmetrical decomposition is

$$\exp[t(A+B)] = \lim_{n\to\infty}\left[\exp\left(\frac{t}{2n}A\right)\exp\left(\frac{t}{n}B\right)\exp\left(\frac{t}{2n}A\right)\right]^n, \tag{2.21}$$

where the order of error is $O(t^3/n^2)$ for a finite n. The time evolution for position and velocity is defined as

$$
\begin{aligned}
\begin{pmatrix} r(h) \\ p(h) \end{pmatrix} &= \exp\left(-\frac{h}{2}\frac{\partial U}{\partial r}\frac{\partial}{\partial p}\right)\exp\left(\frac{hp}{m}\frac{\partial}{\partial r}\right)\exp\left(-\frac{h}{2}\frac{\partial U}{\partial r}\frac{\partial}{\partial p}\right)\begin{pmatrix} r(0) \\ p(0) \end{pmatrix} \\
&= \exp\left(-\frac{h}{2}\frac{\partial U}{\partial r}\frac{\partial}{\partial p}\right)\exp\left(\frac{hp}{m}\frac{\partial}{\partial r}\right)\begin{pmatrix} r(0) \\ p(0) - \frac{h}{2}\frac{\partial U}{r(0)} \end{pmatrix} \\
&= \exp\left(-\frac{h}{2}\frac{\partial U}{\partial r}\frac{\partial}{\partial p}\right)\begin{pmatrix} r(0) + \frac{h}{m}p_1 \\ p_1 \end{pmatrix} \\
&= \begin{pmatrix} r_1 \\ p_1 - \frac{h}{2}\frac{\partial U}{r_1} \end{pmatrix},
\end{aligned}
\tag{2.22}
$$

where

$$r_1 = r(0) + \frac{h}{m}p_1$$

and

$$p_1 = p(0) - \frac{h}{2} \frac{\partial U}{r(0)}.$$

In summary, the position and momentum are defined as

$$r(h) = r(0) + \frac{h}{m} \left[p(0) - \frac{t}{2} \frac{\partial U}{\partial r(0)} \right]$$

$$p(h) = p(0) - \frac{h}{2} \frac{\partial U}{\partial r(0)} - \frac{h}{2} \frac{\partial U}{\partial r(h)}.$$

(2.23)

These equations define the velocity-Verlet method and are the same as those obtained using a Taylor expansion.

Because the velocity-Verlet method provides time reversibility and symplecticness, there is no error divergence, even in time evolution for an extended time. Time reversibility can also be confirmed using the Liouville time evolution operator. When time reversibility is confirmed, the position is defined by

$$\exp iL(-h)q(h)$$

$$= \exp iL_A \left(-\frac{h}{2} \right) \exp iL_B(-h) \exp iL_A \left(-\frac{h}{2} \right) q(h)$$

$$= \exp iL_A \left(-\frac{h}{2} \right) \exp iL_B(-h) \exp iL_A \left(-\frac{h}{2} \right) \times$$

$$\exp iL_A \left(\frac{h}{2} \right) \exp iL_B(h) \exp iL_A \left(\frac{h}{2} \right) q(0)$$

(2.26)

$$= \exp iL_A \left(-\frac{h}{2} \right) \exp iL_B(-h) \exp iL_B(h) \exp iL_A \left(\frac{h}{2} \right) q(0)$$

$$= \exp iL_A \left(-\frac{h}{2} \right) \exp iL_A \left(\frac{h}{2} \right) q(0)$$

$$= q(0),$$

and returns to the original position.

The symplecticness of the velocity-Verlet method is confirmed by the existence of the integral invariant Jacobian matrix of the Poincaré map of the phase space for the time transformation by canonical transformation. The existence is confirmed when the determinant of the Jacobian matrix is 1. The Jacobian matrix must exist for symplecticness to exist. For the determinant of the Jacobian matrix in the velocity-Verlet method, we have

$$
\begin{vmatrix} \dfrac{\partial x(h)}{\partial x(0)} & \dfrac{\partial x(h)}{\partial p(0)} \\[2ex] \dfrac{\partial p(h)}{\partial x(0)} & \dfrac{\partial p(h)}{\partial p(0)} \end{vmatrix} = \begin{vmatrix} \dfrac{\partial x(h)}{\partial x_2} & \dfrac{\partial x(h)}{\partial p_2} \\[2ex] \dfrac{\partial p(h)}{\partial x_2} & \dfrac{\partial p(h)}{\partial p_2} \end{vmatrix} \cdot \begin{vmatrix} \dfrac{\partial x_2}{\partial x_1} & \dfrac{\partial x_2}{\partial p_1} \\[2ex] \dfrac{\partial p_2}{\partial x_1} & \dfrac{\partial p_2}{\partial p_1} \end{vmatrix} \cdot \begin{vmatrix} \dfrac{\partial x_1}{\partial x(0)} & \dfrac{\partial x_1}{\partial p(0)} \\[2ex] \dfrac{\partial p_1}{\partial x(0)} & \dfrac{\partial p_1}{\partial p(0)} \end{vmatrix}
$$

$$(2.27)$$

$$
= \begin{vmatrix} 1 & 0 \\[2ex] \dfrac{h}{2}\dfrac{\mathrm{d}F(x)}{\mathrm{d}x_2} & 1 \end{vmatrix} \cdot \begin{vmatrix} 1 & \dfrac{h}{m} \\[1ex] 0 & 1 \end{vmatrix} \cdot \begin{vmatrix} 1 & 0 \\[2ex] \dfrac{h}{2}\dfrac{\mathrm{d}F\big(x(0)\big)}{\mathrm{d}x(0)} & 1 \end{vmatrix}
$$

$$
= 1.
$$

The symplecticness of the velocity-Verlet method does not preserve the true energy H. For example, in the case of a harmonic oscillator,

$$
H = \frac{(x^2 + v^2)}{2} \tag{2.28}
$$

is not preserved, but

$$
H' = \frac{(x^2 + v^2)}{2} - \frac{h^2}{4}x^2 \tag{2.29}
$$

is preserved. The amount of preservation depends on the time step. Therefore, when h is less than a certain value, there is no divergence of energy, even in a long-time simulation, and there is good preservation. However, as h increases, energy conservation will break.

2.1.3 Accuracies of Verlet and velocity-Verlet methods

There is an interesting relationship between the Verlet method and the velocity-Verlet method. In this section, we have presented the derivation of the Verlet method and the velocity-Verlet method. The updated position of the Verlet method includes the order of error $O(h^4)$ and that of the velocity-Verlet method includes the order of error $O(h^3)$. However, the position $r(t + h)$ of the next step in both methods matches the numerical calculation. Consider the following contradiction. First, we show that $r(t + h)$ in the Verlet method is the same as that in the velocity-Verlet method.

Using equation (2.5), $r(t - h)$ in the velocity-Verlet method is

$$
r(t - h) = r(t) - hv(t) + \frac{h^2}{2}\frac{F(t)}{m}. \tag{2.30}
$$

Substituting equation (2.30) into the right side of equation (2.3) yields

$$r(t + h) = 2r(t) - r(t - h) + h^2 \frac{F(t)}{m}$$

$$= 2r(t) - r(t) + hv(t) - \frac{h^2}{2}\frac{F(t)}{m} + h^2\frac{F(t)}{m} \qquad (2.31)$$

$$= r(t) + hv(t) + \frac{h^2}{2}\frac{F(t)}{m},$$

which is the equivalent of equation (2.5) for the updated position of the velocity-Verlet method. Deformation causes $r(t + h)$ of both methods to be in agreement because $r(t + h)$ of the Verlet method has the same value as that of the velocity-Verlet method by appropriately choosing $r(t)$ and $r(t - h)$. In addition, it can have the same trajectory. Here, $r(t - h)$ is that of the velocity-Verlet method.

Although the position of the Verlet method and the position of the velocity-Verlet method are defined to coincide, the former has an order of error of $O(h^4)$, as shown by the equation (2.1), and the latter has an order of error of $O(h^3)$. Thus, the accuracy of the numerically calculated position minus the error of the true solution of $r(t + h)$ for the Verlet method and the velocity-Verlet method should not be the same, which leads to an apparent contradiction because the value of $r(t - h)$ in equation (2.30) includes the error $O(h^3)$ that is in the Verlet method calculation of $r(t + h)$. $r(t - h)$ in equation (2.31) was calculated using the velocity-Verlet method. If atomic position $r(t)$ and velocity $v(t)$ are true solutions, then $r(t - h)$ includes the error $O(h^3)$ of velocity-Verlet method. Therefore, although the error of the Verlet method position is $O(h^4)$, as seen in equation (2.3), which is the first line of equation (2.31), the position $r(t + h)$ includes the error $O(h^4)$ of the position $r(t - h)$ derived by the Verlet method and the error $O(h^3)$ from the velocity-Verlet method. As a result, the error of $r(t + h)$ of the Verlet method and the velocity-Verlet method is $O(h^3)$, which is the result of matching. In other words, if the initial values of $r(t - h)$ and $v(t)$ are chosen properly, then $r(t + h)$ of the Verlet method and the velocity-Verlet method are identical. Up to now, the error of only one step of the Verlet method and the velocity-Verlet method has been described. In an actual simulation, the trajectory of the atoms over a long time is investigated using iterative calculations of several steps, causing the accumulation of error. The cumulative error of both methods is $O(h^2)$.

Computer simulation includes two kinds of error: a truncation error derived from the numerical integration algorithm and a round-off error generated by the computer

calculations. The round-off error accumulates with each iteration but the computer can handle only finite numbers. As the time-step size of the simulation decreases, the abort error of the numerical calculation decreases, but the number of steps needed to reach the target time of the simulation increases, as does the round-off error.

The MD simulation requires a long time evolution. In the numerical integration of the equation of motion, it is desirable to make the time step as wide as possible from the viewpoint of the round-off error and the expense of the computer calculation. Both the Verlet method and the velocity-Verlet method have little error divergence, even in a long time evolution.

2.2 Classical Interatomic Interaction

In MD simulation, interatomic interactions play an important role in determining the characteristics of materials. Computer calculations of interatomic interactions are the most expensive. Interatomic interactions are determined from experiments and theoretical models and chosen to suit specific properties. To reproduce the characteristics of atomic bonds, e.g., rigid body models such as gases and covalent bonds, ionic bonds, metallic bonds, and van der Waals bonds, interatomic interactions are classified into two-body interaction, three-body interaction, multiple-body interaction, and Coulomb interaction in combination. Some representative potentials are discussed below.

The Lennard-Jones (LJ) potential describes the potential energy of the interaction between two atoms such as noble gas atoms and van der Waals molecules. Because a noble gas is an element with a closed outer shell structure, there is no electron transfer between atoms. Thus, interatomic interaction can be represented by a two-body interaction. The LJ potential comprises a repulsive force term and an attractive force term, depending on the interatomic distance. The attractive force term represents repulsion due to the overlap of electron orbitals and the repulsive force term represents dipole-dipole interaction. The LJ potential is represented by

$$v(r) = 4\epsilon \left[\left(\frac{\sigma}{r} \right)^{12} - \left(\frac{\sigma}{r} \right)^{6} \right], \tag{2.32}$$

where r is the interatomic distance, σ is a parameter with the dimension of distance, and ϵ is a parameter with the dimension of energy. For example, $\sigma = 3.40$ [Å] and $\epsilon = 1.67e^{-21}$ [J] for Ar.

The Stillinger-Weber (SW) potential models the potential of three-body

interaction, in particular, the interaction potential of Si crystal. Si crystals have a diamond cubic crystal structure. Si belongs to Group 14 and has four electrons in the outer orbital to form an sp^3 hybrid orbital. A Si atom forms a covalent bond with four other Si atoms to form a regular tetrahedron. The SW potential, designed to reproduce the structure of a Si crystal, comprises the sum of the potential between two atoms and the potential dependent on the angle between three atoms that reproduces the covalent bond angle.

The total potential energy of the SW potential is

$$\Psi(r_1, \cdots, r_N) = \sum_{\substack{i,j \\ i<j}} \tilde{v}_2(r_i, r_j) + \sum_{\substack{i,j,k \\ i<j<k}} \tilde{v}_3(r_i, r_j, r_k), \tag{2.33}$$

where $\tilde{v}_2$ and $\tilde{v}_3$ are two-body and three-body potential functions, respectively. The two-body potential term is a function of the distance between two atoms and is defined as

$$\tilde{v}_2(r_i, r_j) = v_2(r_{ij}), \tag{2.34}$$

$$v_2(r_{ij}) = \epsilon f_2\left(\frac{r_{ij}}{\sigma}\right), \tag{2.35}$$

where

$$f_2(r) = \begin{cases} A(Br^{-p} - r^{-q})\exp[(r-a)^{-1}], & r < a \\ 0, & r > a \end{cases}. \tag{2.36}$$

The parameters $\{A, B, p, q, a, \sigma, \epsilon\}$ that satisfy the experimental result are $A = 7.049556277$, $B = 0.6022245584$, $p = 4$, $q = 0$, $q = 0$, $a = 1.80$, $\sigma = 0.20951$ [nm], $\epsilon = 50$ [kcal/mol]. The three-body potential term is a function of the distance between the atom of interest and the other two atoms and the angle formed by them. It is expressed as

$$\tilde{v}_3(r_i, r_j, r_k) = v_3(r_{ij}, r_{ik}, \theta_{jik}) + v_3(r_{jk}, r_{ji}, \theta_{kji}) + v_3(r_{ki}, r_{kj}, \theta_{ikj}), \tag{2.37}$$

$$v_3(r_{ij}, r_{ik}, r_{jik}) = \epsilon f_3(r_{ij}/\sigma, r_{ik}/\sigma, \theta_{jik}), \tag{2.38}$$

where

$$f_3(r_{ij}, r_{jk}, \theta_{jik})$$
$$= \lambda \exp\left[\gamma(r_{ij} - a)^{-1} + \gamma(r_{ik} - a)^{-1}\right] \cdot \left(\cos\theta_{jik} + \frac{1}{3}\right)^2 \tag{2.39}$$

and $\lambda = 21.0$ and $\gamma = 1.20$. For a tetrahedron, the angle $\theta = 120.0$ and the energy $f_3 = 0$.

The SW potential is in good agreement with experimental data for Si in the crystalline state. However, noncrystalline state conditions and reaction phenomena cannot be reproduced. For example, the reaction that occurred in the experiment from which the data were obtained was the progression of a crack fracture in a Si crystal. The potential for a crystalline state, such as the SW potential, cannot reproduce the experimental state in which the bond between the Si atoms at the crack tip of the breakdown phenomenon is changing. In such a situation, the potential that includes the breakdown of the bond rather than the potential that reproduces only a crystal structure must be considered. However, it is difficult to have the potential incorporate the experimental data that correspond to such varying conditions. Therefore, it is necessary to use the interatomic potential obtained from quantum mechanics with respect to the electronic state.

The Coulomb force between ions is a function of r^{-1} and long-range force. The number of interactions in a bulk system is quite large so special computational methods are necessary for high-precision calculations. Various methods have been devised to increase the speed of calculating the Coulomb force, one of which is the Ewald method that is described later.

Metallic bonds must reflect the effect of the Coulomb force between the cations of metallic crystals and the free electrons that move freely around them. Elements that have conduction electrons distributed over a relatively long distance must be in a large volume. For metallic bonding, a multibody action potential, such as the embedded-atom method (EAM) potential, has been proposed. In addition to the usual two-body potential (attraction and repulsion), EAM includes a multibody term, which is the energy that results from atoms with an electronic density ρ_i, which is created by superimposing conduction electrons around the atoms:

$$V = \sum_{i,j}^{i<j} \Phi(r_{ij}) + \sum_i F(\rho_i). \tag{2.40}$$

The potential of a molecular model such as an organic molecule is thought to include two-, three-, or four-body interaction and the Coulomb force by combining the covalent bonds between atoms. This potential requires many parameters depending on the molecular system.

2.3 Calculation Method for MD Simulation

MD simulation of a large-scale system takes a long time. The most time-consuming part of the simulation is the calculation of the force on atoms. The direct calculation of force becomes the calculation of $O(N^2)$, where N is the number of the atoms. As N increases, it becomes impossible to calculate the force in a realistic time frame. To accelerate the calculation of the force, and thus the MD simulation, parallelization using a parallel computer has been employed.

Here we discuss methods to accelerate MD simulation that correspond to the interaction distance between atoms. For short-range interactions, the calculation amount can be set to $O(N)$ by introducing a cutoff interaction distance. For long-range interactions, a cutoff distance is not possible. However, it is possible to reduce the computational complexity of long-range interactions and maintain certain computational precision via the Ewald method.

2.3.1 Calculation method of short-range interaction

In MD simulation, the calculation of the force acting on a particle accounts for more than 90% of the simulation iteration loop time. Therefore, accelerating the calculation of this force is the most efficient way to shorten the execution time of the MD simulation. The force calculation reduces the number of pairs of interacting atoms since it is the sum of the interactions of the atom of interest and other atoms. For short-range interactions, the number of pairs of atoms can be reduced by setting a cutoff interatomic interaction distance. However, despite the use of a cutoff interaction distance, calculation of the distance for all pairs of atoms is still required, so the calculation of $O(N^2)$ is necessary. Therefore, use of a cutoff distance does not significantly reduce the amount of calculation. Therefore, the next step is to accelerate the pair interaction calculation. The system is divided into square cells, with the length of each side the cutoff distance r_{cut}, and the atoms in each cell are registered (see Fig. 2.1). The amount of calculation obtained by this cell division method is $O(N)$. In the three-dimensional system, the pair calculation searches for only the cell in which the atom of interest is registered and the atoms registered in the 26 cells surrounding that cell. Therefore, because the number of atoms to be searched per atom of interest is almost constant, the amount of calculation is proportional to N. Therefore, the amount of calculation is $O(N)$.
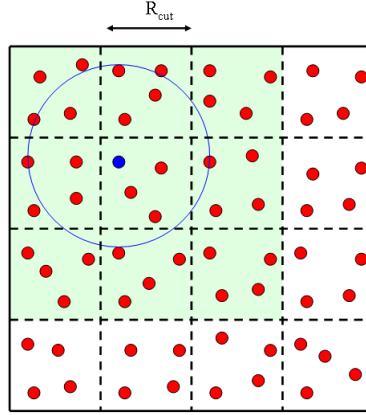
Figure 2.1. System divided into square cells of r_{cut} size. To compute the forces on an atom, the calculation searches for atoms in the green area.

There is another way to reduce the amount of calculation. Although the amount of calculation of the cell division method (Fig. 2.1) is $O(N)$, the cell division performed in every step requires time. In addition, the pairing of each atom with atoms in neighboring cells must be calculated. To further reduce the amount of calculation, atoms registered around each atom via the neighborhood atom registration method are used. The atoms in solids such as crystals hardly move, with vibration the main cause of movement. Therefore, since the targets of pair computation hardly change, it is possible to eliminate the computational complexity of cell division by registering in advance the neighboring atoms of a particular atom to undergo pair calculation. In addition, instead of pairing an atom with the other atoms in its cell, it is sufficient to pair the atom with atoms near it, thus reducing the amount of calculation.

The calculation of short-range interaction is suitable for the distributed-memory-type parallel computer. In parallel computing, memory data are shared via internode communication, which causes a large bottleneck in parallel computation. In parallelization by real-space division, short-range interaction calculations can reduce the amount of communication data since the interacting atoms are those only in the neighboring region. Thus, excellent parallelization can be obtained.

2.3.2 Calculation method for long-range interaction

Coulomb force is repulsive between particles with different charges like ionic crystals and molecules and is proportional to $1/r$. Coulomb force is a long-range

interaction, so a cutoff distance cannot be applied to it. Therefore, the amount of calculation is $O(N^2)$. When there are a number of particles, direct calculation of the interactions is not realistic. The Ewald method accelerates the calculation of the Coulomb force by dividing the Coulomb interaction into a short-range component and a long-range component and calculating the long-range interaction in inverse space. The Ewald method used in this study is discussed below.

Coulomb interaction is a problem of condition convergence, and charge bias occurs because of how the periodic boundary system is defined. This charge bias appears as a macroscopic dipole. Considering the effect of the macroscopic dipole, the energy varies depending on how the periodic system is defined; therefore, the energy cannot be evaluated accurately. The Ewald method can evaluate energy while ignoring the macroscopic dipole term, so the effect of charge bias is excluded. The Ewald method divides the Coulomb interaction into a short-range component and a long-range component, calculates the short-range component directly, and calculates the long-range component in wavenumber space. Therefore, the amount of calculation of the Ewald method is $O(N^{3/2})$, so high-speed computation is possible.

Because calculations for Coulomb interaction involve condition convergence, we introduce a convergence factor s. In the Coulomb interaction equation, Coulomb interaction is denoted as

$$\frac{1}{r_{ij}} \to \frac{1}{r_{ij}} e^{-sr_{ij}^2}. \tag{2.41}$$

The convergence condition is when $s \to 0$ in this equation. The Ewald method is the summation of the real-space sum and the wavenumber-space sum in consideration of periodic boundary conditions (PBCs).

First, for an infinite sum in real space at PBCs,

$$v(\vec{x}, s) = \sum_{\vec{R}_c} e^{-s R_c^2} \frac{1}{|\vec{x} + \vec{R}_c|} \tag{2.42}$$

where $\vec{x}$ is the position of the period box and $\vec{R}_C$ is the position vector of the period box. Transformation of equation (2.42) using the Γ function yields

$$v(\vec{x}.s) = \frac{1}{\sqrt{\pi}} \sum_{\vec{R}_c} \int_0^\infty t^{-1/2} e^{-t|\vec{x}+\vec{R}_c|^2} e^{-s\vec{R}_c} dt \tag{2.43}$$

$$= \frac{1}{\sqrt{\pi}} \sum_{\vec{R}_c} \int_0^{\eta^2} t^{-1/2} \, e^{-t|\vec{x}+\vec{R}_c|^2} \, e^{-sR_c^2} dt$$

$$+ \sum_{\vec{R}_c} \frac{\text{erfc}(\eta|\vec{x} - \vec{R}_c|)}{|\vec{x} + \vec{R}_c|} e^{-sR_c^2}.$$

The complementary error function is defined as

$$\text{erfc}(x) = \frac{2}{\sqrt{\pi}} \int_x^\infty e^{-t^2} dt = \frac{1}{\sqrt{\pi}} \int_{x^2}^\infty e^{-y} \frac{1}{\sqrt{y}} dy. \tag{2.44}$$

Now, the Fourier component of wavenumber $\vec{k}$ of $\sum_{\vec{R}_c} e^{-t|\vec{x}+\vec{R}_c|^2}$ is given as

$$\int \sum_{\vec{R}_c} e^{-t|\vec{x}+\vec{R}_c|^2} e^{-i\vec{k}\cdot\vec{R}} d\vec{x} = \sum_{\vec{R}_c} \left(\frac{\pi}{t}\right)^{3/2} e^{+i\vec{k}\cdot\vec{R}_c} e^{-k^2/4t}. \tag{2.45}$$

Therefore, equation (2.45) can be written as

$$\sum_{\vec{R}_c} e^{-t|\vec{x}+\vec{R}_c|^2} = \int \frac{d\vec{k}'}{2\pi} \sum_{\vec{R}_c} \left(\frac{\pi}{2}\right)^{3/2} e^{+i\vec{k}\cdot\vec{R}_c} e^{-k'^2/4t} e^{i\vec{k}\cdot\vec{x}}$$

$$= \frac{1}{\Omega} \sum_{\vec{n}} \left(\frac{\pi}{t}\right)^{3/2} e^{-|\vec{k}_{\vec{n}}|^2/4t} e^{i\vec{k}\cdot\vec{x}} \tag{2.46}$$

$$= \frac{1}{\Omega} \sum_{\vec{k}} \left(\frac{\pi}{t}\right)^{3/2} e^{-\vec{k}/4t} e^{i\vec{k}\cdot\vec{x}},$$

which becomes

$$\sum_{\vec{R}_c} e^{-t|\vec{x}+\vec{R}_c|} = \frac{1}{\Omega} \left(\frac{\pi}{t}\right)^{3/2} \sum_{\vec{k}} e^{-k^2/4t} \, e^{i\vec{k}\cdot\vec{x}}. \tag{2.47}$$

Equation (2.47) is used as follows. Assume the convergence factor $s \to 0$. From equation (2.43), the first term of $v(\vec{x}, s)$ is

$$\frac{1}{\sqrt{\pi}} \sum_{\vec{R}_c} \int_0^{\eta^2} t^{-1/2} \, \exp\left(-t|\vec{x} + \vec{R}_c|^2\right) \, \exp(-sR_c^2) \quad dt$$

$$= \frac{1}{\sqrt{\pi}} \int_0^{\eta^2} t^{-1/2} dt \sum_{\vec{R}_c} \exp\left[-(s+t)\left|\vec{R}_c + \frac{t}{s+t}\vec{x}\right|^2\right] \, \exp\left(-\frac{st}{s+t}x^2\right)$$

$$= \frac{1}{\sqrt{\pi}} \int_0^{\eta^2} t^{-1/2} \, dt \, \frac{1}{\Omega} \left(\frac{\pi}{s+t}\right)^{3/2} \sum_{\vec{R}_c} \exp\left[-\frac{k^2}{4(s+t)}\right] \exp\left[i\vec{k}\left(\frac{t}{s+t}\vec{x}\right)\right] \exp\left(-\frac{st}{s+t}x^2\right)$$

$$= \frac{\pi}{\Omega} \sum_{\vec{R}} \int_0^{\eta^2} dt(s+t)^{-3/2} \, t^{-1/2} \exp\left[-\frac{k^2}{4(s+t)}\right] \exp\left(i\vec{k}\cdot\vec{x}\,\frac{t}{s+t}\right) \exp\left(-\frac{st}{s+t}x^2\right) \ .$$

(2.48)

When $\vec{k} \neq 0$, the first term of $v(\vec{x}, s)$ converges when $s = 0$. On the other hand, it is necessary that $\vec{k} = 0$ for $s > 0$,

$$= \frac{\pi}{\Omega} {\sum_{\vec{k}}}' \int_0^{\eta^2} dt \, t^{-2} e^{-k^2/4t} e^{i\vec{k}\cdot\vec{x}} + (\vec{k} = 0 \text{ term})$$

$$= \frac{\pi}{\Omega} {\sum_{\vec{k}}}' \int_{\frac{1}{\eta^2}}^{\infty} d\left(\frac{1}{t}\right) e^{-k^2/4t} e^{i\vec{k}\cdot\vec{x}} + (\vec{k} = 0 \text{ term})$$

(2.49)

$$= \frac{4\pi}{\Omega} {\sum_{\vec{k}}}' e^{i\vec{k}\cdot\vec{x}} e^{-k^2/4\eta^2} \frac{1}{k^2} + (\vec{k} = 0 \text{ term}) \ .$$

where the $\vec{k} = 0$ term is

$$\frac{\pi}{\Omega} \int_0^{\eta^2} dt(s+t)^{-3/2} t^{-1/2} \exp\left(-\frac{st}{s+t}x^2\right) \ .$$

(2.50)

If $u = t/(s+t)$, equation (2.50) becomes

$$= \frac{\pi}{\Omega} \int_0^{\frac{\eta^2}{s+\eta^2}} \frac{du}{su^{1/2}} e^{-sux^2}$$

$$= \frac{\pi}{s\Omega} \int_0^{\frac{\eta^2}{s+\eta^2}} \frac{e^{-sux^2}}{u^{1/2}} \, du.$$

(2.51)

With respect to s, equation (2.51) now becomes

$$= \frac{\pi}{s\Omega} \int_0^1 du \, \frac{1}{u^{1/2}} (1 - sux^2 + \cdots) + \frac{\pi}{s\Omega} e^0 \left[-\frac{\eta}{(s+\eta^2)^2}\right]_{s=0} s + O(s)$$

$$= \frac{\pi}{s\Omega} \left(2 - sx^2 \frac{2}{3} + \cdots\right) - \frac{\pi}{\Omega\eta^2} + O(s)$$

(2.52)

$$= \frac{2\pi}{s\Omega} - \frac{\pi}{\Omega\eta^2} - \frac{2\pi}{3\Omega} x^2 + O(s).$$

When $s \approx 0$, as above,

$$\sum_{\vec{R}_c} e^{-sR_c^2} \frac{1}{|\vec{x} + \vec{R}_c|} = \sum_{\vec{R}_c} \frac{\mathrm{erfc}(\eta|\vec{x} + \vec{R}_c|)}{|\vec{x} + \vec{R}_c|} + \frac{4\pi}{\Omega} {\sum_{\vec{R}}}' \frac{1}{K^2} e^{-k^2/4\eta} \; e^{i\vec{k}\cdot\vec{x}}$$

$$- \frac{2\pi}{3\Omega}|\vec{x}|^2 + \frac{2\pi}{\Omega s} - \frac{\pi}{\Omega\eta^2} + O(s).$$ (2.53)

For a charge-neutral system,

$$\frac{2\pi}{\Omega s} - \frac{\pi}{\Omega\eta^2} = 0$$

in total.

Consider the application to a charge-neutral system. For a charge-neutral system, $\sum_{i=1}^{N} z_i = 0$. The Coulomb potential $\phi(\vec{r})$ at position $\vec{r}$ is

$$\phi(\vec{r}) = \sum_{\vec{R}_c} \sum_{j=1}^{N} \frac{Z_j}{|\vec{r} - \vec{r}_j - \vec{R}_c|}$$

$$= \frac{1}{\Omega} {\sum_{\vec{R}}}' \frac{4\pi}{k^2} e^{-\gamma^2 k^2} \sum_{j=0}^{N} Z_j e^{i\vec{k}\cdot(\vec{r}_j - \vec{r})}$$

$$+ \sum_{\vec{R}_c} \sum_{j=1}^{N} \frac{Z_j}{|\vec{r} - \vec{r}_j - \vec{R}_c|} \mathrm{erfc}\left(\frac{|\vec{r} - \vec{r}_j - \vec{R}_c|}{2\gamma} \right)$$

$$- \frac{2\pi}{3\Omega} \sum_{j=1}^{N} Z_j |\vec{r} - \vec{r}_j|^2,$$ (2.54)

where

$$\vec{k} = \frac{2\pi}{\Omega}\left(l\,\vec{b}\times\vec{c} + m\vec{c}\times\vec{a} + n\vec{a}\times\vec{b} \right),$$

$$\Omega = \vec{a} \cdot \left(\vec{b}\times\vec{c} \right).$$ (2.55)

Since $\vec{r} = \vec{r}_l$ ($l = \{1, 2, \cdots, N\}$) diverges when ϕ, let $\phi(\vec{r} = \vec{r}_l)$ be calculated by eliminating its divergence term, i.e., removing the self-term. In other words, $\phi'(\vec{r} = \vec{r}_l)$ $= \phi(\vec{r}_l + \vec{\delta}) = \phi(\vec{r}_l + \vec{\delta}) - Z_l/|\vec{\delta}|$ at $|\vec{\delta}| \approx 0$,

$$\phi'(\vec{r}_l) = \frac{1}{\Omega}\sum_{\vec{R}_c}' \frac{4\pi}{k^2} e^{-\gamma^2 k^2} \sum_{j=1}^{N} Z_j e^{i\vec{k}\cdot(\vec{r}_j - \vec{r}_l)}$$

$$+ \sum_{\vec{R}_c}\sum_{j}^{+l} \frac{Z_j}{|\vec{r}_i - \vec{r}_j - \vec{R}_c|}\,\mathrm{erfc}\left(\frac{|\vec{r}_l - \vec{r}_j - \vec{R}_c|}{2\gamma}\right)$$

$$+ \sum_{\vec{R}_c}\left\{\frac{Z_l}{|\vec{\delta} - \vec{R}_c|}\,\mathrm{erfc}\left(\frac{|\vec{\delta} - \vec{R}_c|}{2\gamma}\right) - \frac{Z_l}{|\vec{\delta}|}\right\}_{|\vec{\delta}|=0}$$

$$- \frac{2\pi}{3\Omega}\sum_{j=1}^{N} Z_j |\vec{r}_l - \vec{r}_j|^2. \qquad (2.56)$$

If $\mathrm{erfc}(x) = 1 - 2/\sqrt{\pi}\int_0^x dt\, e^{-t^2}$, then

$$\left[\frac{\mathrm{erfc}(x)}{x}\right]_{x\approx 0} = \left[\frac{1}{x} - \frac{2}{\sqrt{\pi}x}\int_0^x dt e^{-t^2}\right]_{x\approx 0} \qquad (2.57)$$

$$e^{-t^2} = 1 - t^2 + \frac{t^4}{2} - \cdots.$$

Therefore,

$$\int_0^x e^{-t^2}dt = x - \frac{x^3}{3} + \cdots$$

$$= \left[\frac{1}{x} - \frac{2}{\sqrt{\pi}x}\left(x - \frac{x^3}{3} + \cdots\right)\right]_{x\approx 0} \qquad (2.58)$$

$$= \frac{1}{x} - \frac{2}{\sqrt{\pi}} + O(x^2)$$

and

$$\{\sim\}_{|\vec{\delta}|=0} = \sum_{\vec{R}_c}' \frac{Z_l}{R_c}\,\mathrm{erfc}\left(\frac{R_c}{2\gamma}\right) - \frac{Z_l}{\sqrt{\pi}\gamma}, \qquad (2.59)$$

$$\phi' \; r \; = \; \Omega \; \textrm{Rc. } 4\pi \; e^{-\gamma 2 k2} \; \sum_{j=1}^{N} Z_i e^{ik\cdot ril} \qquad (2.60)$$

$$+ \sum_{\vec{R}_c} \sum_{j}^{\pm l} \frac{Z_j}{|\vec{r}_{lj} - \vec{R}_c|} \operatorname{erfc}\left(\frac{|\vec{r}_{lj} - \vec{R}_c|}{2\gamma}\right)$$

$$+ \sum_{R}' \frac{Z_l}{R_c} \operatorname{erfc}\left(\frac{R_c}{2\gamma}\right) - \frac{Z_l}{\sqrt{\pi}\gamma}$$

$$- \frac{2\pi}{3\Omega} \sum_{j=1}^{N} Z_j |\vec{r}_l - \vec{r}_j|^2 \; .$$

The last term in equation (2.60) is a macroscopic dipole that can be ignored in the Ewald method. The total energy obtained via the Ewald method is

$$V = \frac{1}{2} \sum_{l=1}^{N} Z_l \phi'(\vec{r}_l) \tag{2.61}$$

excluding the macroscopic dipole term. Because the Ewald method eliminates the macroscopic dipole term, the result does not depend on how to determine the MD box. In fact, the last term is

$$\sum_{l}^{N} Z_l \left(\sum_{j}^{N} Z_j |\vec{r}_l - \vec{r}_j|^2\right) = \sum_{l} \sum_{j} \left(Z_l Z_j r_l^2 + Z_l Z_j r_j^2 - 2Z_l Z_j \vec{r}_l \cdot \vec{r}_j\right)$$

$$= -2 \sum_{l} \sum_{j} Z_l Z_j \, \vec{r}_l \cdot \vec{r}_j \tag{2.62}$$

$$= -2 \left(\sum_{l} Z_l \vec{r}_l\right) \cdot \left(\sum_{j} Z_j \vec{r}_j\right)$$

and represents the dipole term.

Now we estimate the computational complexity of the Ewald method, $O(N^{3/2})$. Equation (2.61) is the amount of computation that occurs when the parameter is adjusted so that the sum of the computational amounts of the real-space component and the wavenumber-space component is minimized. First, let L be the size of the PBC system of the simulation, where $L \propto N^{1/3}$ and N is the number of particles. The convergence factor is γ, the maximum wavenumber is $k_{\max}$, and the interaction distance in real space is r_{cut}. $k_{\max}$ is related to the corresponding maximum integer $n_{\max} = LK_n/2\pi$. If γ is large, then r_{cut} increases. The total energy of the Ewald method is

expressed as

$$E = \frac{1}{2\Omega} \sideset{}{'}\sum_{\vec{R}} \frac{4\pi}{K^2} e^{-\gamma^2 K^2} \left(\sum_{j}^{N} Z_j e^{i\vec{K}\cdot\vec{r}_j} \right) \left(\sum_{j}^{N} Z_j e^{i\vec{K}\cdot\vec{r}_j} \right)$$

$$+ \frac{1}{2} \sideset{}{'}\sum_{\vec{R}_c} \sum_{i} \sum_{j}^{i\neq j} \frac{Z_i Z_j}{|\vec{r}_{ij} - \vec{R}_c|} \operatorname{erfc}\left(\frac{|\vec{r}_{ij} - \vec{R}_c|}{2\gamma} \right) \quad (2.63)$$

$$+ \frac{1}{2} \sideset{}{'}\sum_{\vec{R}_c} \sum_{i} \frac{Z_i{}^2}{R_c} \operatorname{erfc}\left(\frac{R_c}{2\gamma} \right) - \sum_{i} \frac{Z_i{}^3}{2\sqrt{\pi}\gamma}.$$

Next, $\gamma \equiv N^{\alpha}$, where α is undetermined, and $r_{\text{cut}} = \gamma = N^{\alpha}$. The amount of calculation for the real-space component is

$$N \times \gamma_{\text{cut}}{}^3 = N^{1+3\alpha} \quad (2.64)$$

from the second and third terms of equation (2.63). The amount of calculation for the wavenumber-space component is

$$N \times n_{\text{max}}{}^3 = N^{2-3\alpha} \quad (2.65)$$

from the first term of equation (2.63). Since $K_{\text{max}} = \gamma^{-1} = N^{-\alpha}$ and $L = N^{1/3}$, then $n_{\text{max}} = N^{(1/3)-\alpha}$. The calculation amounts for the real-space component and the wavenumber-space component are the minimum when $\alpha = 1/6$ in the expression $1 + 3\alpha = 2 - 3\alpha$. The order of error for both the real-space and the wavenumber-space calculations is approximately $O(N^{3/2})$.

3 Electronic State Calculation for MD Simulation

3.1 Density Functional Theory

Empirical interaction potentials are set to match certain properties of materials well. In addition, they have low computational costs and are easy to use, but they are not versatile enough for use in various situations. The potential is difficult to express using only simple parameters when the bonding state changes, such as in a chemical reaction. Originally, chemical reaction simulations had to deal with electrons, which are coupling carriers. Thus, electronic states had to be considered in interatomic interactions. When calculating electronic states using quantum mechanics, a direct method cannot solve the problem of multiple electrons. Methods such as the Hartree-Fock theory and the density

functional theory (DFT) are methods of approximation for solving multiple-electron problems. In this study, we used the DFT method. It has high precision, relatively low computational costs, is suitable for use on a distributed-memory-type parallel computer, and enables large-scale calculations. DFT was devised by Walter Kohn, who won the Nobel Prize in chemistry in 1998 with John Pople.

To calculate the electronic state, the wave function of electrons must be determined using the Schrödinger equation; however, the multiple-body problem for ions and electrons cannot be solved directly. Therefore, by approximating the Hamiltonian or adding restrictions to the wave function, the Schrödinger equation is transformed into a solvable form. In the DFT, the Hamiltonian and the orbital function are based on the electron density instead of the wave function. The DFT equation can be solved using the Kohn-Sham equation, which has been devised to reduce the computational cost.

First, in the DFT, the Hamiltonian must be expressed using the electron density rather than the electronic wave function. Next, the Coulomb potential of the external field caused by atomic nuclei and felt by electrons is defined as

$$V(r) = -\sum_{\alpha} \frac{Z_{\alpha} e^2}{|r - R_{\alpha}|}, \tag{3.1}$$

where α is the number of a particular nucleus. From equation (3.1), the electron density is uniquely determined. Conversely, Hohenberg and Kohn showed that the external field $V(r)$ can be determined using the electron density $n(r)$. According to the Hohenberg-Kohn (HK) theory, the electron density and the external field correspond one to one, so the external potential energy is a functional of the electron density. The HK theory is the foundation of the DFT. The HK theory is proven by a contradiction. First, assume that V and V' produce the same $n(r)$. When the external field is V, the Hamiltonian is H, the wave function of the ground state is Ψ, and the energy of the ground state is E. For the external field V', the Hamiltonian is H', the wave function of the ground state is Ψ', and the energy of ground state is E'. These parameters are related as follows:

$$E = \langle \Psi | H | \Psi \rangle, \tag{3.2}$$

$$E' = \langle \Psi' | H | \Psi' \rangle. \tag{3.3}$$

Use of the variation principle with equations (3.2) and (3.3) results in

$$E < \langle \Psi' | H | \Psi' \rangle = \langle \Psi' | (H + V' - V') | \Psi' \rangle \tag{3.4}$$

$$= \langle \Psi' | (H' + V - V') | \Psi' \rangle$$
$$= \langle \Psi' | H' | \Psi' \rangle + \langle \Psi' | (V - V') | \Psi' \rangle$$
$$= E' + \langle \Psi' | (V - V') | \Psi' \rangle,$$

which results in

$$\therefore E < E' + \langle \Psi' | (V - V') | \Psi' \rangle. \tag{3.5}$$

Similarly,

$$E < \langle \Psi | H | \Psi \rangle = \langle \Psi | (H - V - V') | \Psi \rangle$$
$$= E - \langle \Psi | (V - V') | \Psi \rangle, \tag{3.6}$$

resulting in

$$\therefore E' < E - \langle \Psi | (V - V') | \Psi \rangle. \tag{3.7}$$

Combining equations (3.5) and (3.7), we get

$$E + E' < E + E' + \langle \Psi' | (V - V') | \Psi' \rangle - \langle \Psi | (V - V') | \Psi \rangle. \tag{3.8}$$

However, V and V' are functions of electron position only and Ψ and Ψ' produce the same $n(r)$. Therefore,

$$n(r) = \langle \Psi | \Psi \rangle = \langle \Psi' | \Psi' \rangle,$$
$$\langle \Psi' | V - V' | \Psi \rangle - \langle \Psi | V - V' | \Psi \rangle$$
$$= \int n(r)[V(r) - V'(r)]\mathrm{d}r - \int n(r)[V(r) - V'(r)]\mathrm{d}r \tag{3.9}$$
$$= 0$$

This conflicts with

$$E + E' < E + E'. \tag{3.10}$$

From equation (3.10), we conclude that it is impossible for V and V' to produce the same $n(r)$, i.e., only one external potential energy can produce $n(r)$. The original paper presented the HK theory in which there is a one-to-one relationship between $V(r)$ and $n(r)$. Total energy is determined by $V(r)$ and the total number of electrons. Furthermore, the one-to-one relationship between $V(r)$ and $n(r)$ shows that the total energy is a functional of the spatial integral of $n(r)$ and is expressed as $E[n(r)]$. The portion of the system that excludes $V(r)$ from the Hamiltonian, i.e., the energy value $\langle \Psi | H' | \Psi \rangle$ for

$$H' = H - V$$

$$= \sum_i \frac{p_i^2}{2m} + \sum_{\substack{i,j \\ i<j}} \frac{e^2}{|r_i - r_j|}, \tag{3.11}$$

also depends only on $n(r)$.

$$\therefore F[n(r)] = \langle \Psi | H' | \Psi \rangle. \tag{3.12}$$

Therefore, the total energy can be written as

$$E[n(r)] = F[n(r)] + \int V(r)n(r)\mathrm{d}r. \tag{3.13}$$

The total wave function Ψ has a real part and an imaginary part and is a function of the multiple-electron position set. The total energy can always be expressed as a function of $n(r)$, although the information it contains is much less than that of Ψ. The Kohn-Sham theory seems capable of producing the same electron density as the correct electron density $n(r)$ that corresponds to $V(r)$, with a free-electron (without interaction) system producing an effective external field potential. The wave function of this free-interaction free electron is represented by a single Slater determinant. The kinetic energy E_{kin} of this free-electron system is written as $T_s[n(r)]$. The Hartree term (i.e., the direct term or classical Coulomb term) is a functional of $n(r)$:

$$\frac{e^2}{2} \iint \frac{n(r)n(r')}{|r-r'|} \mathrm{d}r\mathrm{d}r'$$

Thus, the total energy is expressed as

$$\begin{aligned} E[n(r)] = T_s[n(r)] + \frac{e^2}{2} \int \int \frac{n(r,r')}{|r-r'|} \mathrm{d}r\mathrm{d}r' + \int V_{\mathrm{ext}}(r)n(r)\mathrm{d}r \\ + E_{\mathrm{EC}}[n(r)], \end{aligned} \tag{3.14}$$

where E_{XC} is the remainder of $E[n(r)]$ to $T_s[n(r)]$ minus the Hartree term and the external field energy; it is the definition of the exchange-correlation energy of $n(r)$. It is also a functional of the electron density $n(r)$. The Kohn-Sham orbital function is necessary in view of the variation principle by which the variation is zero for $n(\vec{r})$ under the normalization condition $\int \psi_i^*(\vec{r})\psi_i(\vec{r})\mathrm{d}\vec{r} = 1$ for $E[n(\vec{r})]$. If the unknown constant of Lagrange is $\{\epsilon_i\}$ and the normalization condition is the constraint condition, then

$$\left[-\frac{\hbar^2}{2m}\Delta + e^2 \int \frac{n(\vec{r}')}{|\vec{r}-\vec{r}'|}\mathrm{d}\vec{r}' + V_{\mathrm{ext}}(\vec{r}) + \frac{\delta E_{\mathrm{EX}}[n(\vec{r})]}{\delta n(\vec{r})} \right] \psi_i(\vec{r}) = \epsilon_i \psi_i(\vec{r}) \tag{3.15}$$

can be calculated when

$$\frac{\delta\{E[n(\vec{r})] - \sum_{i=1}^{N}\epsilon_i[\int \psi_i^*(\vec{r})\psi_i(\vec{r})\mathrm{d}\vec{r}] - 1]\}}{\delta\psi_i^*(\vec{r})} = 0. \tag{3.16}$$

The eigenvalues $\{\psi_i(\vec{r})\}$ in equation (3.16) can be calculated as the eigenvalues $\{\epsilon_i\}$.

The calculation procedure for the DFT is as follows: For N electron systems (up spin ↑ and down spin ↓ are $N/2$ each),

1. Set the Kohn-Sham orbital function $\{\psi_i(\vec{r})\}$ randomly.

2. Obtain the electron density using $n(r) = 2 \sum_{i=1}^{N/2} |\psi_i(\vec{r})|^2$.

3. Using equation (3.15), solve the eigenvalue function from the minimum fixed value ϵ_1 to the Fermi energy value $\epsilon_{N/2}$ to get $\{\psi_i(\vec{r})\}$.

Repeat steps $1, 2, 3, 2, 3, ...$ until $n(r)$ becomes self-consistent. This eigenvalue problem becomes a large-scale matrix when the number of electrons involved, N, is large, making it difficult to perform the calculation. Therefore, an iterative method such as the conjugate gradient (CG) method is generally used. For exchange-correlation interactions, the local density approximation (LDA), which depends on only electron density, and the generalized gradient approximation (GGA), which corrects the LDA by using the density gradient, have been proposed.

Given the arrangement of nuclei (ions), the wave function of the ground state can be determined via the DFT method. The wave function can then be used to determine the Coulomb force and the force from the electron density that affect the ions. With respect to this force, the MD simulation is performed by moving the position of the ions. The force upon ions can be obtained using the Hellmann-Feynman theorem:

$$H|\Psi\rangle = E(R_\alpha)|\Psi\rangle \text{ with } \langle\Psi|\Psi\rangle = 1, \tag{3.17}$$

where R_α is the position of ion α. The force on ion α is expressed as

$$
\begin{aligned}
F_\alpha &= -\frac{\partial E}{\partial R_\alpha} = -\frac{\partial}{\partial R_\alpha}\langle\Psi|H|\Psi\rangle \\
&= -\left(\frac{\partial}{\partial R_\alpha}\langle\Psi|\right)H|\Psi\rangle - \left\langle\Psi\left|\frac{\partial H}{\partial R_\alpha}\right|\Psi\right\rangle - \left\langle\Psi\left|H\left(\frac{\partial}{\partial R_\alpha}|\Psi\rangle\right)\right.\right. \\
&= -E\frac{\partial}{\partial R_\alpha}\langle\Psi|\Psi\rangle - \left\langle\Psi\left|\frac{\partial H}{\partial R_\alpha}\right|\Psi\right\rangle \\
&= -\left\langle\Psi\left|\frac{\partial H}{\partial R_\alpha}\right|\Psi\right\rangle,
\end{aligned}
\tag{3.18}
$$

with the derivative of energy calculated with respect to the ion position. Here, $\langle\Psi|H = E\langle\Psi|$ is used for formula deformation. Equation (3.18) shows that it is not necessary to calculate the derivative of the wave function, so the force can be determined with little computational cost.

2.2 Technique to accelerate the DFT calculation

Because the DFT calculation involves many electrons, the degree of freedom and the computational cost are large. Therefore, it is common for systems used in the DFT

calculation to contain several hundred atoms depending on the limitations of the computer. In recent years, large-scale parallel computers have performed DFT calculations on systems with thousands of atoms because of improved computer performance and advanced programs. Future DFT calculations must be performed more quickly to handle larger-scale systems.

To calculate equation (3.15), the Kohn-Sham orbital function must undergo normalized orthogonalization. Various normalized orthogonalization methods have been proposed, but the Gram-Schmidt process is used most often. It is a simple and easy-to-understand method for performing normalized orthogonalization of vectors one by one. However, its computational complexity is $O(N^3)$, and for large-scale DFT calculations, it takes up most of the computation time. Therefore, in large-scale computation, it is necessary to speed up the normalized orthogonalization process.

We introduce a matrix-matrix multiplication method that enables the Gram-Schmidt orthogonalization computation to be performed on a high-speed computer. The memory of current computers has a hierarchical structure, with small-capacity cache memory but fast access and large-capacity memory but slow access. High-speed calculations on such a computer require that the cache memory be used effectively.

The Gram-Schmidt orthogonalization process sequentially straightens the vectors one by one. In this process, the vector-vector and matrix-vector multiplications are the main calculations, so the cache memory is not used efficiently and thus many computers do not reach their maximum performance. The computation speed and computer performance can be improved by changing the order of operations and by having the computer efficiently perform many matrix-matrix multiplications. In addition, the performance of matrix-matrix multiplications implies that some computations are performed in parallel, which accelerates the process. This method is used in real-space DFT (RSDFT). It won the Gordon Bell Prize in SC11 in 2011 for execution performance using a supercomputer.

Gram-Schmidt orthogonalization is defined as

$$
\begin{aligned}
\vec{\varphi}_1 &= \vec{\phi}_1, \\
\vec{\varphi}_2 &= \vec{\phi}_2 - \vec{\varphi}_1(\vec{\varphi}_1^* \cdot \vec{\phi}_2), \\
\vec{\varphi}_3 &= \boxed{\vec{\phi}_3 - \vec{\varphi}_1(\vec{\varphi}_1^* \cdot \vec{\phi}_2) - \vec{\varphi}_2(\vec{\varphi}_2^* \cdot \vec{\phi}_3)}, \\
\vec{\varphi}_4 &= \boxed{\vec{\phi}_4 - \vec{\varphi}_1(\vec{\varphi}_1^* \cdot \vec{\phi}_2) - \vec{\varphi}_2(\vec{\varphi}_2^* \cdot \vec{\phi}_3)} - \vec{\varphi}_3(\vec{\varphi}_3^* \cdot \vec{\phi}_4), \\
\vec{\varphi}_5 &= \boxed{\vec{\phi}_5 - \vec{\varphi}_1(\vec{\varphi}_1^* \cdot \vec{\phi}_2) - \vec{\varphi}_2(\vec{\varphi}_2^* \cdot \vec{\phi}_3)} - \vec{\varphi}_3(\vec{\varphi}_3^* \cdot \vec{\phi}_4) - \vec{\varphi}_4(\vec{\varphi}_4^* \cdot \vec{\phi}_5),
\end{aligned}
\tag{3.19}
$$

where $\vec{\phi}_1$ represents an orbital function before orthogonalization and $\vec{\varphi}_1$ represents an orthogonalized orbital function. The standard Gram-Schmidt process orthogonalizes orbital functions one by one; therefore, calculations cannot be performed in parallel at the orbital function level. The main parts of this method are vector-vector multiplication and matrix-vector multiplication, which do not use the cache memory of current computers effectively, resulting in poor computational efficiency. By using matrix-matrix multiplication in the area of equation (3.19) shaded in gray, the calculations can be performed effectively using cache memory, thus improving the computational efficiency and accelerating Gram-Schmidt orthogonalization. The shaded area in equation (3.19) is calculated as

$$\left(\vec{\phi}_3, \vec{\phi}_4, \vec{\phi}_5\right) - \left(\vec{\varphi}_1, \vec{\varphi}_2\right) \begin{pmatrix} {}^t\vec{\varphi}_1^* \\ {}^t\vec{\varphi}_2^* \end{pmatrix} \left(\vec{\phi}_3, \vec{\phi}_4, \vec{\phi}_5\right), \qquad (3.21)$$

which is replaced by two matrix-matrix multiplication calculations. This matrix-matrix multiplication can be partly computed in parallel. Use of the mathematical library BLAS (Basic Linear Algebra Subprograms) for matrix-matrix multiplication allows the efficient use of cache memory by blocking the matrix elements. The performance of some computers can reach 90% or more of their theoretical performance in executing the matrix-matrix multiplication.

In solving the Kohn-Sham equation, it was common to solve the Kohn-Sham orbital as a wave function via Fourier transform. Because it is difficult for distributed-memory-type parallel computers to calculate the Fourier transform efficiently, solving the Kohn-Sham orbital as real-space data and using the difference calculation became an attractive alternative. The difference calculation using real-space data is easy to parallelize by space division and is compatible with distributed-memory-type parallel computers only via communication between adjacent nodes.

The RSDFT method treats the Kohn-Sham orbital and Hartree field as mesh point data with real-space coordinates. We solve the Laplace equation using the precise finite difference method. In this method, high-order differentiation is expressed as $\sum_{n=-1}^{N} C_n f(x + nh)$, where

$$f(x + nh) = \sum_{m=0}^{\infty} \frac{(nh)^m}{m!} D^m f(x) \quad \left(D = \frac{\mathrm{d}}{\mathrm{d}x}\right) \qquad (3.22)$$

by Taylor expansion. For example, the second derivative is

$$h^2 D^2 f(x) = \sum_{n=-N}^{N} C_n f(x + nh)$$

$$= \sum_{n=-N}^{N} C_n \sum_{m=0}^{\infty} \frac{(nh)^m}{m!} D^m f(x) \qquad (3.23)$$

$$= \sum_{m=0}^{\infty} \left[\frac{1}{m!} \sum_{n=-N}^{N} C_n n^m\right] h^m D^m f(x),$$

which becomes

$$m = 0, \sum_{n=-N}^{N} C_n = 0$$

$$m = 1, \sum_{n=-N}^{N} nC_n = 0$$

$$m = 2, \sum_{n=-N}^{N} \frac{n^2}{2} C_n = 1 \qquad (3.24)$$

$$3 \le m \le 2N + 1, \sum_{n=-N}^{N} \frac{n^m}{m!} C_n = 0.$$

It is possible to determine C_{-N} from C_N by simultaneously solving equation (3.24). The order of error is $O(h^{2N+2})$. For example, when $N = 1$,

$$\begin{pmatrix} 1 & 1 & 1 \\ -1 & 0 & 1 \\ 1/2 & 0 & 1/2 \end{pmatrix} \begin{pmatrix} C_{-1} \\ C_0 \\ C_1 \end{pmatrix} = \begin{pmatrix} 0 \\ 0 \\ 1 \end{pmatrix}$$

$$\begin{pmatrix} C_1 \\ C_0 \\ C_1 \end{pmatrix} = \begin{pmatrix} 1 \\ -2 \\ 1 \end{pmatrix}. \qquad (3.25)$$

Therefore, $f(x + h) - 2f(x) + f(x - h) = h^2 f''(x)$. In the DFT method, a fourth-order difference calculation ($N = 4$) is performed. The precision of the numerical calculation is affected when the order is small, but generally, fourth-order accuracy is sufficient.

A fourth-order difference calculation is performed using nine data points in the one-dimensional direction, and one lattice point is calculated using the 25 data points in the three-dimensional case. For a large-scale calculation, the number of lattice data points needed increases, so the difference calculation must be accelerated. The difference calculation of lattice point data has been used in various fields and has been accelerated. Generally, in difference calculations, access to an array of lattice point data often determines the calculation speed. Access to data is not a problem for one-dimensional calculations, but for three-dimensional calculations, access to the additional two-dimensional data is not continuous, thus decreasing the utilization ratio of the cache

memory. In a typical computer, continuous access to memory data is fast when the order of access is known in advance. To speed up the difference calculation, data must be as accessible as possible.

The DFT calculation used in this study targets the cluster system under free boundary conditions. The orbital function data are considered lattice point data in the system box; however, only lattice point data inside the sphere of a certain radius centered on the ions is considered. The orbital function outside the sphere is the boundary condition and the electron density is assumed zero. The lattice point data outside the sphere are not considered to reduce the amount of data to be handled and the amount of memory used. The data inside the sphere are handled as a one-dimensional rather than a three-dimensional array. Therefore, for a difference calculation, the index positions of the one-dimensional and three-dimensional arrays must correspond. The calculation of one data point requires access to 24 points in the three-dimensional array. Three indices of the three-dimensional array must be obtained from the index of the one-dimensional array and a one-dimensional index must be obtained using three indices. The difference calculation is performed repeatedly using the CG method to calculate the Kohn-Sham equation. In the DFT calculation, the size and position of the lattice point data of the orbital function do not change, so the index of the array required for the difference calculation is fixed. Therefore, if the necessary position is calculated in the difference calculation at the beginning of the program run, then list access can be reduced. As a result, a one-point difference calculation can be performed by accessing only 24 points in the one-dimensional position list, and the number of list accesses is reduced by one fourth, thus speeding up the computation.

4 Hybrid Quantum-Classical Simulation

Hybrid quantum mechanical (QM)-classical (CL) simulation divides the system into regions and performs dynamic simultaneous parallel simulation of the regions by applying quantum interaction and empirical interaction. The quantum interaction considers the electronic state via a first-principle calculation such as the DFT. The region in which quantum interaction occurs is called the QM region and an atom in the QM region is called a QM atom. The region in which the empirically derived interaction is used, i.e., the region that remains after excluding the QM region from the entire system, is called the CL region and an atom in the CL region is called a CL atom.

The problem with the hybrid QM-CL simulation is the method used to connect the two regions. At first, the ONIOM method was used to represent the total energy of the whole system comprising multiple regions. Therefore, the energy of the whole system in the hybrid QM-CL method is expressed as

$$H(\{\vec{r}\}, \{\vec{p}\}) = H_{\text{CL}}^{\text{system}}(\{\vec{r}\}, \{\vec{p}\}) + \sum_{\text{cluster}}\left(E_{\text{QM}}^{\text{cluster}} - E_{\text{CL}}^{\text{cluster}}\right), \qquad (4.1)$$

where $\{\vec{r}\}$ and $\{\vec{p}\}$ represent the set of all atomic positions and momenta, respectively. $H_{\text{CL}}^{\text{system}}$ is the classical Hamiltonian of the whole system and comprises the terms for kinetic energy and potential energy, i.e., $H_{\text{CL}}^{\text{system}} = E_{\text{kin}}(\{\vec{p}\}) + E_{\text{CL}}^{\text{system}}(\{\vec{r}\})$. There can be more than one QM region. $E_{\text{QM}}^{\text{cluster}}$ is the potential energy of the quantum (QM) calculation for the QM region and $E_{\text{CL}}^{\text{cluster}}$ is the potential energy of the classical (CL) calculation with respect to the QM region. The summation term of equation (4.1) can be thought of as replacing the classical calculated potential energy with the quantum calculated potential energy for the QM region. The set of atomic positions in the QM region used in CL and QM calculations is expressed as $\{r_{\text{QM}}\}$.

Several methods for connecting the CL region with the QM region have been proposed: the link-atom method and the modified version of the buffered-cluster method.[1] In this study, we used the buffered-cluster method. How to handle the surface of the cluster system in the QM region in the QM calculation and the CL calculation that performs the calculation with the left side of equation (4.1) must be considered. For this situation, the link-atom method is used in the field of molecular chemical calculation. Various methods[1] are available for fine, precise adjustment. In the link-atom method, atoms in the CL region, which were originally bonded within the entire system, are

arranged on the surface of the atomic cluster, which is the QM region. This reduces the influence of the surface in the calculation of the potential energy of the QM region. These atoms are called handshake (HS) atoms. Handshake atom coordinates are denoted by $\{r_{\text{QM}-\text{CL}}^{\text{HS}}\}$, so the potential energy of the cluster in the QM region is given by

$$
\begin{aligned}
E_{\text{QM}}^{\text{cluster}} &= E_{\text{QM}}^{\text{cluster}}\left(\{r_{\text{QM}}\}; \{r_{\text{QM}-\text{CL}}^{\text{HS}}\}\right), \\
E_{\text{CL}}^{\text{cluster}} &= E_{\text{CL}}^{\text{cluster}}\left(\{r_{\text{QM}}\}; \{r_{\text{QM}-\text{CL}}^{\text{HS}}\}\right),
\end{aligned}
\tag{4.2}
$$

where, for the calculation in the CL region, $\{r_{\text{QM}-\text{CL}}^{\text{HS}}\}$ is same as an atom in the CL region. For example, in a Si crystal, handshake atom is the position of a Si atom depends on the arrangement of the CL region. On the other hand, in the QM calculation cluster, the terminal atoms become H atoms. The H atoms combine with atoms with dangling bonds to electronically stabilize the surface. The position of the H atoms is determined by interpolating between the surface atoms of the CL calculation cluster and the coordinates $\{r_{\text{QM}-\text{CL}}^{\text{HS}}\}$ of the handshake atoms as follows:

$$
r^{\text{HS}} = \beta r_{\text{QM}-\text{CL}}^{\text{HS}} + (1 - \beta)r_{\text{QM}}, \qquad \beta = 0.66, \tag{4.3}
$$

where $\beta = 0.66$ is the distance between Si and H atoms obtained from the calculation for SiH_4. Several ways determine the arrangement of H atoms that affect accuracy. The force acting on an atom is calculated as

$$
F_i = -\frac{\partial H}{\partial r_i} = F_{\text{CL},i}^{\text{system}} + \sum_{\text{cluster}} \left(F_{\text{QM},i}^{\text{cluster}} - F_{\text{CL},i}^{\text{cluter}}\right), \tag{4.4}
$$

where

$$
\begin{aligned}
F_{\text{CL},i}^{\text{system}} &= -\frac{\partial E_{\text{CL}}^{\text{system}}}{\partial r_i}, \\[4pt]
F_{\text{QM},i}^{\text{cluster}} &= -\frac{\partial E_{\text{QM}}^{\text{cluster}}}{\partial r_i}, \\[4pt]
F_{\text{CL},i}^{\text{cluster}} &= -\frac{\partial E_{\text{CL}}^{\text{cluter}}}{\partial r_i}.
\end{aligned}
\tag{4.5}
$$

For example, the force on a handshake atom in the QM region is given by

$$
\begin{aligned}
\frac{\partial E_{\text{QM}}^{\text{cluster}}}{\partial r_{\text{QM}-\text{CL}}^{\text{HS}}} &= \left(\frac{\partial E_{\text{QM}}^{\text{cluster}}}{\partial r^{\text{H}}}\right)\left(\frac{dr^{\text{H}}}{dr_{\text{QM}-\text{CL}}^{\text{HS}}}\right), \\[4pt]
\frac{\partial E_{\text{QM}}^{\text{cluster}}}{\partial r_{\text{QM}}} &= \left(\frac{\partial E_{\text{QM}}^{\text{cluster}}}{\partial r_{\text{QM}}}\right)_{r^{\text{H}}\text{fixed}} + \left(\frac{\partial E_{\text{QM}}^{\text{cluster}}}{dr^{\text{H}}}\right)\left(\frac{dr^{\text{H}}}{dr_{\text{QM}}}\right).
\end{aligned}
\tag{4.6}
$$

In the link-atom method, the accuracy of the connection between the regions is affected

by the position of the H atoms. The link-atom method has two problems: The selection of the QM region is limited because the surface of the selected QM region limits the position of the terminating atom, and the type of atom being handled can make the selection of a terminating atom difficult. For these reasons, the buffered-cluster method was devised for selecting a free QM region that corresponds to a system composed of various atoms.

In the buffered-cluster method, the energy term of the QM region on the right side of equation (4.6) is a function of only the position of the QM atom, as seen in the following energy equations:

$$E_{\mathrm{QM}}^{\mathrm{cluster}} = E_{\mathrm{QM}}^{\mathrm{cluster}}(\{r_{\mathrm{QM}}\}), \tag{4.7}$$

$$E_{\mathrm{CL}}^{\mathrm{cluster}} = E_{\mathrm{CL}}^{\mathrm{cluster}}(\{r_{\mathrm{QM}}\}). \tag{4.8}$$

For both the QM calculation and the CL calculation for the QM region [equations (4.7) and (4.8)], buffer atoms at the QM-CL boundary are placed at the broken bonds of the QM atoms, thus terminating and stabilizing the electron orbit of the dangling bonds. For the CL calculation of the QM region [equation (4.8)], the buffer atoms are Si because they mimic the original bond at the QM-CL boundary. The buffer atoms are where the potential energy is minimal under the constraint in which the $\{r_{\mathrm{QM}}\}$ of the QM atoms in the cluster region is fixed. This is done each time $\{r_{\mathrm{QM}}\}$ is changed to simulate the potential energy $E_{\mathrm{CL}}^{\mathrm{cluster}}$. Therefore, in the buffered-cluster method, the position of the buffer atoms may be different from the CL atom coordinates in the whole system. Here, the Si buffer atom interacts with the Si atom of the binding pair of the CL atom in the whole system via the SW potential of the atom. In the buffered-cluster method, the buffer atom associated with the QM calculation of the QM region [equation (4.7)] is either H or Si depending on the original bonding characteristic of the Si system. For the QM calculation, the position of the H buffer atom is determined by the position of the buffer atom of the atomic cluster used for the CL calculation. For the atomic clusters used for the CL calculation, H buffer atoms are placed for each Si buffer atom located at $r_{\mathrm{CL}}^{\mathrm{buffer}}$ and connected to r_{QM}, within the atomic cluster for the QM calculation, with the scale factor of $\beta = 0.66$.

In the buffered-cluster method, the force on atom i in the QM region is given by

$$F_i = -\frac{\partial H}{\partial r_{\mathrm{QM},i}} = -\frac{E_{\mathrm{CL}}^{\mathrm{system}}}{\partial r_{\mathrm{QM},i}} - \sum_{\mathrm{cluster}} \left(\frac{\partial E_{\mathrm{QM}}^{\mathrm{cluster}}}{\partial r_{\mathrm{QM},i}} - \frac{\partial E_{\mathrm{CL}}^{\mathrm{cluster}}}{\partial r_{\mathrm{QM},i}} \right) \tag{4.9}$$

where

$$\frac{\partial E_{\text{QM}}^{\text{cluster}}}{\partial r_{\text{QM},i}} = \left(\frac{\partial E_{\text{QM}}^{\text{cluster}}}{\partial r_{\text{QM},i}} \right)_{\text{fix}\{r_b\}} + \sum_{j}^{\text{cluster}} \frac{\partial E_{\text{QM}}^{\text{cluster}}}{\partial r_{b,j}} \left(\frac{\partial r_{b,j}}{\partial r_{\text{QM},i}} \right)_{\text{CL}},$$

$$(4.10)$$

$$\frac{\partial E_{\text{CL}}^{\text{cluster}}}{\partial r_{\text{QM},i}} = \left(\frac{\partial E_{\text{CL}}^{\text{cluster}}}{\partial r_{\text{QM},i}} \right)_{\text{fix}\{r_b\}}.$$

The force on atom i in the CL region is given by

$$F_i = \frac{\partial E_{\text{CL}}^{\text{system}}}{\partial r_{\text{CL},i}}. \tag{4.11}$$

In the buffered-cluster method, the position of the buffer atom in the QM calculation of the atomic cluster is determined by using the position of the buffer atom obtained by the CL calculation of the atomic cluster. Since $E_{\text{QM}}^{\text{cluster}}$ and $E_{\text{CL}}^{\text{cluster}}$, defined by equations (4.7) and (4.8), respectively, are not dependent on the position of the CL atom, $\{r_{\text{CL}}^{\text{cluster}}\}$, the DFT energy $E_{\text{QM}}^{\text{cluster}}$ of the atomic cluster is minimized by stabilizing the buffer atom at the QM atom. Because the structure of a crystal undergoes undesired deformation, the accuracy of the buffered-cluster method when applied to Si crystals with various choices of clusters is analyzed with respect to atomic position, atomic force, and electronic structure. Unlike the link-atom method, the buffered-cluster method can be applied to ionic materials such as alumina using long-range empirical interaction potential.

1)   S. Ogata, Phys. Rev. B **72**, 045348 (2005).

5 Visualization of Complex Simulation Data

In this research, we report on a file data format for visualization of simulation results and its visualization software as research on the hybrid quantum (QM)-classical (CL) simulation[1-3]. The hybrid QM-CL simulation is a Molecular Dynamics (MD) simulation that combines a classical MD calculation region handling atoms and an electronic state calculation region handling ions and electrons, and these result data are particle data representing atoms and ions and lattice point data representing the electronic density. In data analysis of this simulation, it is necessary to visualize these two results data efficiently. It is common to handle particle data and lattice point data separately so far, and in the result of the hybrid QM-CL simulation, when it is desired to handle these data together, problems arise due to convenience. Therefore, in order to facilitate visualization of the hybrid QM-CL simulation, these problems were solved by developing a file format combining particle data and lattice point data. Furthermore, we have developed a visualization software to read these files and visualize these data.

5.1 Visualization for Simulation with High Performance Computer

Researches and developments by a computer simulation of a material simulation are progressing due to improvement in computational performance of the computer. The computer simulation has become the practical tool due to expansion of system size handled by computer simulation and improvement of computation accuracy. As the computer simulation becomes larger and widely used, utility tools supporting simulation run are increasingly important. Especially researches and developments for making input data of simulation, analyzing simulation result and visualization make it easier to use.

In the field of computer simulations, visualizations are important methods as one of analysis methods of results. In the observation of natural phenomena and the measurement of experiments, the transition and change are quantified. On the other hand, in computer simulation, numerical data is obtained by simulating on a computer based on a numerical model. This result will be compared with experimental measurement data. In addition, the simulation imagines a phenomenon that cannot be seen in experiments and the like, and can model it and perform a virtual experiment. In such a case, by visualizing the simulation result, it is possible to intuitively understand the phenomenon of the simulation as compared with what is actually seen or compared with the imagined image.

For example, when a simulation system is in equilibrium state, it is possible to comprehend by statistically quantified data, but in non-equilibrium state, it is necessary to see the phenomenon change carefully, so it is difficult to understand with only numerical data. In the nanoscale simulation, when viewing the structure of the molecule and the reaction path of the chemical reaction, the analysis by visualization is thought to help many understanding of the phenomenon.

The computer simulation consists of preprocess such as initial settings such as model setting, execution of iterative calculation based on the model, and postprocess that analyzes the result obtained. The execution of the simulation has been made larger and faster by the use of super computer like parallel computers. On the other hand, preprocess and postprocess are often performed by local computers. As the data handled in the simulation becomes larger and more complicated, efficiency of preprocess and postprocess for simulation becomes more important.

In recent years, supercomputers, which are computers for scientific technology fields with high computational performance, are advancing large-scale parallel computers. According to TOP 500[4] which announces ranking of supercomputer performance using the Linpack benchmark, the supercomputer performance has improved exponentially up to now. The supercomputer has become a distributed memory type parallel computer networked with many nodes equipped with many CPUs and accelerators such as GPU. Therefore, in the simulation, the space division method, which is a parallelization method suitable for a distributed memory type parallel computer, has come to be widely used. The space division method is a method of dividing data into real spaces and allocating them to parallel computers for calculation. The parallel computation by real space division is suitable for distributed memory type parallel computing machine because there are few communication processes between nodes which are bottlenecks in the parallel computer. In parallel computers, various methods are used to simulate with high accuracy with a realistic model.

The hybrid simulation is a method of dividing the entire system into partial regions and applying a simulation method of different accuracy to perform a large-scale simulation. Electronic state calculation is performed in a region where chemical reaction occurs, and other regions are calculated by an atomistic model. By applying appropriate precision calculation to the divided region, the large-scale simulation with high calculation efficiency is enabled. In hybrid QM-CL simulation, the classical region

calculation based on the atomistic model and the quantum region calculation by the electron and ion model are performed in parallel and the time evolution is performed by the MD method.

The MD simulation is a particle simulation in which atoms are treated as mass points and particle position information is updated by Newton's equation of motion by numerical integral method such as the Verlet method by interaction between atoms. Since atoms have position data and velocity data, they have six floating point number data in three-dimensional space. Furthermore, information data such as particle type and physical quantity may be added. Electronic state calculations calculate the state of electrons around ions. Electrons are handled as the electronic density and have values as lattice point data in real space.

The result of a hybrid QM-CL simulation has classical region has atomic positions data, and the quantum region has ionic positions data and lattice point data of electronic density by electronic state calculation. In the visualization of the result of the hybrid QM-CL simulation, the whole system is visualized by atomistic system or only the quantum region is taken out to visualize the ion and electronic density together.

Visualization of MD simulation, which is a classical region, generally shows atomic particles as spheres and visualizes the bonds by stick display. On the other hand, in the electronic state calculation, visualization is made by combining ionic particles and lattice point of electronic density. In this case, the ions are placed in the system box. The electronic density has data on lattice point of the entire box. There is many software to visualize such particle system data and electronic density data, and various functions can be used in visualization.

In the case of visualization as a hybrid QM simulation, it is necessary to visualize lattice point data of electronic density by electronic state calculation applied to a part of regions for data of a large-scale particle system, Visualization by combining different data formats for regions is desired. However, it is difficult to visualize such result data. In the hybrid QM-CL simulation, since there is a large particle system and a part of the region is calculated by electronic state calculation, if lattice point data of electronic density is set with reference to the entire space of particle system, the number of lattice point data is huge It is inefficient to visualize it. There is also a method of handling particle data and lattice point data separately and displaying them overlapping at the time of visualization. In that case, it is necessary to arrange where to place the region of the lattice point data

in the particle system region. It is difficult to handle this because it is necessary to manage and add information. A file format that simultaneously handles visualization of particle data and electronic density data is necessary in domain segmentation simulation such as hybrid QM-CL simulation.

Therefore, in order to easily visualize the hybrid QM-CL simulation, we propose a file format for visualization in which particle data of atomic position and lattice point data of electronic density are combined into one. Together with formulation of data format for visualization, we developed a visualization software to read and visualize the file of the data format formulated this time.

5.2 Visualization of Hybrid Quantum-Classical Simulation

The hybrid QM-CL simulation used in this study is a MD simulation consisting of two calculation methods. The system is divided into regions, and quantum regions using the electronic density functional theory (DFT) and classical regions using empirical interaction are applied. The quantum region treats electrons as density data on real space lattice point. The classical region treats the position of an atom as particle data. In the visualization of the hybrid QM-CL simulation, these two types of data are visualized in one space and progress in time.

The particle simulation such as the MD simulation is a simulation in which particles are moved based on interaction between particles, time evolution is investigated, and physical quantity is examined by statistical mechanics and the like. Generally, the particle data consists of position information and its attached information. In the three-dimensional space, the position information is vector data in tree-dimensional space and is a value obtained as a result of simulation. Electronic state calculation such as DFT treats electrons as density distributed in real space. Electronic Density is treated as data of a point divided into lattices, and lattice point data is a position regularly made in space and its attached information. When the position of the lattice points is determined regularly, the position information of the lattice points is unnecessary. In that case, information on the grid interval and the number of grids is required. The position information of lattice points is necessary at the stage of visualization.

The problem in visualizing the results of hybrid QM-CL simulation is to deal with two types of data: particle data and lattice point data. Visualization of atomic particle data and lattice point data of electronic density has been done so far. In the case of

electronic state calculation, electronic density is calculated in a space in which ions are arranged. Currently, the electronic state calculation requires a lot of time for calculation, so the size of the system to be calculated is not originally large. Therefore, particle data and lattice point data were set to the same space size for visualization. In this way, visualization of data which treats particles and electronic density together is done. However, the hybrid QM-CL simulation is a system in which the space size of the particle system is large and only a part of the region has electronic density data. In this case, if the space of lattice point data of the electronic density is matched with the space size of the particle system, the size of the lattice point data becomes enormous and cannot be handled. Although the data size is enormous, lattice points where there is no value of electronic density are spreading in the space other than the quantum region, resulting in poor efficiency. When managing particle system data and lattice point data as separate files, the region of lattice point data will be embedded in the particle system. This is troublesome because it is difficult to align the two data and the two location information are required.

5.3 Akira Format and Akira Software

In order to easily visualize the result data of hybrid QM-CL simulation, we proposed a file format for managing particle data and lattice point data of electronic density as one file. In addition, we develop software that reads and visualizes the proposed data file and release this software to the public[5]. We will call the data file for visualization of hybrid QM-CL simulation as Akira format file. The Akira format manages particle data and lattice point data in one file. For the data of the whole system, the lattice point data is added to the particle data. The lattice point data is composed of the starting position of the lattice point data, the interval of the lattice points, the number of lattice points and values on lattice points. A hybrid QM-CL simulation sometimes handles a plurality of quantum regions. Therefore, in the Akira format, it is possible to have lattice point data of a plurality of regions. The Akira format makes visualization easy by treating it as one file including information necessary for visualization of the hybrid QM-CL simulation. We also developed a software to read the file of Akira format and visualize the result of hybrid QM-CL simulation. Visualization software Akira reads the particle data and lattice point data of the file of Akira format, the particle data performs the ball and stick display, and the lattice point data performs the isosurface and volume rendering display. This

visualization software is publicly available[6], and anyone can use it.

The visualization software Akira consists of a conversion program that performs a preprocess for visualization and a visualization program that performs a display. The conversion program that performs a preprocess for visualization reads a file of Akira format which is simulation result data, and creates an intermediate file of data that is easy to handle in the visualization program. The visualization program which performs a display reads and displays the intermediate file created by the conversion program.

The preprocess conversion program reads simulation result data and creates an intermediate file converted into data suitable for visualization. This process is done to make data easy to handle with the visualization software. For example, it converts double precision floating point number data to single precision floating point number to reduce the data size, or combines multiple files of time-series data into one file. In addition, this process performs analysis of data and filter process for narrowing down the targets to be visualized. Intermediate files are created as binary files to reduce data size and speed up reading.

Since these preprocesses can be executed on the supercomputer, it can be performed at high speed. The preprocess on the supercomputer does not require moving a large number of files output by simulation to the local computer. In the visualization program, by reading preprocessed data, speeding up from reading of file to visualization is done. In addition, the initial time of visualization and repetitive process are shortened. In visualization, animation can be displayed by reading time series data. In addition, display of particles can be performed with a color corresponding to the physical quantity of particles.

Visualization software Akira has been developed to operate on general OS such as Windows, Mac and Linux. In the visualization program, GUI parts and file process are written using Java language. For graphics process, we use the OpenGL[7] which is the widely-used graphics library. The OpenGL is capable of hardware process with many GPUs and process is fast. We use JogAmp[8] to use OpenGL from Java. The developed software Akira is published on the web.

5.4 Visualization Example

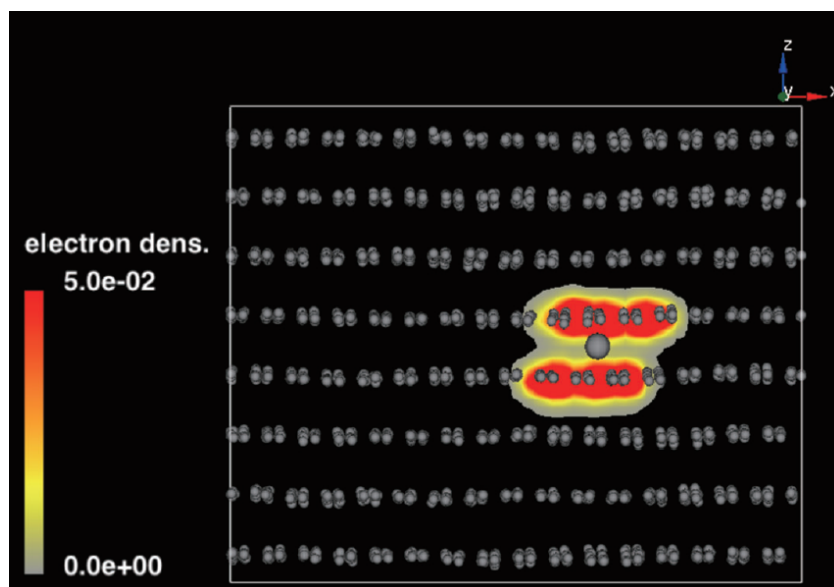An example of visualization of hybrid QM-CL simulation is shown in Figure 5.1.

Figure 5.1. The visualization of the results of a hybrid QM-CL simulation on Li between graphite layers is shown. The atoms of the whole system are indicated by spheres. The QM region handled in the DFT calculation is selected around Li ions. Since the QM region has electronic density data of grid data, the electronic density is indicated by color contour display.

In the hybrid QM-CL simulation, the calculation of the quantum region does not simply calculate the partial system. We calculate the cluster system by extracting the quantum region and adding terminal atoms and buffer atoms for stabilizing the boundary electronic state. Therefore, the electronic density obtained by the electronic state calculation is the electronic density including the terminal atoms and the buffer atoms, which is different from the electronic density of the quantum region. Therefore, in visualization of hybrid QM-CL simulation, it is not accurate to simply display lattice data superimposed on particle data. Originally it is desirable to display from the electronic density excluding the electronic data around the terminal atoms and buffer atoms.

5.5 Summary

In recent years, the computer simulation has grown in scale due to the improvement of computer performance. In the supercomputer field, large-scale parallel computers in which a large number of computer nodes are network-connected in parallel are mainstream. In parallel computers, large-scale simulation and long-term simulation are performed by parallelization by space division. In this way, the size of the simulation result data becomes enormous.

In a large-scale simulation using a large-scale parallel computer, the data to be stored is enormous. For example, in simulations using three-dimensional lattice data, the number of lattice points is on the scale of thousands of thousands. In the simulation of particle systems, it is on the order of hundreds of millions of large ones. When handling data of $4000 \times 4000 \times 4000$ lattice points of double precision floating point number data (8 bytes), the result data of one time is 512 GBytes of data size. In the case of time series data of a plurality of times, the data size is multiplied by the step number.

Generally, large-scale simulations are executed by large-scale supercomputers located in a remote place. On the other hand, when visualizing or analyzing, it is common to move the result data of the simulation to a local computer. This is because analysis and visualization of data are often performed interactively. In the case of large-scale simulation, since the result file is enormous, it is becoming difficult to move data to the local computer from the data storage capacity of the local computer and the data communication speed of the network. As a result, it is becoming difficult to analyze and visualize the results of large-scale simulation.

In order to solve such a problem, it is also studied to perform analysis and visualization simultaneously with execution of simulation on a remote supercomputer located in a remote place. Other studies are also being conducted to reduce the size of the simulation result data. In some applications where visualization of simulation results is used, some high precision numerical data are not required, so research is being made to reduce the data size with low precision data and use it for visualization. For example, by changing floating point number data from double precision to single precision, the data size is reduced.

Hagita and colleagues propose a method of compressing data. This method is the jointed hierarchical precision compression number-data format (JHPCN-DF)[9]. This method compresses data by discarding bit information of small digits according to

necessary precision in the data structure of floating point number. In floating point notation, the least significant bit of the mantissa relates to the precision number of floating point number. The characteristic of JHPCN-DF is that accuracy can be adjusted. Cutting off the lower bits with zero, or performing other compression such as zip will result in large compression. For remote controllers etc., it is suitable to store and use highly accurate data and use local computers to transfer data with reduced precision from supercomputer for visualization.

In the long-term simulation, the resultant time series data becomes enormous. In order to reduce the amount of time series data, the frequency of storing data is reduced, but it is related to the quality of data, so it cannot easily be reduced. With respect to the visualization of the simulation result, it is possible to display it as smooth data by using interpolated data at the time of visualization by using data of a large time interval.

In this research, in order to easily visualize hybrid QM-CL simulation, we proposed a data format Akira for visualization. We have developed a visualization software that visualizes data in Akira format. In the Akira format, in order to efficiently visualize particle data and lattice point data which are result data of hybrid QM-CL simulation, particle data and lattice point data of electronic density are managed in one file collectively. Furthermore, Akira visualization software to read and visualize data of Akira format was developed and made public. Akira software program consists of preprocess program for converting data and program for visualization. In addition to the Akira format, Akira program can handle general MD simulation files and visualize them.

Large-scale simulation using high-performance supercomputer due to high parallelization of computers has been carried out. Although the advancement of simulation such as parallel calculation is advancing, it is also necessary to upgrade the postprocess such as analysis and visualization of the result data of the simulation. In addition, the development of utilities related to simulation such as saving of simulation result data is becoming an issue.

In the result of the hybrid QM-CL simulation, we showed the result of visualizing particle data of atoms and ions and lattice point data of electronic density as one. The particle data can be displayed by ball display or the like, and the lattice point data can be displayed together with isosurface display and volume rendering display. In the future, when the range of application of computer simulation expands and various simulations are carried out, it is considered that the number of simulations combining

52

plural calculation methods such as hybrid QM-CL method will increase. In such a case, we think that the Akira format is useful to treat plural different data as one.

1) S. Ogata, E. Lidorikis, F. Shimojo, A. Nakano, P. Vashishta, and R. K. Kalia, Comput. Phys. Commun. **138**, 143 (2001).

2) S. Ogata, F. Shimojo, R. K. Kalia, A. Nakano, and P. Vashishta, Comput. Phys. Commun. **149**, 30 (2002).

3) S. Ogata, Phys. Rev. B **72**, 045348 (2005).

4) https://www.top500.org/

5) T. Nakamura, T. Kouno, R. Kobayashi, and S. Ogata, J. Comput. Chem. Jpn., Vol. 10, No. 2, pp. 59-68 (2011).

6) https://code.google.com/archive/p/project-akira/ (2017).

7) https://www.opengl.org/

8) https://jogamp.org/

9) K. Hagita, M. Omiya, T. Honda, and M. Ogino, SC14 Poster, 2014

6 Activation Energy for Oxygen Diffusion in Strained Silicon: A Hybrid Quantum-Classical Simulation Study with the Nudged Elastic Band Method

6.1 Introduction and Preparatory Examination

Impurities of a variety of species such as O, P, and B are introduced naturally or intentionally in Czochralski (Cz)-grown Si crystals. Among others O is the most important and common impurity,[1] which stems from the quartz crucible through its partial dissolution into the Si melt at high temperatures $T \sim 1,800$ K. Most O atoms exist in Si crystal as interstitials that occupy puckered bond-center sites of two neighboring Si atoms aligning along $\langle 111 \rangle$ direction. Because of decreased solubility of O in Si at lower temperatures, annealing of Cz-Si produces aggregates of O that range in size from nanometers to micrometers. At $T = 700\text{-}800$ K, small clusters of O and Si that contain up to tens of O atoms are formed, which are referred to as the thermal double donors (TDD)[2] because of their electrical activity. At higher temperatures, there appear large-scale O precipitates accompanied by structural defects.[1]

Controlling diffusivity of a selected impurity-species in Cz-Si is one of the engineering challenges to which many semiconductor institutes have been addressing, to create advanced LSI devices. In general, external stress affects the impurity diffusivity in a material; one may think of advancing this to control the migration behavior of impurities in Cz-Si. In the case of O in Cz-Si, it has been demonstrated by measuring the time evolution of concentration of the TDD that hydrostatic pressure $P \sim 1$ GPa enhances the O diffusion in Cz-Si significantly at $T = 720$ K.[3,4] Furthermore, understanding the stress dependence of the O diffusivity in Si is important to analyze the oxidation process of Si and also the stress corrosion cracking of Si-based materials as silica.[5] In the oxidation of Si(111), for instance, it has been observed with the TEM that the oxidation proceeds layer by layer.[6,7] Since the characteristic volume of Si doubles after the oxidation, the Si side at the SiO_2-Si boundary may experience significant un-isotropic stretch from the SiO_2 side at the oxidation. Theoretical explanation of such a unique oxidation process of the Si surface requires detailed analyses on the O migration in Si at various stress conditions.[8]

Motivated by these, in the present paper, we will investigate theoretically the change of the activation energy for O diffusion in Si crystal due to a wide range of compressive and expansive strains. As an O atom moves along a transition path in Si

crystal, the strain field produced by the O should vary accordingly. Since the strain field can be long-ranged in an elastic medium, we will consider a Si system with large enough size for accurate computation of the activation energy.

To further clarify our motivation of considering a large system, as a preparatory examination, we will investigate in this section the possible contribution of peripheral atoms (i.e., located far from the O atom) to the O activation in strained Si crystal using a classical inter-atomic potential only (i.e., without using the electronic structure calculation). Since the classical inter-atomic potentials for a mixture of Si and O appropriate to the present setting are not known, we will exploit the inter-atomic potential for pure Si system. To mimic the strain field created by the O atom inserted in Si crystal, we will prepare a large Si crystal without O, and will set two or three Si atoms selected in the Si crystal to the configuration that corresponds to either the minimum or the maximum energy state along the minimum energy path (MEP) of the O transition. After relaxation of the rest atoms, we will obtain the potential energy of each atom in the system for both states. Summation of the energy difference between the two states with respect to the peripheral atoms will give us an approximate estimate of the peripheral contribution to the activation energy.

Following the procedure described above, we firstly consider the local atomic configuration in the close proximity of the inserted O in Si crystal at zero pressure predicted[9] by the density-functional theory (DFT) with the local-density approximation (LDA). Figure 6.1(a) depicts the O interstitial in the minimum energy state, which is called the "end" state; while Figure 6.1(b), in the maximum energy state (i.e., the saddle point), called the "mid" state. In Figure 6.1(a) and 6.1(b), three principal Si atoms, Si1, Si2, and Si3, reside on the same $(10\bar{1})$ plane. In the end state, the O forms a bended structure with the Si2-Si3 bond elongated. The O may rotate around the Si2-Si3 axis or penetrate the center of Si2 and Si3 easily at low pressures.[10] Former LDA-DFT calculations[9,10] have predicted that the O in Si crystal makes a transition from the end state to one of the nearby end states through the mid state. The activation energy for the O transition in Si crystal at zero pressure has been predicted to be in the range between 2.0 and 2.2 eV by the LDA-DFT calculations using the supercells.[9-12] Referring to the former LDA-DFT results,[9] we set the Si2-Si3 distance $d(\text{Si2} - \text{Si3}) = 3.20\,\text{Å}$ in the end state. On the other hand, the local configuration of the mid state contains ambiguity.

We therefore consider three possible situations for the mid state: $\big(d(\text{Si}1-\text{Si}2), d(\text{Si}2-\text{Si}3), d(\text{Si}1-\text{Si}3)\big) = (2.90\,\text{Å}, 2.90\,\text{Å}, 4.74\,\text{Å})$, $(2.74\,\text{Å}, 2.74\,\text{Å}, 4.32\,\text{Å})$, $(2.57\,\text{Å}, 2.57\,\text{Å}, 3.91\,\text{Å})$, which correspond to $\theta = 109.5°$, $104.5°$, and $98.8°$, respectively.
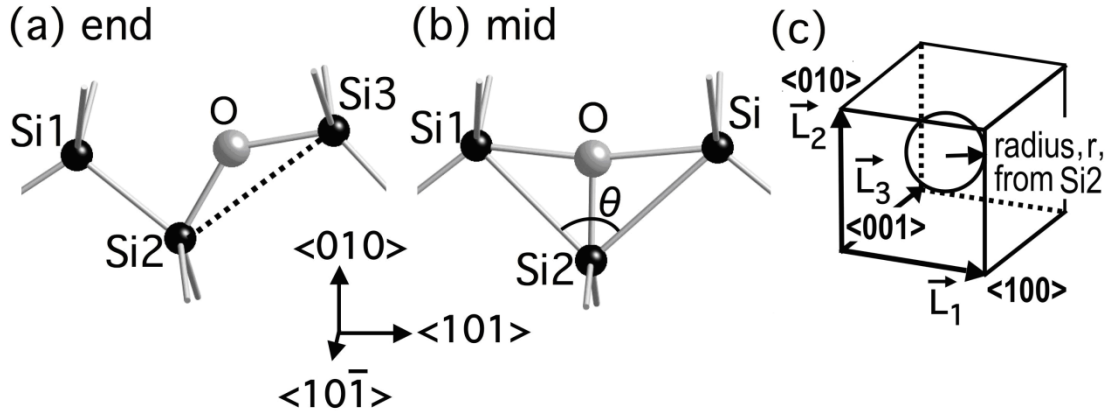

Figure 6.1. (a) The end state of the O transition in Si. (b) The mid state of the O transition in Si. (c) Schematic view of the total system.

Secondary we prepare a Si crystal under the periodic boundary conditions (PBC) with the three simulation-box vectors $\{\mathbf{L}_1, \mathbf{L}_2, \mathbf{L}_3\}$ parallel to $\{\langle 100\rangle, \langle 010\rangle, \langle 001\rangle\}$, as shown in Figure 6.1(c); the system assumes a cube with $L_1 = L_2 = L_3 \approx 130\,\text{Å}$ at zero strain, and the total number of Si atoms is 110,592. We use the Stillinger-Weber (SW)[13] inter-atomic potential for Si. To mimic either configuration of Si1, Si2, and Si3 for the end or the mid state, we pick up three Si atoms at around the center of the system [see Figure 6.1(c)]. The $d(\text{Si}2-\text{Si}3)$ is fixed in the end state; while $\big(d(\text{Si}1-\text{Si}2), d(\text{Si}2-\text{Si}3), d(\text{Si}1-\text{Si}3)\big)$ are fixed in the mid state. For each state, we relax all other Si atoms to the minimum energy configuration. We thereby find $d(\text{Si}1-\text{Si}3) = 4.30\,\text{Å}$ in the end state. The contribution of the peripheral atoms to the activation energy is evaluated as:

$$\Delta E_{\text{periph}}(r) = \sum_{r_i-r}^{\text{atoms}}\left(e_i^{\text{mid}} - e_i^{\text{end}}\right), \tag{6.1}$$

where e_i^{state} is the potential energy of atom-i for each state and r_i is the distance of atom-i measured from Si2 in the mid state. Irrespective of the setting of $\left(d(\text{Si1} - \text{Si2}), d(\text{Si2} - \text{Si3}), d(\text{Si1} - \text{Si3})\right)$ in the mid state, we find $\left|\Delta E_{\text{periph}}(r)\right| <$ 0.01 eV at $r \geq 10\,\text{Å}$, that is, negligible contribution of the peripheral atoms (see the dotted curves in Figure 6.2).
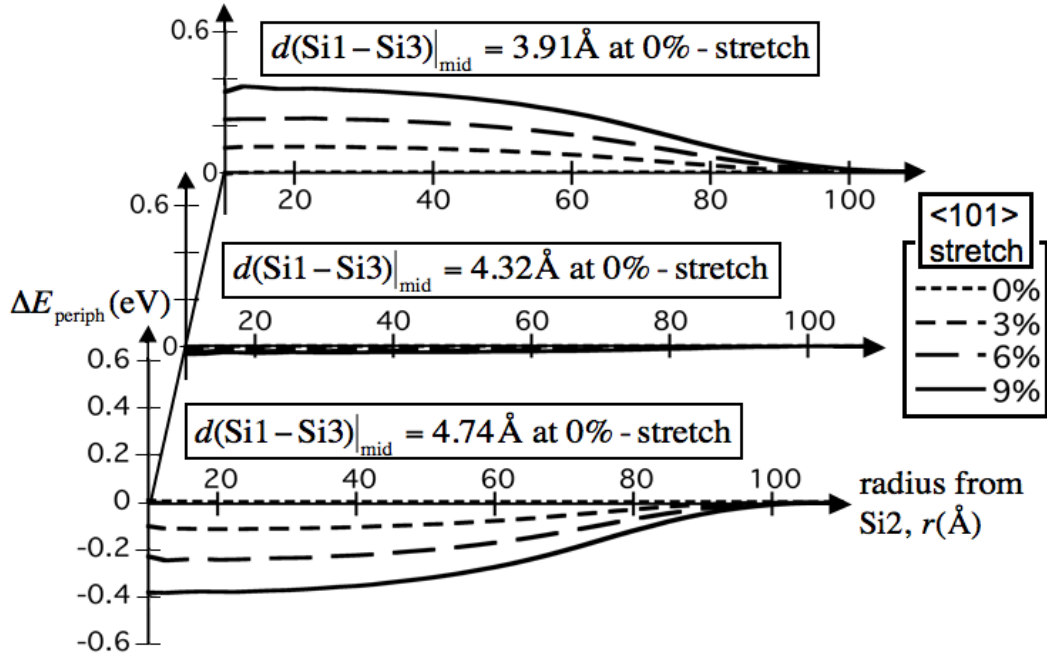

Figure 6.2. The $\Delta E_{\text{periph}}(r)$ in $\langle 101 \rangle$-case calculated using the classical inter-atomic potential for Si. The $\{0\%, 3\%, 6\%, 9\%\}$-stretches are considered for three settings of $\left(d(\text{Si1-Si2}), d(\text{Si2-Si3}), d(\text{Si1-Si3})\right)$, denoted simply with $d(\text{Si1-Si3})$ at 0%-stretch, in the mid state.

Thirdly we investigate possible effects of system stretch on $\Delta E_{\text{periph}}(r)$. Three stretch-directions are considered: $\langle 101 \rangle$, $\langle 010 \rangle$, and $\langle 10\bar{1} \rangle$. In each case, uni-axial

stretches of 3%, 6%, and 9% are applied to the system by changing the simulation box vectors. The same degree of uni-axial stretch is applied to $d(\text{Si2} - \text{Si3})$ in the end state, and to $\left(d(\text{Si1-Si2}), d(\text{Si2-Si3}), d(\text{Si1-Si3})\right)$ in the mid state, assuming similar stiffness of those bonds to that of the other Si-Si bonds in the system. Then the atomic positions are relaxed under the constraints. The calculated values of $\Delta E_{\text{periph}}(r)$ are substantial only in $\langle 101 \rangle$-case as plotted in Figure 6.2, which are about one order of magnitude larger than those in $\langle 010 \rangle$- and $\langle 10\bar{1} \rangle$-cases. The $\Delta E_{\text{periph}}(r)$ approaches to a constant as r decreases to about 10 Å, which we call the peripheral energy $\Delta E_{\text{periph}}^*$. Though the magnitudes of $e_i^{\text{mid}} - e_i^{\text{end}}$ are relatively large at small r_i, they contribute little to $\Delta E_{\text{periph}}^*$ since the number of the atoms is small. We find for $\langle 101 \rangle$-case in Figure 6.2: (i) the magnitude of $\Delta E_{\text{periph}}^*$ increases in proportion to the stretch, which is nearly zero at 0%-stretch, (ii) the $\Delta E_{\text{periph}}^*$ ranges between -0.40 and 0.40 eV at 9%-stretch for three settings of $\left(d(\text{Si1} - \text{Si2}), d(\text{Si2} - \text{Si3}), d(\text{Si1} - \text{Si3})\right)$ in the mid state. We here note that the convexity of all the curves of $\Delta E_{\text{periph}}(r)$ changes at $r \sim 70$ Å as seen in Figure 6.2, which corresponds to the half of the simulation box size. To confirm that the present system has a large enough volume, we also consider a five times larger simulation-volume for $\langle 101 \rangle$-case. We thereby find that $\Delta E_{\text{periph}}^*$ changes little (~ 0.01 eV) by such a size change, while the shape of $\Delta E_{\text{periph}}(r)$ appears to scale to the simulation box size.

The (i) in the last paragraph may be understood as follows. The stretch applied to the system creates a uniform strain field in the system if inhomogeneity relating to the three Si atoms, Si1, Si2, and Si3, is ignored. The constrained configuration of the three Si atoms adds a weak strain field, which may be independent of the system stretch and dependent on the state (i.e., mid or end) of the system. Assuming that the change of the energy of atom-i, e_i^{state}, is proportional to the square of the local strain, we may consider that the energy difference $e_i^{\text{mid}} - e_i^{\text{end}}$ is approximately proportional to the product of the uniform strain due to the system stretch and the difference of the local strain between the end and the mid states. Therefore the summation of $e_i^{\text{mid}} - e_i^{\text{end}}$, that is $\Delta E_{\text{periph}}^*$, should be proportional to the system stretch. This explains why $\Delta E_{\text{periph}}^*$ is zero at 0%-stretch and increases in magnitude in proportion to the system stretch. The (ii) in the last paragraph is because $\Delta E_{\text{periph}}^*$ varies nearly linearly as a function of the difference $\Delta d \equiv d(\text{Si1-Si3})|_{\text{mid}} - d(\text{Si1-}Si3)|_{\text{end}}$. In fact, at 9%-stretch, $\left(\Delta E_{\text{periph}}^*, \Delta d\right) =$

$(0.40 \text{ eV}, -0.452 \text{ Å})$, $(-0.02 \text{ eV}, 0.0 \text{ Å})$, and $(-0.40 \text{eV}, 0.452 \text{Å})$. Since the direction of the Si1-Si3 line is parallel to $\langle 101 \rangle$, larger $d(\text{Si1-Si3})$ in the mid state acts to relax the peripheral region further in the stretched system, resulting in smaller $\Delta E^*_{\text{periph}}$.

   In the preparatory examination explained above, we have demonstrated that if the difference Δd of order 0.1 Å exists in $\langle 101 \rangle$-stretched system (by several percent) substantial contribution of order 0.1 eV to $\Delta E^*_{\text{periph}}$ should emerge from the peripheral region. In reality, the configuration of the two or three atoms (Si1, Si2, and Si3) and therefor $d(\text{Si1-Si3})$ in a strained system are the results of interplay of the reacting central atoms and the deformed peripheral atoms. Therefore we will adopt the concurrent, hybrid simulation scheme.[14] In the hybrid scheme, a total system of Si crystal with one O atom is divided in real space; a quantum (QM) electronic-structure calculation method such as the DFT is applied to a local region around the O atom, and the classical (CL) interatomic potential such as the SW potential is applied to the rest of the system. Using the hybrid scheme we can treat the large-scale system as has been used in the preparatory examination with much higher physical accuracies. For a strained Si system, it is not known whether the mid state in Figure 6.1(b) corresponds to the saddle point in the energy surface. Therefore we will combine the hybrid QM-CL simulation method with the nudged elastic band (NEB)[15] method to investigate the energy surface profile along the MEP in a strained system.

   In Section 6.2, we explain the hybrid QM-CL simulation method and its combination with the NEB method. The simulation results and their physical explanation are presented in Section 6.3. Comparison of the present results with the relating experimental data is given in Section 6.4 with concluding remarks.

6.2 Methodology

6.2.1 Hybrid QM-CL simulation method

   We consider the same model system of Si crystal $(L_1 = L_2 = L_3 \approx 130 \text{ Å})$ under the PBC as has been used in the preparatory examination in Section 6.1, but a single O atom inserted at the center; total number of atoms $N = 110{,}593$. We have confirmed in Section 6.1 that the present system size is large enough to evaluate the peripheral energy, $\Delta E^*_{\text{periph}}$. For the hybrid QM-CL simulation, we set a QM region around the O in the system, which contains 53 Si and 1 O as depicted in case 3 in Figure 6.3. We call the atoms in the QM region as the QM atoms; the rest atoms in the system, as the CL atoms.

We adopt the SW inter-atomic potential for the CL calculation of Si. We have determined the present size of the QM region through comparison of the atomic forces for various selections of the QM region in the hybrid QM-CL simulation method (see the last paragraph of Section 2.1). We choose the DFT method for the QM calculation by considering balance between accuracy and computation speed, though any method that can describe the electronic structure of an atomic cluster may be used.
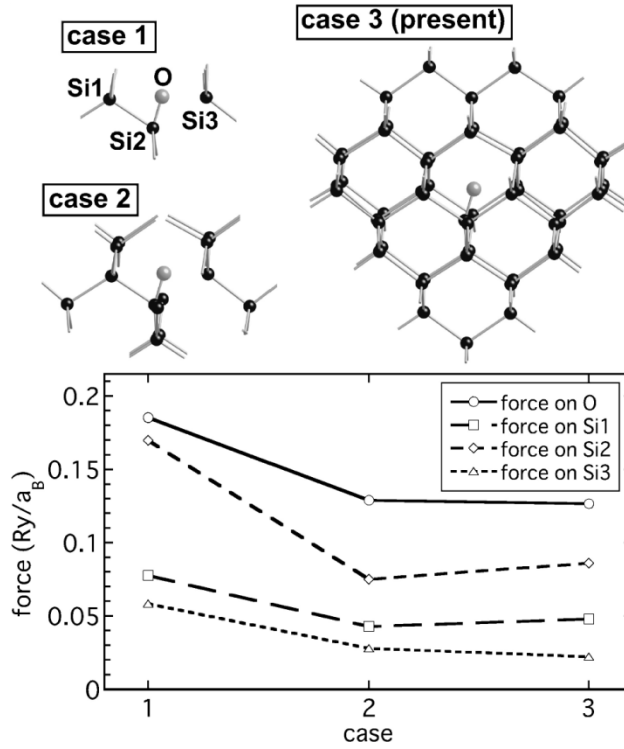

Figure 6.3. The forces on O, Si1, Si2, and Si3 atoms, in unit of Ry/a_B (a_B is the Bohr radius), calculated with the hybrid QM-CL simulation method for an intermediate configuration (NEB image $\alpha = 3$) between the end and the mid states at 9%-stretch in $\langle 101 \rangle$-case. Three cases of the QM region are considered: numbers of the QM atoms are 4 (case 1), 12 (case 2), and 54 (case 3).

We write the total energy of the hybridized system in a modular form.[16] Since

we have a single QM region in the present setting, the Hamiltonian that predicts the dynamics of all the atoms is:[17,18)]

$$H(\{\mathbf{r}\}, \{\mathbf{p}\}) = H_{\mathrm{CL}}^{\mathrm{system}}(\{\mathbf{r}\}, \{\mathbf{p}\}) + E_{\mathrm{QM}}^{\mathrm{cluster}} - E_{\mathrm{CL}}^{\mathrm{cluster}}, \qquad (6.2)$$

where $\{\mathbf{r}\}$ and $\{\mathbf{p}\}$ represent the sets of positions and momenta of all the atoms, respectively. The $H_{\mathrm{CL}}^{\mathrm{system}}$ in Equation (6.2) is the classical Hamiltonian for the total system composed of the kinetic and the potential energy terms: $H_{\mathrm{CL}}^{\mathrm{system}} = E_{\mathrm{kin}}(\{\boldsymbol{p}\}) + E_{\mathrm{CL}}^{\mathrm{system}}(\{\boldsymbol{r}\})$. The set of last two terms on the right hand side of Equation (6.2) may be understood as a quantum correction to the classical potential energy for the QM region. We denote the sets of the positions of the CL and the QM atoms as $\{\mathbf{r}_{\mathrm{QM}}\}$ and $\{\mathbf{r}_{\mathrm{CL}}\}$, respectively.

We adopt the buffered-cluster method[19)] to couple the QM and CL regions in a seamless manner with respect to the atomic forces. In the buffered-cluster method, the two cluster-energy terms on the right hand side of Equation (6.2) are functions of the positions of the QM atoms $\{\mathbf{r}_{\mathrm{QM}}\}$ only:

$$E_{\mathrm{QM}}^{\mathrm{cluster}} = E_{\mathrm{QM}}^{\mathrm{cluster}}(\{\mathbf{r}_{\mathrm{QM}}\}), \qquad (6.3)$$

$$E_{\mathrm{CL}}^{\mathrm{cluster}} = E_{\mathrm{CL}}^{\mathrm{cluster}}(\{\mathbf{r}_{\mathrm{QM}}\}). \qquad (6.4)$$

In both QM and CL calculations of the QM region in Equation (6.3) and (6.4), fictitious atoms that are called the buffer atoms are placed at the broken dangling-bond sites of the QM atoms at the QM-CL boundaries to buffer possible effects due the bond cut.

For the CL calculation of the QM region in Equation (6.4), the buffer atoms are Si to mimic the original bonds at the QM-CL boundary. Starting from the positions of either the corresponding CL-Si atoms or the buffer-Si atoms at the last step, the positions of the buffer-Si atoms are adjusted at every time step in the simulation run to minimize the potential energy $E_{\mathrm{CL}}^{\mathrm{cluster}}$ under the constraint of fixing $\{\mathbf{r}_{\mathrm{QM}}\}$. Here, the buffer-Si atoms are set to interact only with the bonding-pair QM-Si through the SW inter-atomic potential. Note that the positions of the buffer atoms in the buffered-cluster method may differ from that of the corresponding CL atoms in the total system.

In the buffered-cluster method, the buffer atoms for the QM calculation of the QM region in Equation (6.3) are either H or Si depending on the bonding characteristics in the original Si system. For the present selection of the QM region depicted as case 3 in Figure 6.3, all the buffer atoms are H; for case 2, the buffer atoms are Si and H; for case 1, all the buffer atoms are H. The positions of the buffer-H atoms for the QM calculation are determined by referring to that of the buffer atoms in the atomic cluster for the CL

calculation. For each buffer-Si atom located at $\mathbf{r}_{CL}^{buffer}$ that connects to a QM atom at $\mathbf{r}_{QM}$ in the atomic cluster for the CL calculation, we put a buffer-H atom at $\mathbf{r}_b = \beta\mathbf{r}_{QM}^{buffer} + (1-\beta)\mathbf{r}_{QM}$ with the scaling factor $\beta = 0.66$ in the atomic cluster for the QM calculation.

Characteristic features of the buffered-cluster method are the following. Since both $E_{QM}^{cluster}$ and $E_{CL}^{cluster}$ in Equation (6.3) and (6.4) are independent of the positions of the CL atom $\{\mathbf{r}_{CL}\}$, the QM atoms interact with the CL atoms through the classical inter-atomic potential contained in H_{CL}^{system}. If we were to minimize the DFT energy, $E_{QM}^{cluster}$, of the atomic cluster through relaxation of the buffer atoms in the QM calculation, there should appear various surface-reconstructions of the cluster, resulting in undesirable deformations of the crystalline structure. Such a reconstruction on the cluster surface is suppressed in the buffered-cluster method. Accuracies of the buffered-cluster method when it is applied to Si crystal with various choices of the QM region have been analyzed from various points of view including the atomic positions, the atomic forces, and the electronic structures.[19] Merits of the buffered-cluster method as compared to the link-atom method[20] have been discussed. The buffered-cluster method has been applied also to ionic materials as alumina in which the empirical inter-atomic potential is long-ranged.[21]

As for the DFT calculation of the QM cluster, we adopt the standard Kohn–Sham (KS) formulation for the valence electrons with the norm-conserving pseudo-potentials.[22,23] Cartesian mesh-points in real space are used to represent the KS orbitals and the Hartree potential.[24] Those data on the mesh-points are spatially decomposed to store and to calculate them in compute nodes, which saves computer memory in a node and realizes fast computation on a parallel computer. The second derivatives of the KS orbitals and the Hartree potential are evaluated with the 6th-order finite-difference method.[24] The Fourier components of the local and nonlocal pseudo-potentials with wavelengths shorter than the mesh size are suppressed. The mesh size for Si is $h = 0.55$ a.u., which corresponds to the cut-off energy of $(\pi/h)^2 \sim 33$ Ry in the plane wave representation of the KS orbitals. Finer mesh-points are used for the KS orbitals in the vicinity of O following the double-grid method.[25]

There is an important point that should be considered for accurate coupling of the QM and the CL regions in the hybrid QM-CL simulation scheme. The classical SW potential predicts the Si-Si bond distance in Si crystal as 2.35 Å at zero pressure, which

is quite close to the experimental value. On the other hand, the present LDA-DFT calculation predicts the bond distance as 2.31 Å, which is about 1.5% smaller than the experimental value. The distance is 2.36Å if the generalized gradient approximation (GGA)[26] is adopted in the DFT. Though the LDA appears to give less accurate prediction of the bond distance as compared to the GGA, we choose to use the LDA because of the following three reasons: (i) the LDA is appropriate for a system with nearly homogeneous electron density and, in fact, the region around the inserted O in Si lattice may have nearly homogeneous electron density, (ii) the former DFT calculations[9–12] in literature to which we will compare used the LDA, and (iii) we are interested in the change of the activation energy due the system stretch rather than in its absolute value. Since we will stretch the system by the same order of 1% as the error of the LDA with respect to the bond distance, adjustment of the parameters in the SW potential to reproduce the same bond distance with that in the LDA-DFT calculation is necessary for accurate coupling of the QM and the CL regions. We therefore shorten all the radial parameters of the SW potential by 1.5% from their original values.

We analyze the accuracy of the QM-CL coupling for the present Si system containing O in two ways. In one way, we consider an intermediate configuration between the end and the mid states, and examine possible variation of the forces on the QM atoms by changing the size of the QM region (without changing the total system). For this purpose we pick an NEB-image ($\alpha = 3$; see Section 6.2.2) of the atoms close to the mid state at 9%-stretch in ⟨101⟩-case. We consider three QM sizes as shown in Figure 6.3 (top), and compare the forces on Si1, Si2, Si3, and O in Figure 6.3 (bottom). We then find that the forces approach to limiting values as we increase the QM size. Therefore we may state that the present choice (case 3) of the QM region for the hybrid simulation has high accuracies with respect to the forces with possible errors less than $0.01\ \mathrm{Ry}/a_\mathrm{B}$ (a_B is the Bohr radius) or a few percent. In the other way, we consider a two times larger total-system without changing the QM size. By such an increase, Si1, Si2, Si3, and O move by less than 0.001 Å through the atomic relaxation with the hybrid simulation method. We parenthetically consider a pure Si system by removing O in the hybrid QM-CL method. Though the QM atoms at the QM-CL boundary are found to deviate from the correct crystalline-positions slightly (by 0.03 Å at most), they do not affect other QM and CL atoms; in fact, the other atoms deviate by less than 0.003 Å, which is two orders of magnitude smaller than the possible value (order 0.1 Å) of the difference of d(Si1-Si3)

between the mid and the end states and therefore may be ignored.

6.2 Combining hybrid QM-CL and NEB methods

Direct computer simulation of the O transition in Si crystal is difficult at normal conditions since its activation energy is much larger than the thermal energy. Such a rare event problem is usually addressed with the transition state theory (TST)[27] based on the statistical mechanics. In the TST, the transition rate at temperature T is written as

$$k_{\text{TST}} = w\exp(- Q/k_{\text{B}}T) \qquad (6.5)$$

with the activation free-energy Q, the attempt frequency w, and the Boltzmann constant k_{B}. Theoretical calculation of Q is not easy since, in principle, one should span the configuration phase-space in its evaluation. In the harmonic approximation[27] to the TST,

$$Q \approx E_{\text{sad}} - E_{\text{end}} + k_B T \sum_{i=1}^{3N-1} \ln\left(w_i^{\text{sad}}/w_i^{\text{end}}\right) \qquad (6.6)$$

for a system of N atoms. Here E_{sad} is the energy at the saddle state, E_{end} is the local minimum of the potential energy corresponding to the end state, and $\{w_i\}$ are the corresponding normal-mode frequencies with the mode along the MEP excluded. The last term in the right hand side of Equation (6.6) corresponds to the entropy. At low temperatures, the energy difference $\epsilon \equiv E_{\text{sad}} - E_{\text{end}}$ called the activation energy dominates in Q.

The NEB method is a simulation technique to search the MEP between the two end states of a transition and to evaluate its activation energy, ϵ.[15] It has been widely used, for examples, for chemical reactions of molecules[28] in combination with electronic structure calculation such as the DFT, and for dislocation transition in metals[29] with the empirical inter-atomic potentials. Let us consider $M + 1$ images including two end images, in which each image is composed of N atoms at $\mathbf{R} \equiv \{\mathbf{r}_1, \mathbf{r}_2, \dots, \mathbf{r}_N\}$ in $3N$-dimention. An elastic band denoted as $[\mathbf{R}_0, \mathbf{R}_1, \mathbf{R}_2, \dots, \mathbf{R}_M]$ contains two end images fixed at $\mathbf{R}_0$ and $\mathbf{R}_M$ corresponding to the two local minima of the energy. The positions of the $M - 1$ intermediate images are adjusted with an optimization algorithm. In the formulation of the NEB method, the tangent at image-α $(\alpha \in \{1, 2, \dots, M - 1\})$ is estimated using two adjacent images along the path, $\mathbf{R}_{\alpha+1}$ and $\mathbf{R}_{\alpha-1}$. We use one of the simplest methods to estimate the tangential direction:

$$\hat{\mathbf{T}}_\alpha = \mathbf{T}_\alpha/|\mathbf{T}_\alpha| \text{ with } \mathbf{T}_\alpha = \frac{\mathbf{R}_{\alpha+1}-\mathbf{R}_\alpha}{|\mathbf{R}_{\alpha+1}-\mathbf{R}_\alpha|} + \frac{\mathbf{R}_\alpha-\mathbf{R}_{\alpha-1}}{|\mathbf{R}_\alpha-\mathbf{R}_{\alpha-1}|}. \qquad (6.7)$$

The total force acting on image-α is the addition of the spring force along the tangent and

the real force perpendicular to the tangent:

$$\mathbf{F}_\alpha = \mathbf{F}_\alpha^S|_\parallel + \mathbf{F}_\alpha^{real}|_\perp,$$

where

$$\mathbf{F}_\alpha^S|_\parallel = k_{\alpha,species}(\mathbf{R}_{\alpha+1} - \mathbf{R}_\alpha) \cdot \widehat{\mathbf{T}}_\alpha \widehat{\mathbf{T}}_\alpha$$
$$-k_{\alpha-1,species}(\mathbf{R}_\alpha - \mathbf{R}_{\alpha-1}) \cdot \widehat{\mathbf{T}}_\alpha \widehat{\mathbf{T}}_\alpha \qquad (6.9)$$

with the spring constant $k_{\alpha,species}$ that depends on both image pair and atomic species, and

$$\mathbf{F}_\alpha^{real}|_\perp = \mathbf{F}_\alpha^{real} - \mathbf{F}_\alpha^{real} \cdot \widehat{\mathbf{T}}_\alpha \widehat{\mathbf{T}}_\alpha. \qquad (6.10)$$

The spring forces, Equation (6.9), do not interfere with the convergence of the atomic positions within each image, while the real forces, Equation (6.10), do not affect the distribution of the images along the MEP. An improved way of estimating the local tangent in the NEB has been proposed in ref. 30.

In the present simulation to obtain the O transition path in Si crystal, we calculate the real force $\mathbf{F}_\alpha^{real}$ using the potential energy terms in the hybrid QM-CL simulation method. We introduce seven movable images (i.e., $M = 8$), which are placed initially along the straight line connecting the two end states. We relax all the atoms in the images $\alpha \in \{1, 2, \ldots, M-1\}$ concurrently to minimize the addition of the real potential energies and the spring energies. The velocity Verlet algorithm is used for the relaxation dynamics with the velocity-damping factor 0.5-0.99 at each time-step 1.0-5.0 fs depending on the relaxation stage. We intend to set the inter-image distances at around the center of the image sequence relatively shorter for accurate determination of the saddle state. We therefore set $k_{\alpha,species} \equiv \bar{k}_{\alpha,species}$ in Equation (6.9) with $\bar{k} \sim$ 100 a. u. , $\left(A_{0,O}, A_{1,O}, \ldots, A_{M-2,O}, A_{M-1,O}\right) = (1, 2, \ldots, 2, 1)$, and $A_{\alpha,Si} = (m_{Si}/m_O)A_{\alpha,O}$; m_O and m_{Si} are the atomic masses of O and Si, respectively. The mass dependence of the spring constant, $k_{\alpha,species}$, is effective to relax all the atoms coherently with the dynamic method.

In the present setting, the cost of the DFT calculation for the atomic cluster composed of 53 Si, 1 O, and 48 H for buffering is significantly higher than that of the MD potential calculation for the total system; the cost of the spring interaction calculation is negligible. Therefore the positions of the QM atoms are updated much less frequently than that of the MD atoms to minimize the total computation cost. Typical relaxation run takes about 20 h, in which the DFT calculation is performed for several hundred times

while the MD calculation of the total system for 10^5 times. We use 64 processors on an in-house PC cluster or Fujitsu HPC2500: 8 processors for each DFT calculation, 1 processor for each MD, and 1 processor for the spring interaction. If the MEP is symmetric with respect to the center, one may reduce the computation cost and the required memory size substantially by exploiting the symmetry. In the present study, however, we do not explore such a possibility for simplicity and generality of the simulation code.

6.3 Results and Analyses

Figure 6.4 shows the sequence of the real potential energies, $E_{\text{CL}}^{\text{system}}(\{\mathbf{r}\}) + E_{\text{QM}}^{\text{system}} - E_{\text{CL}}^{\text{cluster}}$, in the images obtained with the hybrid QM-CL-NEB method. In the figure, the horizontal axis denotes the linear location of the O, which is obtained by projecting its position measured from that in the central image to the Si1-Si3 line; the energies at the two ends, which are the same, are taken as the origin of the vertical axis. The open circles with dashed curve in Figure 6.4 correspond to the 0%-stretched (i.e., zero pressure) system. The mirror symmetry of the data points with respect to the central vertical line of Figure 6.4 indicates high numerical accuracies of the present simulation. We find that the activation energy at 0%-stretch is 1.93 eV, which relates to the highest point in the sequence of the open circles in Figure 6.4. We confirm that the central image in the sequence corresponds to the mid state in Figure 6.1(b) and that the mid state is the saddle point in the energy surface. Recall that the former LDA-DFT calculations[9–12] in literature using the supercells estimated the activation energy in the range 2.0-2.2 eV. The present value of 1.93 eV is obtained using the atomic clusters instead of the supercells, however, it is quite close to the former estimates.
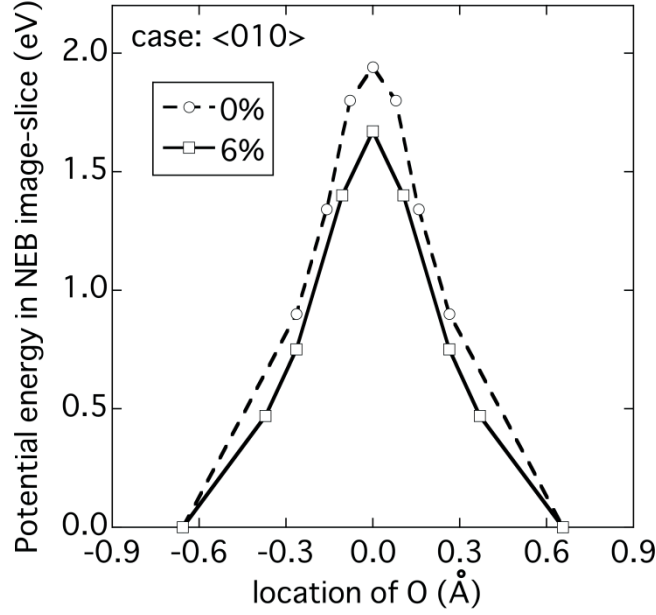
Figure 6.4. The sequence of the real potential energies in the NEB images for the O transition in Si, calculated with the hybrid QM-CL-NEB method. The open circles with dashed curve for 0%-stretch; the open squares with solid curve for 6%-stretch in ⟨010⟩-case.

To investigate the strain dependence of the activation energy, we consider three cases of stretch direction by changing the simulation box as has been done in the preparatory examination in Section 6.1: ⟨101⟩, ⟨010⟩, and ⟨10$\bar{1}$⟩. In each case, both negative and positive stretches are applied: 2, 3, 6, and 9%. Stretching the system should be followed by substantial relaxation of all the atoms in the total system. As an example, the energy sequence at 6%-stretch in ⟨010⟩-case obtained with the hybrid QM-CL-NEB method is depicted in Figure 6.4 as the open squares with solid curve. Through comparison of the two curves in Figure 6.4, we find a substantial decrease ~ 0.26 eV of the activation energy by the 6%-stretch in ⟨010⟩ direction. We have performed several trial runs with various inter-image distances (i.e., various $k_{\alpha,\text{species}}$) to confirm that the center of the image sequence that corresponds to Figure 6.1(b) is the saddle point in the energy surface in the stretched system.

Figure 6.5 summarizes all the calculated values of the activation energy for the

O transition in various conditions of stretched Si, obtained with the hybrid QM-CL-NEB method. We estimate possible error of each point in Figure 6.5 as 0.01-0.02 eV, from the fluctuation in the dynamic relaxation process in the hybrid QM-CL-NEB simulation. In all the three cases of the stretch direction, the activation energy varies monotonically as a function of the stretch. In ⟨101⟩-case, the activation energy decreases by 0.11 eV due to 2%-stretch and increases by 0.19 eV due to 9%-stretch. On the other hand, in ⟨010⟩-case, the activation energy increases by 0.02 eV due to 2%-stretch and deceases by 0.34 eV due to 9%-stretch. In ⟨10$\bar{1}$⟩-case weak dependence of the activation energy on the stretch is observed; the activation energy decreases only by 0.08 eV due to 9%-stretch. The weak dependence in ⟨10$\bar{1}$⟩-case is reasonable since the stretch direction in the case is perpendicular to the plane formed with Si1, Si2, and Si3 in Figure 6.1(a) or 6.1(b), on which the O moves. We will return to investigate physical mechanisms of the relatively strong stretch-dependencies of the activation energy observed in ⟨101⟩- and ⟨010⟩-cases.
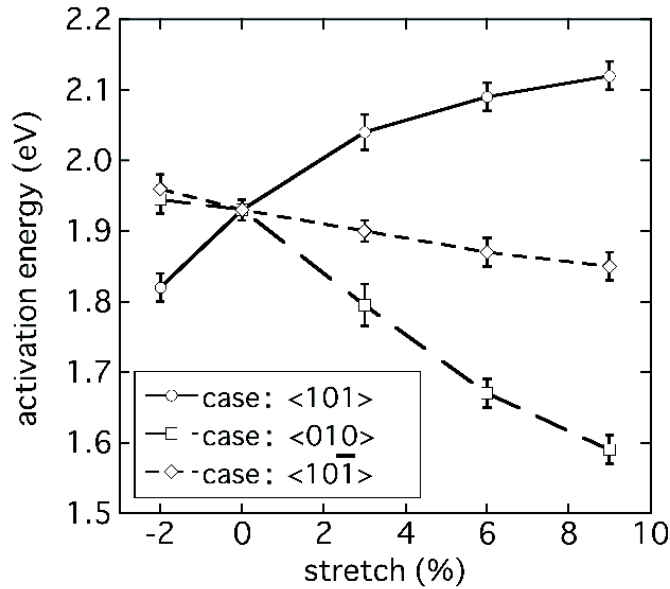

Figure 6.5. The activation energies for the O transition in stretched Si calculated with the hybrid QM-CL-NEB method.

As mentioned in Section 6.1, we are interested in the contribution of the peripheral atoms to the activation energy. The contribution of those atoms located outside of the sphere of radius r from Si2 to the activation energy, which is calculated with the hybrid QM-CL-NEB method, is shown in Figure 6.6 for $\langle 101 \rangle$-, $\langle 010 \rangle$-, and $\langle 10\bar{1} \rangle$-cases. It should be compared with Figure 6.2 obtained using the SW inter-atomic potential only. For each curve in Figure 6.6, we may take the value at $r \sim 10$ Å and regard it as the peripheral energy $\Delta E^*_{\mathrm{periph}}$ in the same way as in the preparatory examination in Section 6.1. Some of the curves in Figure 6.6 are not smooth, which indicates possible errors contained in the present simulation. We, in fact, observed $\Delta E_{\mathrm{periph}}$ at a given r fluctuate within 0.01 eV at the last stage of the relaxation run. We find that the magnitudes of $\Delta E^*_{\mathrm{periph}}$ at all the stretches are smaller than 0.04 eV in all the three direction-cases considered. In Section 6.1 we have demonstrated the possibility of substantial peripheral energy $\left| \Delta E^*_{\mathrm{periph}} \right| \sim 0.4$ eV at 9%-stretch in $\langle 101 \rangle$-case. However, the present results with the hybrid QM-CL-NEB method give quite small magnitudes of $\Delta E^*_{\mathrm{periph}}$ even at 9%-stretch in $\langle 101 \rangle$-case. This indicates that the major contribution to the activation energy comes from the DFT energy for the QM region. For all the three cases we in fact find that about 80 to 95% of the change of the activation energy due to the system stretch originates from the DFT cluster-energy, $E^{\mathrm{cluster}}_{\mathrm{QM}}$.
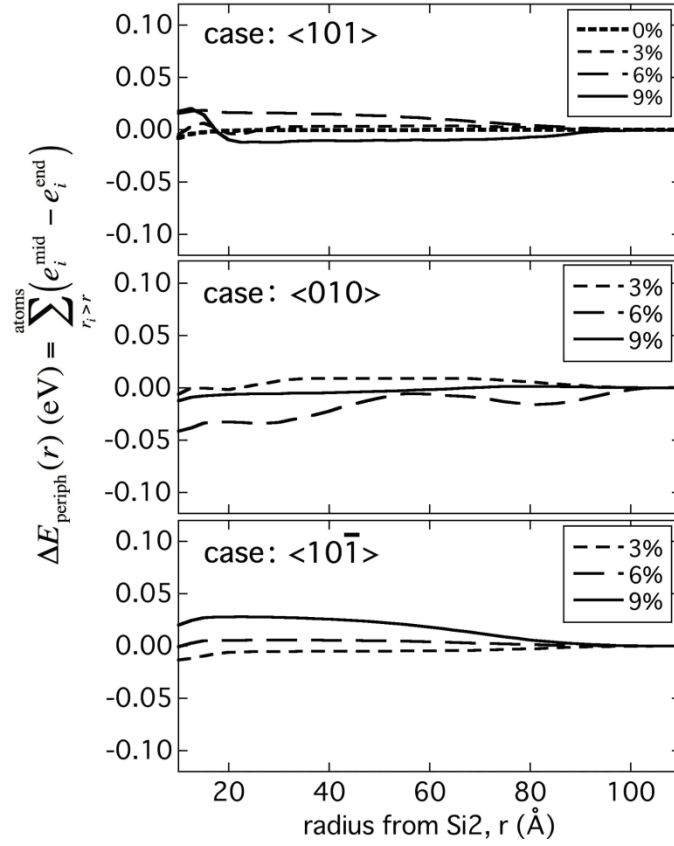
Figure 6.6. The $\Delta E_{\mathrm{periph}}(r)$ calculated with the hybrid QM-CL-NEB method.

We consider the reasons why the $\Delta E^*_{\mathrm{periph}}$ calculated with the hybrid QM-CL-NEB method is so small in magnitude in all the cases. In the preparatory examination, we have found that $\Delta E^*_{\mathrm{periph}}$ can be substantial at large stretches only in $\langle 101 \rangle$-case, and that the larger the difference $|\Delta d|$ of $d(\mathrm{Si1\text{-}Si3})$ between the end and the mid states the larger the $|\Delta E^*_{\mathrm{periph}}|$ in $\langle 101 \rangle$-case. We summarize the principal interatomic distances in the end state in Table 6.I; the distances in the mid state, in Table 6.II. For $\langle 101 \rangle$-case we find in Tables 6.I and 6.II: (i) at 0%-stretch, $d(\mathrm{Si1\text{-}Si3})$ in the mid state is substantially smaller by 0.17 Å than that in the end state, (ii) $d(\mathrm{Si1\text{-}Si3})$ in the mid (end) state increases by 4.4 (1.6), 6.0 (3.3), and 8.9 (5.2)% due to 3, 6, and 9%-stretches, respectively, (iii) at 9%-stretch, $d(\mathrm{Si1\text{-}Si3})$ in the mid state becomes quite similar to that in the end state. Therefore the small $|\Delta E^*_{\mathrm{periph}}|$ found at a relatively large stretch in $\langle 101 \rangle$-case corresponds well to the small $|\Delta d|$, in reference to the finding in the

preparatory examination. Since $d(\text{Si1-Si3})$ in the mid state increases linearly to the system stretch, we may think that neither Si1 nor Si3 exerts strong forces along the Si1-Si3 direction to the surrounding Si atoms due to the Si1-O and the O-Si3 interaction. This is also understood by the observation that the system stretch of the mid state in $\langle 101 \rangle$-case makes the Si1-O and the O-Si3 interaction weak, which will be demonstrated through the electron population analyses in the last paragraph of this section. The finding of negligible $\Delta E^*_{\text{periph}}$ in $\langle 101 \rangle$- and $\langle 10\bar{1} \rangle$-cases accords also well with that in the preparatory examination.

Table 6.I. Inter-atomic distances, d, in the end state (see figure 6.1) of the O transition in strained Si, obtained with the hybrid QM-CL-NEB method. The $d_{\text{Si}}^{\text{ref}}$ corresponds to d in the reference Si-crystal containing no O.

Stretch (%)	$d(\text{Si2-Si3})$ (Å)	$\dfrac{d(\text{Si2-Si3})}{d_{\text{Si}}^{\text{ref}}(\text{Si2-Si3})}$	$d(\text{Si1}-\text{Si2})$ (Å)	$d(\text{Si1}-\text{Si3})$ (Å)
0	3.264	1.409	2.322	4.459
$\langle 101 \rangle$ direction				
3	3.286	1.399	2.340	4.530
6	3.314	1.391	2.363	4.607
9	3.340	1.381	2.388	4.691
$\langle 010 \rangle$ direction				
3	3.284	1.404	2.346	4.461
6	3.303	1.398	2.370	4.460
9	3.321	1.392	2.396	4.461
$\langle 10\bar{1} \rangle$ direction				
3	3.270	1.403	2.333	4.463
6	3.274	1.397	2.344	4.460
9	3.278	1.391	2.353	4.457

Table 6.II. Inter-atomic distances, d, in the mid state (see figure 6.1) of the O transition in strained Si, obtained with the hybrid QM-CL-NEB method.

Stretch (%)	$(1/2)[d(\text{Si1-Si2}) + d(\text{Si2-Si3})]$ (Å)	$d(\text{O-Si2})$ (Å)	$d(\text{Si1-Si3})$ (Å)
0	2.875	1.765	4.288
$\langle 101 \rangle$ direction			
3	2.888	1.746	4.476
6	2.930	1.729	4.545
9	2.957	1.728	4.671
$\langle 010 \rangle$ direction			
3	2.960	1.770	4.211
6	2.990	1.763	4.297
9	3.024	1.772	4.323
$\langle 10\bar{1} \rangle$ direction			
3	2.880	1.763	4.348
6	2.903	1.760	4.350
9	2.930	1.761	4.337

In the following, we return to explain the physical mechanisms of the stretch dependence of the activation energy in Figure 6.5. As stated in the former paragraph, most of the change of the activation energy due to the stretch comes from the change of the DFT energy difference between the mid and the end states. Firstly we clarify that which state (mid or end) makes a major contribution to the activation energy-change. Figure 6.7 shows the changes of the DFT energy, $E_{\text{QM}}^{\text{cluster}}$, for each state at -2, 3, 6, and 9%-stretches; the top panel is for $\langle 101 \rangle$-case, the middle for $\langle 010 \rangle$-case, and the bottom for $\langle 10\bar{1} \rangle$-case. Additionally, as a reference, we plot in Figure 6.7 the changes of $E_{\text{QM}}^{\text{cluster}}$ for the QM region selected in pure Si crystal (i.e., no O atom is contained) in the same

way. In each panel, the mid-state energy (open circle) measured from the end-state energy (open square) at a given stretch (i.e., on a vertical line) corresponds to the activation energy-change. In $\langle 101 \rangle$-case, the end-state energy increases less than the Si-crystal energy does, due to positive stretches. In $\langle 010 \rangle$-case, on the contrary, the same behavior is observed for the mid-state energy. In $\langle 10\bar{1} \rangle$-case, both end-state and mid-state energies increase by the same amount as the Si-crystal energy does.
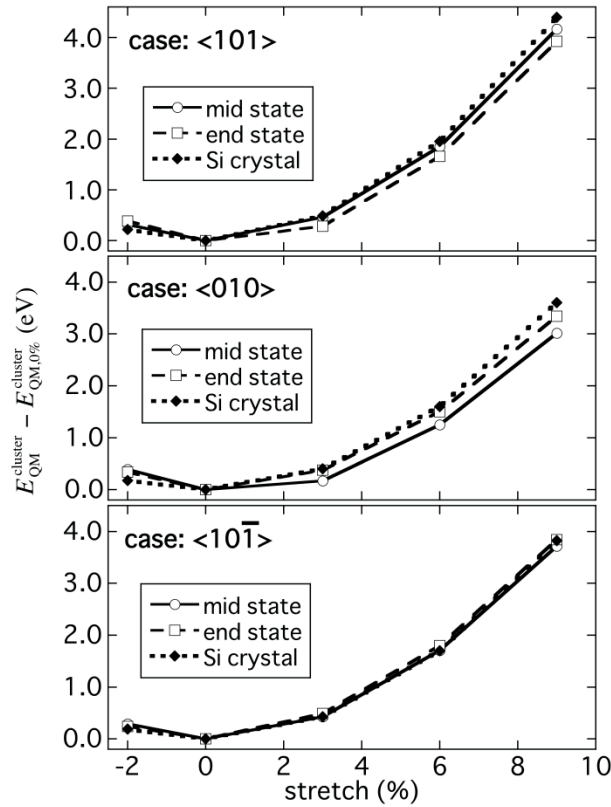
Figure 6.7. The changes of the DFT energies of the QM cluster due to the system stretches calculated with the hybrid QM-CL-NEB method. The open circles with solid curves for the mid state; the open squares with dashed curves for the end state. For references, those of the corresponding QM cluster for pure Si crystal are shown by the filled squares with dotted curves.

Secondly we proceed to investigate mechanisms of the relatively small energy-increases by $\langle 101 \rangle$- and $\langle 010 \rangle$-stretches in the end and mid states, respectively, observed in Figure 6.5 following the schema in Figure 6.8. Let us consider about the end state. Interesting behavior of the principal Si-Si distance is observed for the end state in Table 6.I; $d_{\mathrm{Si}}^{\mathrm{ref}}(\text{Si2-Si3})$ is the distance in the reference Si-crystal containing no O. We here note that the direction of the Si2-Si3 line in the end state does not differ significantly from that in the pure Si crystal. For the end state we observe in Table 6.I that: as the system is stretched, (i) $d(\text{Si2-Si3})$ increases more in $\langle 101 \rangle$-case than in the other two cases, and (ii) the ratio $d(\text{Si2-Si3}) / d_{\mathrm{Si}}^{\mathrm{ref}}(\text{Si2-Si3})$ becomes more closer to unity in $\langle 101 \rangle$-case than in the other two cases. As seen in the atomic configuration of the end state in Figure 6.3 (top), the Si2-Si3 segment experiences a compressive force from the surroundings at 0%-stretch. Therefore the (i) means enhanced structural relaxation occurring in $\langle 101 \rangle$-case. The (ii) supports the idea since a closer value of $d(\text{Si2-Si3}) / d_{\mathrm{Si}}^{\mathrm{ref}}(\text{Si2-Si3})$ to unity means a smaller force acting on the Si2-Si3 segment from the surroundings and vice versa. In $\langle 10\bar{1} \rangle$-case, such a structural relaxation is minimal and hence the energy change in the end state is nearly the same with that in the Si crystal as shown in Figure 6.7(c). We may therefore conclude that the enhanced structural relaxation in the end state at a positive stretch in $\langle 101 \rangle$-case has given the smaller energy-increase of the end-state as compare to the Si-crystal.
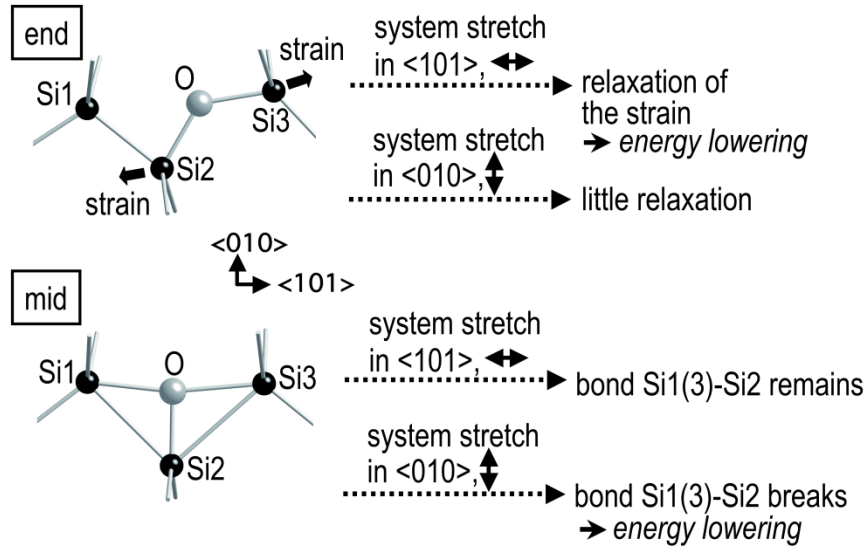
Figure 6.8. Proposed mechanisms of the energy lowering of the end and the mid states relative to the corresponding Si crystal, when the system is stretched in ⟨101⟩- and ⟨010⟩-directions.

Let us then consider about the mid state (see Figure 6.8). We find in Table 6.II that d(Si1-Si2), which is the same with d(Si2-Si3) by symmetry, extends slightly more in ⟨010⟩-case than in ⟨101⟩- and ⟨10$\bar{1}$⟩-cases. Table 6.III shows the Mulliken's overlap populations[31] p_{ol} of electrons between the principal pair of atoms in the mid state. Significant decrease of p_{ol}(Si1-Si2) and p_{ol}(Si2-Si3) to below 0.1 is observed only in ⟨010⟩-case, which means breakage of Si2-Si1(3) bond. In ⟨010⟩-case, since the stretch direction is parallel to the Si1-Si3 line, the larger at a positive stretch means weaker bonding between O and Si1(3); therefore, the original Si2-Si1(3) bond remains as seen in Table 6.III. In ⟨010⟩-case, on the contrary, the stretch direction is perpendicular to the Si1-Si3 line, and substantial bonding remains between O and Si1(3) even at large stretches. Relating to this, the Si2-Si1(3) bond breaks when the system is stretched in ⟨010⟩ direction, as seen in Table 6.III. We may therefore conclude that the breakage of Si2-Si1(3) bond acts to suppress the energy-increase of the mid-state due to ⟨010⟩-stretch. The sudden drop of the activation energy at 3%-stretch in h010i-case, seen in

Figure 6.5, should be related to such a breakage of Si2-Si1(3) bond occurring between 0 and 3%-stretches.

Table 6.III. The Mulliken's overlap populations, p_{ol}, in the mid state (see Figure 6.1) of the O transition in strained Si, obtained with the hybrid QM-CL-NEB method.

Stretch (%)	$(1/2)[p_{ol}(Si1\text{-}Si2)$ $+ p_{ol}(Si2\text{-}Si3)]$	$p_{ol}(O\text{-}Si2)$	$(1/2)[p_{ol}(O\text{-}Si)$ $+ p_{ol}(O\text{-}Si3)]$
0	0.171	0.712	0.141
$\langle 101 \rangle$ direction			
3	0.185	0.756	0.104
6	0.155	0.885	0.082
9	0.162	0.875	0.072
$\langle 010 \rangle$ direction			
3	0.098	0.870	0.145
6	0.098	0.868	0.132
9	0.097	0.847	0.128
$\langle 10\bar{1} \rangle$ direction			
3	0.178	0.718	0.131
6	0.177	0.752	0.125
9	0.160	0.777	0.122

6.4. Discussion and Concluding Remarks

We have calculated the change of the activation energy for the O transition in Si crystal with the hybrid QM-CL-NEB simulation method. With a nano-structured Si system at a complex interface in mind, we have stretched the Si system with one O atom ($N = 110{,}593$, in total) to three mutually perpendicular directions at a wide range of degree between -2 and 9%. It has been found that the change of the activation energy ranging from -0.4 to 0.2 eV depends sensitively on both direction and degree of the

stretch, and that the peripheral atoms in the system make little contribution to the activation energy-change. We have elucidated the microscopic mechanisms of the activation energy-change from the combined analyses of the atomic structure relaxation and the electronic populations. On the other hand, experimental data about the pressure dependence of the O diffusion rate in Si are available only at small degrees of compression, i.e., less than 1%. As far as we know, two groups have reported experimental results on the pressure dependence of the activation energy for O diffusion in Cz-Si. Antonova et al.[32] measured the partial dissolution of the O precipitates, which were created at $T = 900\text{-}1{,}000 \, \text{K}$, at high temperature $T = 1{,}230\text{-}1{,}550 \, \text{K}$ and pressure $P = 1.0\text{-}1.3 \text{GPa}$. In the experiment, the Acenters, which are the pairs of vacancy and O atom, were introduced into the O precipitates by electron irradiation, and the deep level transient spectroscopy was used to detect A-center agglomerates. They thereby estimated a significant drop of the activation free-energy to $Q \sim 0.62 \, \text{eV}$ at $P \sim 1.0 \, \text{GPa}$.[32] We here note that such a Cz-Si system annealed at high temperatures usually contains large-scale O precipitates accompanied by various kinds of defects around them, and that the O diffuses in the form of connected pairs of O and self-interstitials.[32] Since the O is assumed to diffuse in Si crystal in the form of the O interstitial (O_i) in the present simulation study, direct comparison of the present simulation results and the experimental data is difficult.

The other group made a series of experiments to measure the time rates of concentration enhancement of the TDD (i.e., small O aggregates) in Cz-Si at $T = 720 \, \text{K}$, to find that applying the pressure $P = 1.0 \, \text{GPa}$ increases the time rate by 3-10 depending on the initial concentration of O.[3,4] We may consider that the formation process of the TDD starts with the diffusion of O in the form of O_i. Meeting of two O_i may result in creation of the double O interstitial (O_{2i}), whose diffusion may be faster than that of O_i.[12] Assuming that the formation rate of the TDD is proportional to the diffusion rate of O_i we may estimate from the experimental data[3,4] that the activation free-energy for O_i diffusion changes by $\Delta Q = -0.08$ to $-0.16 \, \text{eV}$ at $T = 720 \text{K}$ due to the applied pressure $P = 1.0 \, \text{GPa}$. We will relate the present simulation results to this change as follows.

We convert the hydrostatic pressure to the strain. The bulk modulus of Si crystal described with the SW potential is $B = 1.08 \, \text{MBar}$,[33] which is close to the experimental value of 0.99 Mbar.[34] Therefore the hydrostatic pressure $P = 1.0 \, \text{GPa}$ corresponds to

the relative volume change of $\Delta V/V = -0.010$, which relates to shortening of each side length of the simulation box by 0.33%. Since such a length change is quite small and the three directions $(\langle 101 \rangle, \langle 010 \rangle, \langle 10\bar{1} \rangle)$ in the present simulation study are mutually perpendicular to each other, we may simply sum the activation energy-change, $\Delta \epsilon$, at 0.33%-stretch in $\langle 101 \rangle$, $\langle 010 \rangle$, and $\langle 10\bar{1} \rangle$-cases to evaluate the change $\Delta \epsilon$ for $P = 1.0$ GPa. Using the linear interpolation method to estimate $\Delta \epsilon$ at 0.33%-stretch in each case in Figure 6.5, we estimate $\Delta \epsilon = -0.014$ eV for $P = 1.0$ GPa from the present simulation results. Though the entropy is not included in $\Delta \epsilon$, we may expect similar tendencies of $\Delta \epsilon$ and of ΔQ. In fact, the present estimate of $\Delta \epsilon$ takes the same sign, but is several times as small in magnitude as the experimental value of ΔQ.

We parenthetically remark on a simple approach by Gusakov and Murin[35] to estimate the effect of pressure on the O diffusion in Si. They considered a Si cluster with O_i. The pressure was modeled by replacing the equilibrium distance of Si-Si bonds in the external part ($r > 5\text{-}7$ Å) of the cluster with the length of Si-Si bonds that corresponds to a given pressure. They thereby found lowering of the activation energy by 0.17% due to applied pressure $P = 1.0$ GPa, which corresponds to $\Delta \epsilon = -0.03$ eV in fair agreement with the present estimates $\Delta \epsilon = -0.014$ eV despite the simple modeling of the pressure. With their approach, however, it is difficult to analyze the dependence of the activation energy-change on the stretch direction and the possible contribution of the peripheral atoms to the energy.

Such a comparison analysis between the present results and the related experimental ones highlights inherent complexity of the experimental data, whose theoretical explanation is an open problem. It has been pointed out through the DFT calculation that there exists the saddle ridge in the energy surface around the MEP for the O transition at zero pressure.[9] Significant difference between the activation energy $\epsilon = 1.93$ eV calculated with the hybrid QM-CL-NEB method and the activation free-energy $Q = 2.53\text{-}2.56$ eV obtained experimentally at normal conditions,[36–40] may be explained by the entropy effects relating to the saddle ridge. Due to such a unique shape of the energy surface around the saddle ridge, the harmonic approximation to the free energy may not be accurate enough to estimate the activation free-energy. When Si crystal is strained, the shape of the saddle ridge is expected to change significantly. One of the possible reasons of the relatively large decrease of the activation free-energy $\Delta Q = -0.08$ to -0.16 eV due to $P = 1.0$ GPa estimated experimentally, might be related to

such a shape change of the energy surface around the MEP. Another possible reason is because of the existence of defects and dislocations in Cz-Si. Even if the hydrostatic pressure is applied to Cz-Si, un-isotropic and/or inhomogeneous stress field may be created in the system due to such imperfections. It means that the simple summation of the activation-energy changes at the same stretch in the three stretch-directions, which we did in the previous paragraph, may not be appropriate to a compressed Cz-Si. Considering that O diffuses preferably through the path with $\Delta \epsilon < 0$ in such a compressed system, we may expect $\Delta \epsilon$ for $\langle 101 \rangle$-case only contributes. Then we have another estimate of the activation-energy change $\Delta \epsilon = -0.053$ eV for $P = 1.0$ GPa relating to -0.33%-stretch in $\langle 101 \rangle$-case, which compares to the experimental estimates $\Delta Q = -0.08$ to 0.16 eV.

1) Semiconductors and Semimetals, ed. F. Shimura (Academic Press, Orlando, 1994) Vol. 42.

2) See, e.g., R. C. Newman: J. Phys.: Condens. Matter 12 (2000) R335.

3) 3) V. V. Emtsev, Jr., C. A. J. Ammerlaan, V. V. Emtsev, G. A. Oganesyan, B. A. Andreev, D. I. Kuritsyn, A. Misiuk, B. Surma, and C. A. Londos: Phys. Status Solidi B 235 (2003) 75.

4) V. V. Emtsev, B. A. Andreev, A. Misiuk, W. Jung, and K. Schmalz: Appl. Phys. Lett. 71 (1997) 264.

5) See, e.g., B. Lawn: Facture of Brittle Solids (Cambridge University Press, New York, 1993) 2nd ed.

6) J. M. Gibson and M. Y. Lanzerotti: Nature 340 (1989) 128.

7) F. M. Ross and J. M. Gibson: Phys. Rev. Lett. 68 (1992) 1782.

8) H. Kageshima and K. Shiraishi: Phys. Rev. Lett. 81 (1998) 5936.

9) M. Ramamoorthy and S. T. Pantelides: Phys. Rev. Lett. 76 (1996) 267.

10) S. Hao, L. Kantorovich, and G. Davies: Phys. Rev. B 69 (2004) 155204.

11) R. B. Capaz, L. V. C. Assali, L. C. Kimerling, K. Cho, and J. D. Joannopoulos: Phys. Rev. B 59 (1999) 4898.

12) J. Coutinho, R. Jones, P. R. Briddon, and S. O¨berg: Phys. Rev. B 62 (2000) 10824.

13) F. H. Stillinger and T. A. Weber: Phys. Rev. B 31 (1985) 5262.

14) See, e.g., G. Lu and E. Kaxiras: in Handbook of Theoretical and Computational Nanotechnology, ed. M. Rieth and W. Schommers (American Scientific Publisher, New York, 2005) Vol. X, Chap. 22.

15) G. Mills and H. Jo´nsson: Phys. Rev. Lett. 72 (1994) 1124.

16) S. Dapprich, I. Koma´romi, K. S. Byun, K. Morokuma, and M. J. Frisch: J. Mol. Struct.: THEOCHEM 461–462 (1999) 1.

17) S. Ogata, E. Lidorikis, F. Shimojo, A. Nakano, P. Vashishta, and R. K. Kalia: Comput. Phys. Commun. 138 (2001) 143.

18) S. Ogata, F. Shimojo, R. K. Kalia, A. Nakano, and P. Vashishta: Comput. Phys. Commun. 149 (2002) 30.

19) S. Ogata: Phys. Rev. B 72 (2005) 045348.

20) M. Eichinger, P. Tavan, J. Hutter, and M. Parinello: J. Chem. Phys. 110 (1999) 10452.

21) S. Ogata and R. Belkada: Comput. Mater. Sci. 30 (2004) 189.

22) See, e.g., M. C. Payne, M. P. Teter, D. C. Allan, T. A. Arias, and J. D. Joannopoulos: Rev. Mod. Phys. 64 (1992) 1045.

23) N. Troullier and J. L. Martins: Phys. Rev. B 43 (1991) 1993.

24) J. R. Chelikowsky, N. Troullier, and Y. Saad: Phys. Rev. Lett. 72 (1994) 1240.

25) T. Ono and K. Hirose: Phys. Rev. Lett. 82 (1999) 5016.

26) J. P. Perdew, K. Burke, and M. Ernzerhof: Phys. Rev. Lett. 77 (1996) 3865.

27) P. Ha¨nggi, P. Talkner, and M. Borkovec: Rev. Mod. Phys. 62 (1990) 251.

28) G. Henkelman, B. P. Uberuaga, and H. Jo´nsson: J. Chem. Phys. 113 (2000) 9901.

29) T. Rasmussen, K. W. Jacobsen, T. Leffers, O. B. Pedersen, S. G. Srinivasan, and H. Jo´nsson: Phys. Rev. Lett. 79 (1997) 3676.

30) G. Henkelman and H. Jo´nsson: J. Chem. Phys. 113 (2000) 9978.

31) D. Sa´nchez-Portal, E. Artacho, and J. M. Soler: J. Phys.: Condens. Matter 8 (1996) 3859.

32) I. V. Antonova, A. Misiuk, V. P. Popov, L. I. Fedina, and S. S. Shaimeev: Physica B 225 (1996) 251.

33) H. Balamane, T. Halicioglu, and W. A. Tiller: Phys. Rev. B 46 (1992) 2250.

34) G. Simmons and H. Wang: Single Crystal Elastic Constants and Calculated Aggregate Parameters: A Handbook (MIT Press, Cambridge, MA, 1971).

35) V. Gusakov and L. Murin: Physica B 340–342 (2003) 773.

36) C. Haas: J. Phys. Chem. Solids 15 (1960) 108.

37) P. D. Southgate: Proc. Phys. Soc. 76 (1960) 385.

38) G. D. Watkins, J. W. Corbett, and R. S. McDonald: J. Appl. Phys. 53 (1982) 7097.

39) J. C. Mikkelsen, Jr.: Appl. Phys. Lett. 40 (1982) 336.

40) S.-T. Lee and D. Nichols: Appl. Phys. Lett. 47 (1985) 1001.

7 Enhanced Si-O Bond Breaking in Silica Glass by Water Dimer: A Hybrid Quantum-Classical Simulation Study

7.1 Introduction

Silica (*i.e.*, SiO_2) is known to form both glass and crystals, such as α-quartz under ordinary conditions and β-quartz and cristobalite at higher temperatures, depending on the manufacturing procedure and environmental conditions. High-purity silica glass has superior durability and mechanical strength to other glasses such as soda glass.[1,2] Silica glass therefore has been or is expected to be used for mission-critical applications such as for optical fibers,[3] nearly permanent data-storage devices,[4] and matrices for nuclear waste storage.[5] While the migration of water to α-quartz in a moist environment is negligible, it is substantial to silica glass.[6] Even in silica glass with relatively high water resistance, a substantial number of Si-OH groups are produced not only through manufacturing processes but also through Si-O bond-breaking reactions involving the migrated water.[1] A further increase in the number of Si-OH groups is undesirable for applications since it affects both the coefficient of thermal expansion and the refractive index and thereby increases the loss of long-wavelength optical transmission in optical fibers.[3] It also degrades the durability of silica glass in data-storage devices.[4] A theoretical understanding of both the conditions and the microscopic mechanisms of Si-O bond breaking by water is therefore essential.

Tomozawa's group[7] thoroughly investigated the reactions of silica glass with water molecules by infrared spectroscopic measurements to find the following key features; (i) Water molecules migrate from a moist environment and diffuse in the molecular form. (ii) Reactions between water molecules and Si-O bonds appear to involve a multiple-stage process and proceed slowly with a characteristic timescale on the order of 10 days, resulting in the formation of Si-OH groups. (iii) Hydrogen bonding occurs between a water molecule and a Si-OH group. We consider that the features suggest: two water molecules diffusing separately in silica glass may meet each other to form a water dimer under some conditions, and then the dimer breaks a Si-O bond.

Regarding the microscopic theory of reactions between water and silica glass, the Michalske-Freiman (MF) model,[8] which involves a water molecule, has been thought to govern the crack-tip reaction[9] in stretched silica glass given by $\equiv$ Si-O-Si$\equiv$ +

$H_2O \rightarrow \equiv$Si-OH HO-Si$\equiv$.　At the crack tip of silica glass in mode-I opening, an intrusive water molecule adsorbs at an elongated Si-O bond and breaks the bond to form two neighboring Si-OH groups. The MF model is also expected to account for the principal process in the stress corrosion cracking of Si in a moist environment.

　　　　Del Bene et $al.$[10] presented a seminal theoretical study on the possible reaction between silica glass and multiple water molecules in dimer and trimer forms in addition to the monomer. To simplify the Si-O network structure of silica glass, they considered a small molecule FH_2Si-O-$SiFH_2$ with F and H for termination. The energetics of the reactions of the molecule with a water monomer, dimer, and trimer were investigated by the molecular orbital calculations with second-order perturbation theory for the electron correlation. The calculated energies should be regarded as qualitative values because of the ignorance of the glass structures and the existence of F and H adjacent to Si in the molecule. It was found that the binding energies of the water monomer, dimer, and trimer are in the order monomer < trimer < dimer; that is, the adsorption of a water dimer is the most probable. Also, the barrier energy of Si-O bond breaking by the dimer through the intermediate state of $OH^- + H_3O^+$ is 1.3 eV. It was pointed out the possibility that Si-O bond breaking by a water dimer precedes that by a water monomer, which is in accordance with the above suggestion relating to the experimental data in Ref. 7.

　　　　Bakos et $al.$[11,12] considered a 72-atom silica glass under the periodic boundary conditions and placed a water dimer at the center of a $(Si$-O-$)_8$ ring. Using the density-functional theory (DFT) with the generalized gradient approximation (GGA),[13] they found that the barrier energy is 1.5 eV for the dissociative adsorption of the water dimer at the dual adsorbed state of Si-$OH^- + O$-H_3O^+ through the reaction $2H_2O \rightarrow OH^- + H_3O^+$ without breaking a Si-O bond. The two adsorption sites were located on the same $(Si$-O-$)_8$ ring. Batyrev et $al.$[14] calculated the barrier energies for both the diffusion and adsorption of a water molecule in another 72-atom silica glass. As we will explain below, however, such a small silica glass is suspected to contain artificial local strains and therefore substantial ambiguity in the barrier energies.

　　　　In this study we will therefore prepare a large-scale silica glass composed of 4,608 atoms and will perform the hybrid quantum (QM)-classical (CL) simulation[15-17] of internal Si-O bond breaking by either a water monomer or dimer. The hybrid QM-CL

simulation has a physical accuracy comparable to that of the first-principles molecular dynamics (MD) simulation. We will thereby demonstrate that when the silica glass containing a water dimer in a void is gradually compressed at a temperature of 400 K, the bond-breaking reaction is enhanced significantly if microscopic conditions are satisfied. The reasons for the conditions will be explained. On the other hand, when the silica glass contains a water monomer in the same settings, we will demonstrate that no bond breaking with the water occurs until the system collapses as a result of compression. Through separate calculations we will show that the barrier energy for Si-O bond breaking with a water dimer is substantially smaller than that with a water monomer. We will also show that the barrier energy in the case of a water dimer decreases significantly when the system is compressed.

For the existence of a water dimer in silica glass, water molecules are required to migrate to the interior from a moist environment and to meet and form a dimer. In this paper we will show that connected paths between voids exist in the present 4,608-atom silica glass, through which water monomers can diffuse thermally. The connected paths between the voids will be related to the existence of large $(Si-O-)_n$ rings in the silica glass.

The organization of this paper is as follows. Section 7.2 will explain the methodology used to prepare a large-scale silica glass and to perform the hybrid QM-CL simulation of it. Microscopic structures of the silica glass and their changes upon compression and expansion will be analyzed. In Section 7.3, the hybrid QM-CL simulation of the silica glass under gradual compression or expansion with a water monomer in a void will be performed at 400 K. No Si-O bond-breaking reactions will be observed. In Section 7.4, the hybrid QM-CL simulation of 24 cases with a water dimer in a void will be performed, and Si-O bond breaking will be found in 3 cases. Separate DFT calculations of the barrier energy and heat of reaction will be also performed. Section 7.5 will demonstrate the existence of connected paths between voids in the silica glass, through which a water monomer can diffuse. A summary and concluding remarks will be also given.

7.2 Methodology and Preparatory Simulation

We prepare a large-scale silica glass under the periodic boundary conditions to minimize artificial internal strains. There are several interatomic potentials to describe

silica glass.[18-21)] We adopt a recent one proposed by Takada *et al.*[21)] for gradually quenching a silica liquid in an MD simulation.[22)] For simplicity, we ignore the density-dependent factors installed in the interatomic potential formula $V_{ij}(r_{ij})$ by setting them to unity as follows:

$$V_{ij}(r_{ij}) = \frac{Q_i Q_j}{r_{ij}} + f_{ij}(r_{ij}) \qquad (7.1)$$

with

$$f_{ij}(r_{ij}) = A_{ij}\{1 - \exp[B_{ij}(r_{ij} - C_{ij})]\}^2 - A_{ij} . \qquad (7.2)$$

Here, the charges in Equation (7.1) are $Q_{Si} = 1.30\,e$ and $Q_O = -0.65\,e$, and the parameters in Equation (7.2) are $A_{SiO} = 1.99597$ eV, $A_{OO} = 0.023272$ eV, $A_{SiSi} = 0.007695$ eV, $B_{SiO} = 2.6518$ Å^{-1}, $B_{OO} = 1.3331$ Å^{-1}, $B_{SiSi} = 2.0446$ Å^{-1}, $C_{SiO} = 1.628$ Å, $C_{OO} = 3.791$ Å, and $C_{SiSi} = 3.7598$ Å. The Ewald method[22)] is used for the Coulomb calculation.

We begin by melting a 576-atom α-quartz at 5,000 K with volume expansion. Following the time-evolution schedule of the temperature and density used to prepare a silica glass in Ref. 17, we perform a long (about 5 ns in total) quenching run of the system by 100 K in a stepwise manner with a volume shrinkage. We then double the dimensions in all three (x, y, and z) directions to obtain a system of eight times as large as the original. An additional relaxation run is performed at 400 K.

The thereby obtained silica glass, which is composed of 4,608 atoms (1,536 Si and 3,072 O), has dimensions of $(L_x, L_y, L_z) = (41.782, 36.193, 46.424)$ Å and a density of 2.18 g/cm^3. In general, each Si (O) atom has four (two) nearest-neighbor O (Si) in silica. Since a single bonding defect of Si (that has three nearest-neighbor O) remains in the original 576-atom system, eight defects exist in the present silica glass. We will insert water molecules at locations far from the defects to avoid undesirable effects due to the defects.

We refer to a local vacant space among the three-dimensional Si-O network as a void for simplicity. The void may be characterized by $(Si\text{-}O\text{-})_n$ rings on its surface. We count the numbers of $(Si\text{-}O\text{-})_n$ rings with $n \leq 9$. Figure 7.1(a) depicts a void in α-quartz, which has $(Si\text{-}O\text{-})_6$ and $(Si\text{-}O\text{-})_8$ rings on its surface; representative rings are highlighted by dots. As can be seen in Figure 7.1(a), a $(Si\text{-}O\text{-})_8$ ring can be regarded as

an aggregate of four $(Si-O-)_6$ rings. However, for clarification, we count $(Si-O-)_6$ and $(Si-O-)_8$ rings independently. In α-quartz the population ratio of $(Si-O-)_6$ to $(Si-O-)_8$ rings is 1 to 7. On the other hand, the sizes (n) of the rings are distributed widely from 3 to 9 in the present silica glass, as depicted in Figure 7.1(b). The relative populations are respectively 0.75, 5.73, 15.86, 24.37, 28.63, 22.74, and 1.92 % for $n = 3, 4, 5, 6,$ 7, 8, and 9. We remark that a water molecule can pass through the rings with $n \geq 7$ as the barrier energies for the passage are on the order of 0.1 eV.[11]
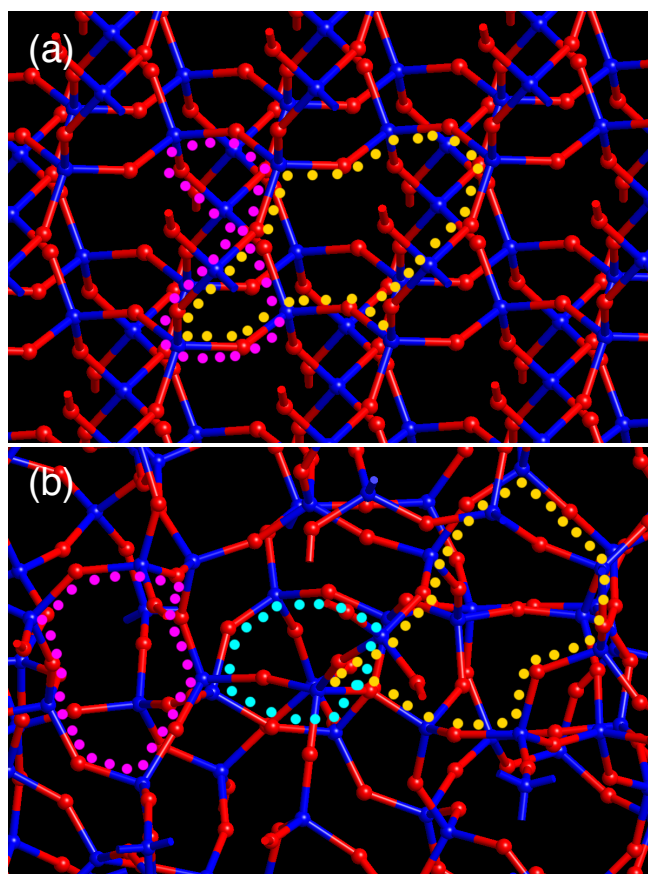
Figure 7.1. (a) Representative $(Si-O-)_6$ and $(Si-O-)_8$ rings, highlighted by magenta and yellow dots, respectively, in α-quartz. The red and blue spheres are O and Si, respectively. (b) Same as (a), but $(Si-O-)_4$, $(Si-O-)_6$, and $(Si-O-)_8$ rings are highlighted by cyan, magenta, and yellow dots, respectively, in the present silica glass.

In both α-quartz and the present silica glass, the Si-O bond lengths are 1.61−1.69 Å. Figure 7.2 shows the distributions of the three-body angles in 5 %-compressed (in the x-direction), 0 %-compressed (*i.e.*, the present), and 5 %-expanded systems (a) for O-Si-O and (b) for Si-O-Si. Through comparison of the distributions, we find that the Si-O-Si angle at an O shared by two SiO_4 units easily changes. While the deformation of a SiO_4 unit by expansion is negligible, it is substantial by compression, as seen in Figure 7.2(a). We will find in Section 7.4 that the deformation of a SiO_4 unit is a key requirement for Si-O bond breaking to occur and that the deformation degree of a SiO_4 unit due to system compression strongly depends on its local structure. If one prepares a silica glass either at a much higher quenching rate or using a much smaller system such as 72 atoms, the distributions of both the ring sizes and three-body angles are altered substantially. In such silica glasses, the adsorption energies of a water molecule become unphysically large.
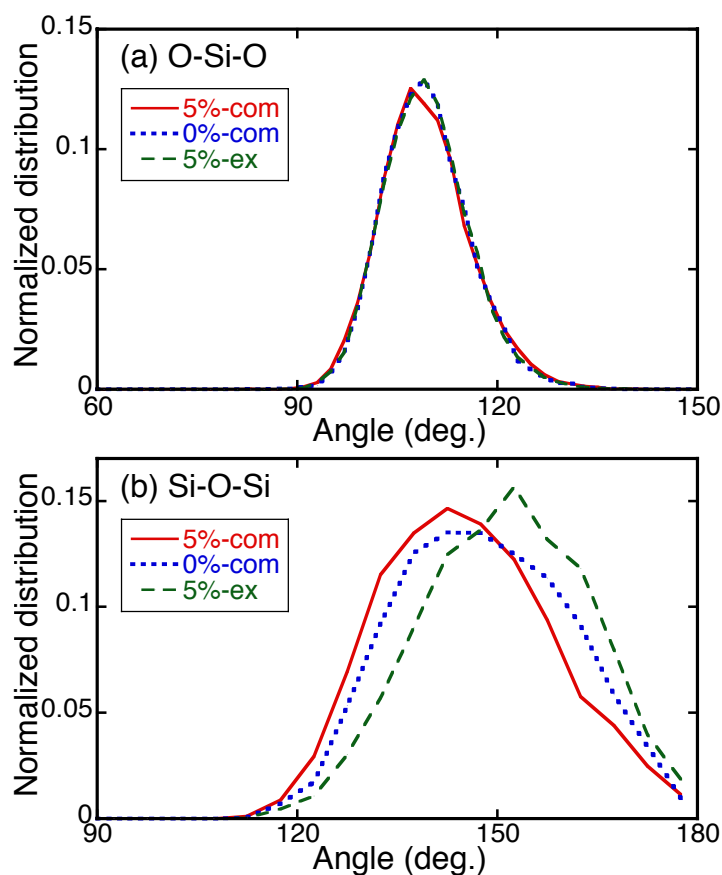
Figure 7.2. (a) Distributions of O-Si-O angles in the present silica glass at 5 % compression, 0 % compression, and 5 % expansion. (b) Same as (a), but for the Si-O-Si angles.

In Section 7.3 and 7.4, we will insert either a water monomer or dimer in a void in the present silica glass and will perform simulations with gradual compression or expansion to study the reaction dynamics between the water and Si-O bonds. For the simulations we adopt the hybrid QM-CL method, which is applicable to various large condensed systems including Al, alumina, Si, SiO_2, and graphite,[17,23-25)] while maintaining a high accuracy of DFT.[26)] As depicted in Figure 7.3(a) for a water molecule in a void, the total system is virtually decomposed to QM and CL regions. The atoms in the QM region are described with DFT, while those in the CL region are described with the classical interatomic potential proposed by Takada *et al.*[21)] The QM region contains a water molecule near its center. The outermost atoms of the QM region are Si; H atoms

are added as the buffer atoms to terminate the Si of virtually broken Si-O bonds. The positions of the buffer atoms are controlled dynamically using the buffered cluster method.[17]
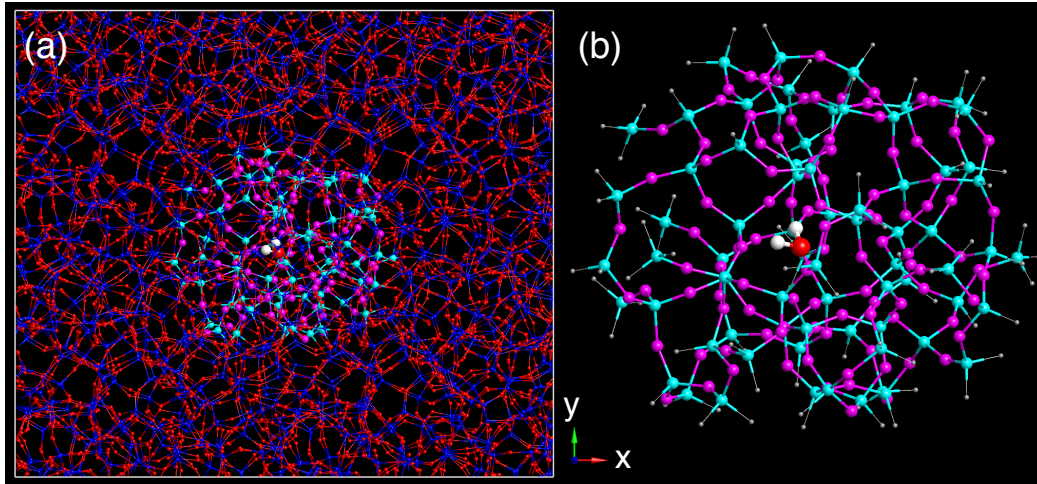

Figure 7.3. (a) Present silica glass with a water molecule in a void. The red and blue spheres are CL O and Si, respectively. The magenta and cyan spheres are QM O and Si, respectively. The large red and white spheres are respectively QM O and H of a water molecule. (b) Atomic cluster used for the QM calculation.

The electronic structure calculation of the QM region with the buffer atoms is performed using the real-space grid (RG) DFT code[27] which is efficient in large-scale simulations[28] on supercomputers. In the RGDFT, the norm-conserving pseudopotentials[29] are used for valence electrons. The local density approximation (LDA) is used for the exchange-correlation potential for the following reasons. While the GGA describes the water dimer structure and energy better than the LDA (the energy difference is about 0.1 eV),[30] the LDA reproduces various properties of individual silica phases better than the GGA.[31] Since we will compress or expand the silica glass without changing the phase, the LDA is suitable for our study. In the RGDFT, higher numerical accuracy is obtained with a smaller gridsize h at the cost of longer computation times.

We set $h = 0.40\, a_{\mathrm{B}}$ $(a_{\mathrm{B}} = 0.5292\ \text{Å})$ from the following observations. As we decrease h, the equilibrium Si-O-Si angle of α-quartz increases and the Si-O bond length decreases. At $h = 0.40$ $(0.35)\, a_{\mathrm{B}}$, the Si-O-Si angle is 137° (141°) and the Si-O bond length is 1.66 (1.63) Å, while the angle is 144° and the Si-O bond length is 1.61 Å in experiments. Despite differences of only a few percent in the angle and bond length, the computation time with $h = 0.35\, a_{\mathrm{B}}$ is about five times that with $h = 0.40\, a_{\mathrm{B}}$.

7.3 Hybrid Simulation with Water Monomer in Void

In this section, we consider a water molecule inserted in a void of the present silica glass. After the insertion, we select the QM region composed of water and its surrounding Si and O atoms in the hybrid QM-CL method, as shown in Figure 7.3(a). The radius of the QM region is about 17 Å and the region is composed of about 200 atoms. Figure 7.3(b) shows the atomic cluster including the termination H atoms used in the QM calculation. The RGDFT code calculates the electronic structures of this atomic cluster of about 260 atoms. The hybrid QM-CL simulation is performed for 1.0 ps with a time step of 1.0 fs at a temperature of 400 K using the Berendsen method[32] until equilibration. That is, at each time step, the velocity vectors of all the atoms are scaled by $\sqrt{1 + \left(\frac{T_{\mathrm{req}} - T}{T}\right) / n_{\mathrm{B}}}$ with the required temperature T_{req} and the number of relaxation time steps $n_{\mathrm{B}} = 100$.

We then compress or expand the system gradually in either of the $\{x, y, z\}$-directions. For the compression procedure, we adopt the constant-volume-change method: the volume becomes 95 % of the initial value after 1,000 time steps. The present volume-change rate is chosen from the following facts. In a former classical MD simulation[33] of the yield stress of a silica glass under expansion, a 2 %-higher (lower) value was obtained at a rate twice as high (low) as the present one. Also we perform a classical MD simulation to analyze possible compression-rate dependence of the Si-O-Si angle. By comparison with a simulation run at a rate five times as slow as the present one, we find no substantial difference in the angle until 10 % compression. We are interested in the reaction dynamics due to the inserted water. Since no Si-O bond switching is found until 20 % compression in the present silica glass without water in the classical MD

simulation, we perform the hybrid QM-CL simulation run for 4.0 ps (corresponding to 20 % compression).

Several voids, in each of which a water molecule is inserted, are selected randomly in the present silica glass. For a void, we compress or expand the total system in either of the $\{x, y, z\}$-directions. In all the compression and expansion runs, the water molecule moves inside the void and does not initiate the Si-O bond breaking. This indicates that the adsorption energy of a water molecule at a void surface is on the order of 0.1 eV at most and that the barrier energy for Si-O bond breaking by a water molecule is substantially larger than 0.1 eV order irrespective of the compression stage. In former DFT calculations[14,30] of a 72-atom silica glass, it was found that the O of a water molecule formed a covalent-like bond with a Si of the Si-O network; the bonding energy was 0.5 eV in Ref. 14. However, we did not find such a robust bond in the present runs. We assume that such a bond resulted from artificial residual stresses due to the smallness of the system under the periodic boundary conditions.

To understand the reasons for no Si-O bond breaking by a water molecule in the present runs, we separately calculate the corresponding barrier energy by DFT. Using a typical void (case 1y in Section 7.4), we calculate the energy of the relaxed system as a function of the constrained distance between the center of the target Si-O bond and the O of H_2O to find the reaction path. For fast calculation, we relax about 130 atoms around the H_2O and fix other atoms. We analyze the dependence of the energy on the compression in the y-direction. At 0 % compression, we find that the state $\equiv$Si-OH HO-Si$\equiv$ is unstable (*i.e.*, no transition state exists) and transforms barrierlessly to $\equiv$Si-O-Si$\equiv$ + H_2O. This is because a SiO_4 unit hardly deforms from a regular tetrahedron at 0 % compression and hence approach of the O in H_2O to the Si requires large deformation energy of the SiO_4 unit (3.1 eV at a constrained distance of 1.6 Å). At 5 % and 10 % compression, we find that the state $\equiv$Si-OH HO-Si$\equiv$ is metastable and that the barrier energies are respectively 0.52 and 0.92 eV. The substantial deformation of SiO_4 units by compression makes the reacted state metastable. Figure 7.4 shows the configurations at the initial and near-transition states at 10 % compression. If the system is expanded, we assume that the situation does not change substantially from that at 0 % compression because the significant amounts of stains are absorbed by the angular (Si-O-Si) relaxation between SiO_4 units [see Figure 7.2(a)].
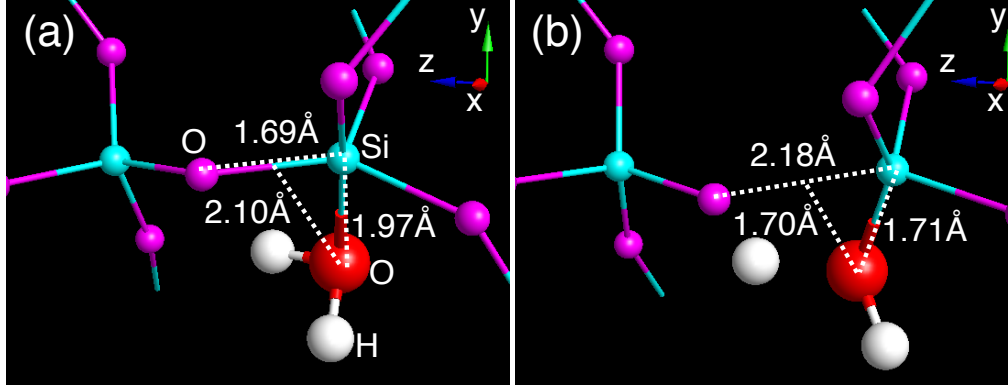
Figure 7.4. Zoom-in views of the atomic configuration in the Si-O bond-breaking reaction with a water monomer by DFT in case 1y at 10 % compression (a) for the initial state and (b) for the transition state.

The heat of reaction in Si-O bond breaking by a water molecule is endothermic: it is -0.82 and -0.40 eV at 5 % and 10 % compression, respectively. Considering the endothermic nature of the reactions, we expect that they have little opportunity to occur even at high temperatures. Note that the former calculations[11,12] for the 72-atom silica glass gave a barrier energy of 1.5 eV and a heat of reaction of $-0.3 - -0.7$ eV at 0 % compression, and the heat of reaction was about 0 eV at 0 % compression in Ref. 13. Despite the significant difference in the system size, the endothermic nature of the reaction was predicted.

7.4 Hybrid Simulation with Water Dimer in Void

In this section, we consider a water dimer placed in a void of the silica glass. To prepare the initial configuration, we first insert a water dimer at the center of a void selected randomly in the present silica glass. Since this causes a significant change in the potential energy owing to the relatively large size of the dimer, we then thermalize only the six atoms that compose the water dimer at 400 K. We then thermalize all the atoms of

the system at 400 K. If either a dimer or a molecule diffuses into a neighboring void, we choose another void. Starting from the initial configuration obtained thereby, we compress the system gradually in one direction for 4.0 ps at the same rate as in the water monomer runs (*i.e.*, 5 % compression after 1.0 ps).

For the locations of voids, we choose eight sites randomly. The centers of the voids are at $(x/L_x, y/L_y, z/L_z) = (0.500, 0.500, 0.500)$ for void 1, $(0.434, 0.027, 0.120)$ for void 2, $(0.558, 0.596, 0.241)$ for void 3, $(0.456, 0.215, 0.594)$ for void 4, $(0.921, 0.639, 0.758)$ for void 5, $(0.455, 0.024, 0.135)$ for void 6, $(0.424, 0.061, 0.886)$ for void 7, and $(0.545, 0.067, 0.772)$ for void 8. We compress the system in the x, y, and z-directions and hence have 24 cases in total. We name each case; for example, case 2y denotes the case that void 2 is chosen and compressed in the *y*-direction. The surface of a void is characterized by the distribution of $(Si\text{-}O\text{-})_n$ rings. We define n_i as the number of the rings with $n = i$ on the void surface. Table I shows the distribution of $\{n_i\}$ for each of the eight voids. Figure 7.5 depicts the QM region with a water dimer in it for each void. As can be seen in Table 7.I and Figure 7.5, both small $(n = 3, 4)$ and large $(n = 9)$ $(Si\text{-}O\text{-})_n$ rings exist on the void surfaces.
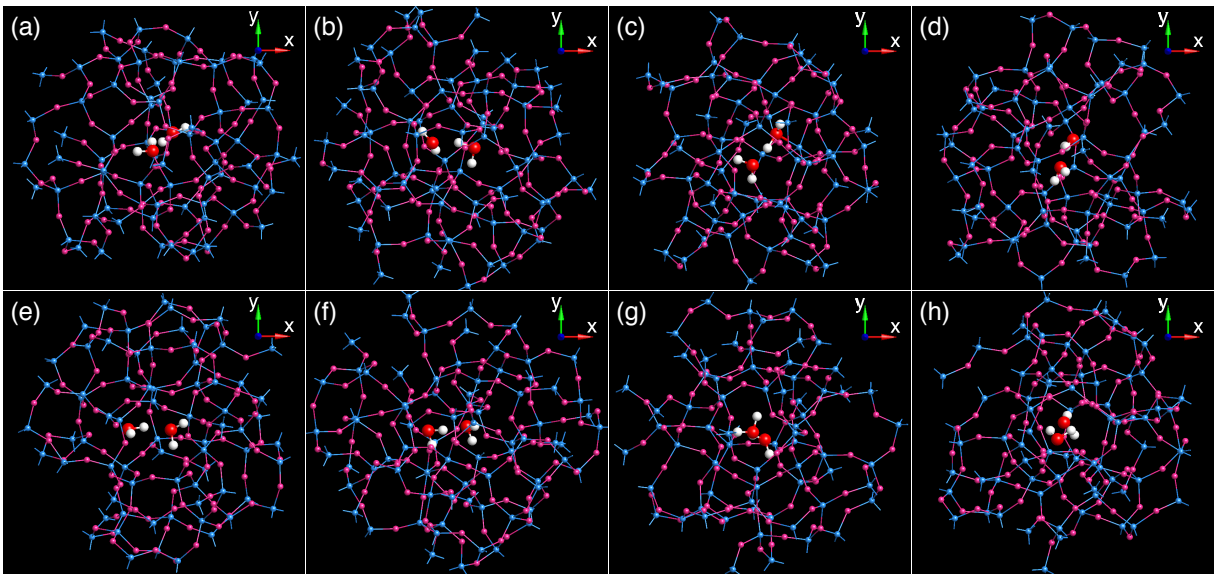

Figure 7.5. QM atoms in each of the eight voids with a water dimer (a) for void 1, (b) for

void 2, (c) for void 3, (d) for void 4, (e) for void 5, (f) for void 6, (g) for void 7, and (h) for void 8. The Si-O bonds within a distance of 2.0 Å and the O-H bonds within a distance of 1.2 Å are shown.

Table 7.I. Distribution of $(Si\text{-}O\text{-})_n$ rings on the surfaces of the eight voids.

Void case	n_3	n_4	n_5	n_6	n_7	n_8	n_9
1	0	0	3	2	5	3	0
2	0	0	1	5	1	2	0
3	1	2	4	3	4	1	1
4	0	2	1	2	3	2	1
5	0	0	1	5	3	1	0
6	0	0	1	5	1	2	0
7	0	1	2	5	2	2	0
8	0	2	1	4	3	0	0

The energy of the water dimer in a void relative to that of two isolated water molecules in two voids is $-0.3 - 0.0$ eV in the 0 % compressed system. During the gradual compression of the system by the hybrid QM-CL method, we observe competition between the escape of an H_2O to a neighboring void after dissociation of the dimer and the adsorption of H_3O^+ at Si after H-transfer within the dimer.

7.4.1 Cases with Si-O bond breakings

Among the 24 cases, Si-O bond-breaking reactions are found in cases 1y, 2z, and 6x. In all three cases, the reactions occur through the formation of H_3O^+ and OH^- via H-transfer between the two H_2O. Regarding the charge states, Mulliken's population analyses[34] show that they are $H_3O^{+\delta}$ and $OH^{-\delta}$ with $\delta \sim 0.5$ relative to two charge-

neutral H_2O in a void. Considering the intrinsic ambiguity of the analyses, we regard them as H_3O^+ and OH^-. In this subsection, we explain the three cases in detail. We find that the water assumes the form of $H_3O^+ + OH^-$ if the O-O distance is less than 2.6 Å [see Figure 7.7(b) later], which we call the H-transferred water dimer. Note that the O-O distance is 2.7 Å at equilibrium if the dimer is set in vacuum. The reaction $2H_2O = H_3O^+ + OH^-$ goes back and forth in a void in the present runs. When the O-O distance is between 2.6 and 3.5 Å, we call the state the water dimer. Otherwise, we refer to the state as water as monomers. The coordination number of a Si corresponds to the number of O atoms within a distance of 2.0 Å from the Si. The Si of the target Si-O bond is often five-coordinated as a result of the adsorption of the O of H_2O in addition to the original four O.

The time evolutions of the system in the three bond-breaking cases are as follows.

Case 1y: At $0.0-0.5$ ps, we observe the H-transferred water dimer and the five-coordinated Si. At $0.5-1.3$ ps, the water dimer state is seen. At $1.3-2.2$ ps, the H-transferred water dimer and the five-coordinated Si, which differs from the five-coordinated Si during $0.0-0.5$ ps, are seen. Figure 7.6(a) depicts the atomic configuration at 2.2 ps. At 2.3 ps, we find the reacted state of $\equiv$Si-OH HO-Si$\equiv$ $+ H_2O$ after the Si-O bond breaking, as depicted in Figure 7.6(b). Figure 7.7 shows the time evolutions of the interatomic distances, bond overlap populations, and O-Si-O angles to substantiate the scenario mentioned above. We judge that a bond is formed if the bond overlap population becomes larger than 0.5.

Case 2z: At $0.0-1.7$ ps, the water dimer is seen and sometimes the water monomers are seen. The H-transferred water dimer and the five-coordinated Si appear at $1.7-3.1$ ps. One of the four Si-O bonds of the Si, which is far from the water, is broken at 3.2 ps. Then the O of the broken Si-O bond forms a new O-Si bond with a surrounding Si maintaining twofold coordination. Finally, an O, which differs from the O of the originally broken Si-O bond, adsorbs H of H_3O^+ to form $\equiv$Si-OH HO-Si$\equiv$ $+ H_2O$.

Case 6x: At $0.0-1.6$ ps, the water monomers are seen. At $1.6-3.1$ ps, the H-transferred water dimer and the five-coordinated Si appear. At 3.1 ps, the reacted state of $\equiv$Si-OH HO-Si$\equiv$ $+ H_2O$ is formed in a similar manner to in case 1y.
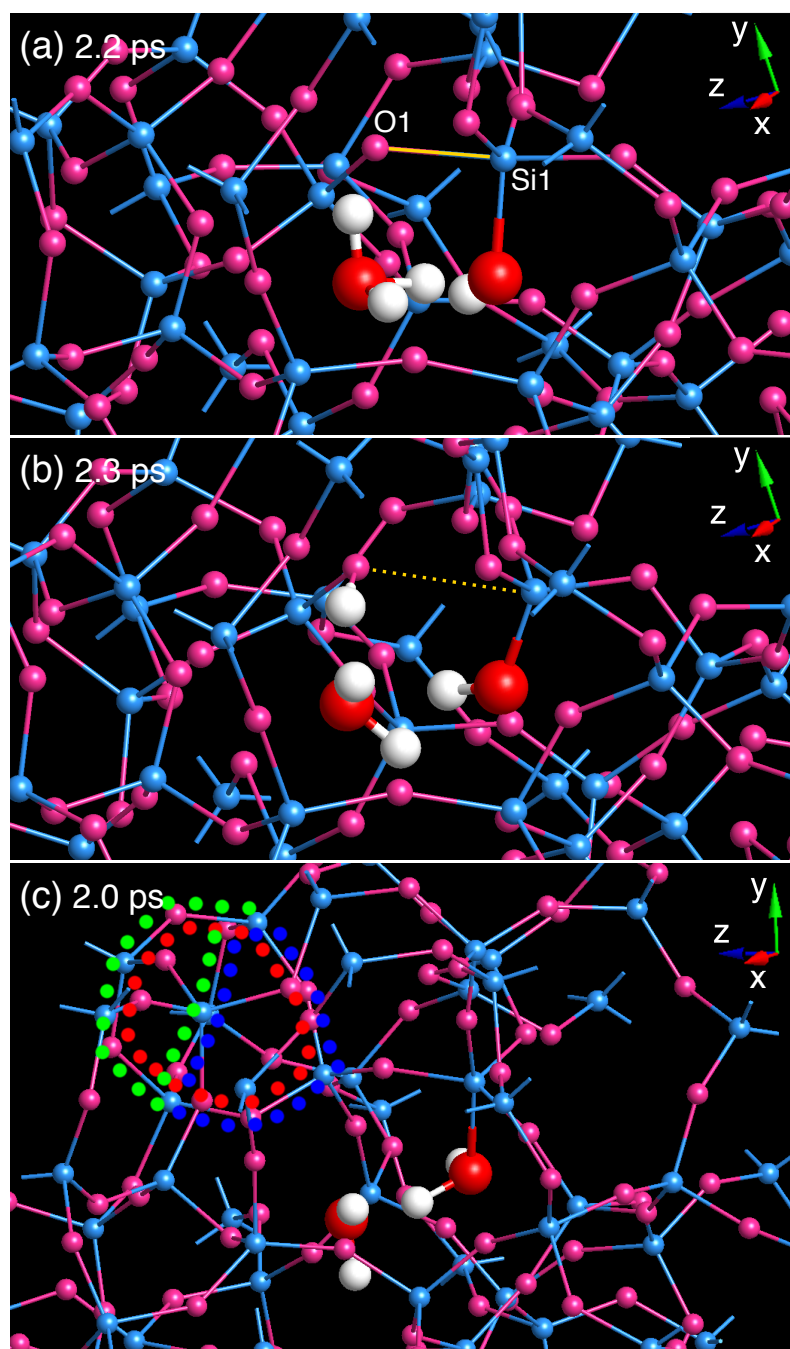
Figure 7.6. Snapshots in case 1y: (a) at 2.2 ps and (b) at 2.3 ps. (c) Zoom-out view at 2.0 ps depicting the complex of three $(Si-O-)_4$ rings adjacent to a five-coordinated Si.

In both cases 1y and 6x, the water dimer is converted to the H-transferred water dimer, *i.e.*, $OH^- + H_3O^+$, and then the O of OH^- adsorbs at a Si to form the five-coordinated Si. After that, within $1-2$ ps, the H of H_3O^+ transfers to the O bonded originally to the Si in accordance with Si-O bond breaking to form $\equiv$Si-OH HO-Si$\equiv$ $+ H_2O$. In case 2z, the five-coordinated Si forms in the same way. The Si is unstable and breaks a backbone Si-O bond that is not the closest to the H of H_3O^+. The Si-O bond breaking continues until the H of H_3O^+ transfers to the O of a broken bond. Although there are differences in terms of which of the four Si-O bonds breaks, essentially the same reaction mechanisms are observed in the three cases. Since an H_2O remains after the reaction, we may regard such an H_2O as a catalyst.

Observing the three cases, we state that all the following conditions need be satisfied for Si-O bond breaking by a water dimer to occur in a void: (i) a water dimer becomes OH^- and H_3O^+ after the H-transfer, (ii) a Si on the void surface is five-coordinated by the adsorption of OH^- and is therefore unstable, (iii) H_3O^+ is located close to such an unstable Si-O bond so that the H of H_3O^+ can transfer to the unstable O after Si-O bond breaking.

We find by a separate DFT calculation for the H-transfer in $2H_2O$ in vacuum that the energy increases monotonically as the distance r_{OH} between O of an H_2O and H of another H_2O decreases. In the LDA, the energies at $r_{OH} = 1.1$ and 1.0 Å are 1.3 and 1.9 eV larger, respectively, than the equilibrium value and 1.5 and 2.1 eV according to the GGA.[13] Therefore, the H-transferred state of $H_3O^+ + OH^-$ has little opportunity to exist in vacuum at an ordinary temperature of 400 K. The reason for our observation of the H-transfer in the present runs is that H_3O^+ and OH^-, respectively, adsorb to O and Si on the void surface when the H-transfer occurs and thereby decrease both the barrier energy and the energy of the H-transferred state. In fact, conditions (i) and (ii) are satisfied simultaneously in the present runs.

For condition (i), a water dimer in a void has considerable opportunity to satisfy this condition, particularly when the system is compressed because of the increased interaction between the dimer and the surrounding Si-O network. The five-coordination of Si under condition (ii) requires significant deformation of a SiO_4 unit from a regular tetrahedron, as depicted in Figure 7.7(d). Such a significant deformation tends to occur in a $(Si-O-)_n$ ring with $n = 6 - 9$ that resides next to a complex of small rings such as

(Si-O-)$_4$ when the system is compressed. This is because such a complex of smaller rings is stiffer than a larger ring and hence the concentration of strain occurs at the larger ring. In fact, as depicted in Figure 7.6(c) for case 1y, the Si-O bond that breaks is located adjacent to a complex of three (Si-O-)$_4$ rings. The realization of condition (iii) depends on the detailed structure of the Si-O network on the void surface. In case 2z, we found both a H-transferred water dimer and five-coordinated Si during $1.7-3.1$ ps; *i.e.*, conditions (i) and (ii) were satisfied. However, condition (iii) was not satisfied because the H_3O^+ adsorbed at an O far from the O of the target Si-O bond. Therefore, Si-O bond breaking did not occur.
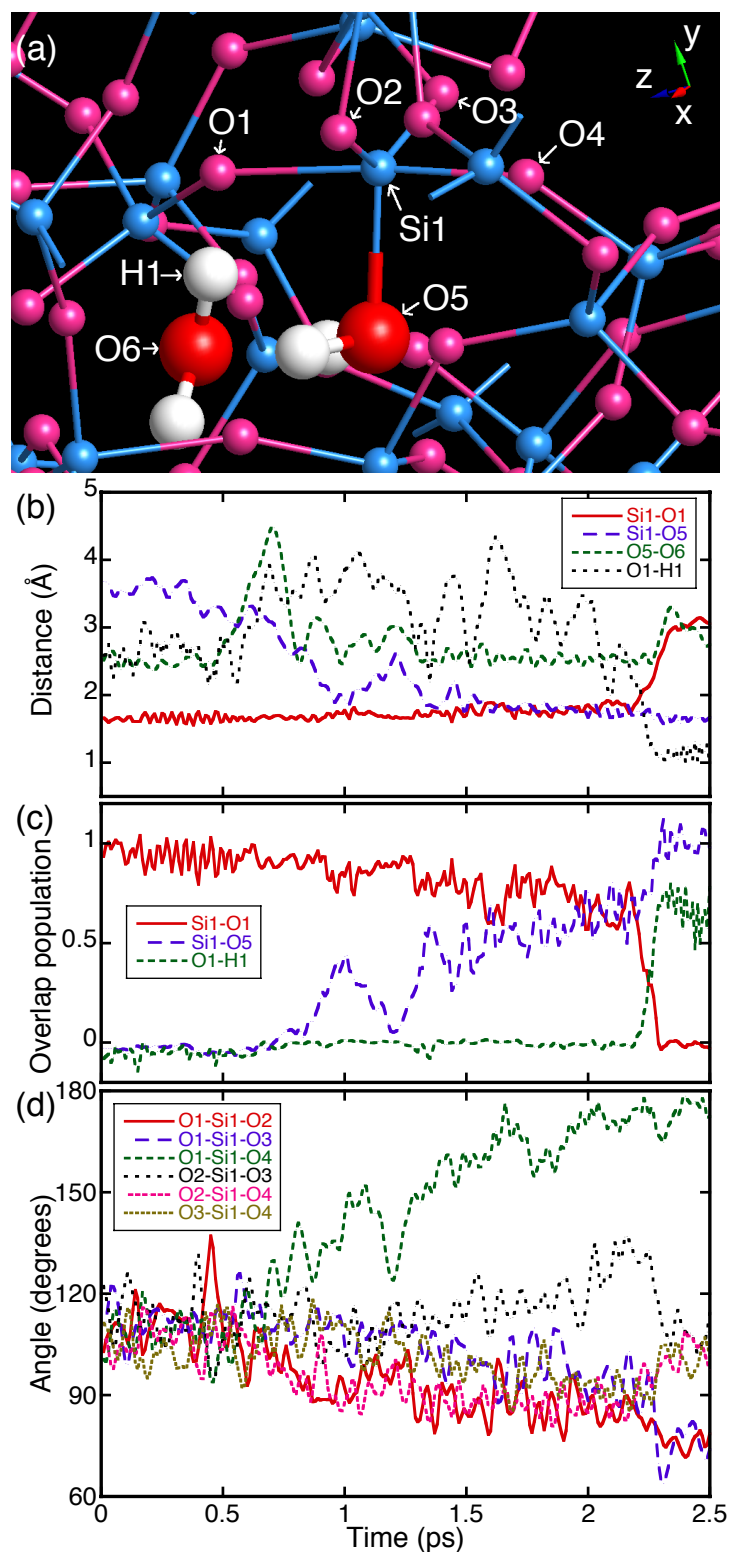
Figure 7.7. (Color online) Time evolutions of quantities in case 1y: (a) atom ID's at 2.15 ps, (b) interatomic distances, (c) bond overlap populations, and (d) O-Si-O angles.

No discussion of the preferred size of the $(Si\text{-}O\text{-})_n$ ring for the Si-O bond-breaking process with a water dimer has been found. On the other hand, calculations for the process with a water molecule have been reported. On the basis of a GGA-DFT calculation for a 72-atom silica glass, Van Ginhoven *et al.*[30] suggested that the process with a water molecule occurs not on small rings, such as $(Si\text{-}O\text{-})_3$ and $(Si\text{-}O\text{-})_4$, but on a ring adjacent to a small ring. Although the size of the system used in their calculations was much smaller than that in the present study, the idea that a ring adjacent to a small ring tends to react with water is in agreement with the present finding. Batyrev *et al.*[14] showed by a GGA-DFT calculation for a 72-atom silica glass that the heat of reaction of the process with a water molecule becomes positive (as large as 1 eV) owing to significant stress relaxation if a broken Si-O bond belongs to a $(Si\text{-}O\text{-})_3$ ring. However, we found no such Si-O bond breaking on small rings in the present simulation.

The present observation of Si-O bond breaking with a water dimer in a void at 400 K is in strong contrast to the case of no bond breaking with a water monomer. To understand the reasons for this different behavior, we separately analyze the energetics during Si-O bond breaking with a water dimer at 0 %, 5 %, and 10 % compressions. We adopt case 1y and calculate by DFT the energy as a function of the distance between the center of the target Si-O bond [O1-S1 in Figure 7.7(a)] and the O [O5 in Figure 7.7(a)] of the dimer similarly to in the monomer case. For a given value of the distance, we relax the remaining positional degrees of the atoms while taking care to avoid trapping in a local energy minimum by starting from various virtually shifted positions of the to-be-transferred H atom [H1 in Figure 7.7(a)].

We thereby find that the state $\equiv Si\text{-}OH\ HO\text{-}Si\equiv + H_2O$ is unstable and transforms barrierlessly to $\equiv Si\text{-}O\text{-}Si\equiv +$ (water dimer) at 0 % compression. Similarly to the monomer case in Section 7.3, this is because substantial energy (about 4 eV) is required at 0 % compression for the O of an H_2O to approach the central Si of a nearly regular SiO_4 tetrahedron. At 5 % compression, we find that the barrier energy is 0.10 eV and that it decreases further to 0.05 eV at 10 % compression. The heat of reaction is nearly zero: -0.11 and 0.12 eV at 5 % and 10 % compression, respectively. The initial and

near-transition states of the reaction at 10 % compression are depicted in Figure 7.8. Such small barrier energies in compressed situations resulted because the existence of another H_2O in close proximity to the H_2O assists the H-transfer. While the reaction is endothermic in the case of a water monomer, the reaction with a water dimer is nearly exothermic. We assume that this is for two reasons: the high energy of the dimer under compression owing to its large size in the initial state and the hydrogen bond formation between an H_2O and two Si-OH in the final state in the case of a dimer.
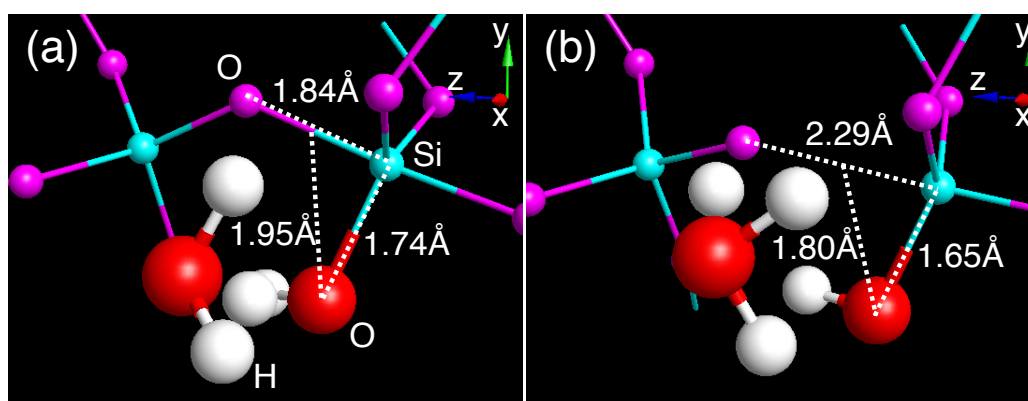

Figure 7.8. Zoom-in views of the atomic configuration in the Si-O bond-breaking reaction with a water dimer obtained by DFT in case-1y at 10 % compression. (a) for the initial state and (b) for the transition state.

7.4.2 Cases without Si-O bond breakings

In 21 out of the 24 cases examined by the hybrid QM-CL simulation in which a water dimer is inserted in a void of the present silica glass, no Si-O bond breaking is observed. We explain the reasons for this in the 21 cases. In about half the cases (cases 1x, 1z, 2x, 2y, 3x, 3y, 3z, 5z, 6y, 6z, 7x, and 8z; 12 cases in total), we find transitions between the water dimer and the H-transferred water dimer states until about 2.0 ps. As depicted in Figure 7.9 for case 1x, the OH^- of the H-transferred water dimer adsorbs at a Si [Figure 7.9(a)] on the void surface, but the H_3O^+ adsorbs at an O at the opposite side

to the Si on the void surface [Figure 7.9(b)], therefore no bond breaking occurs. This means that condition (iii) given in Section 7.4.1 is not satisfied.
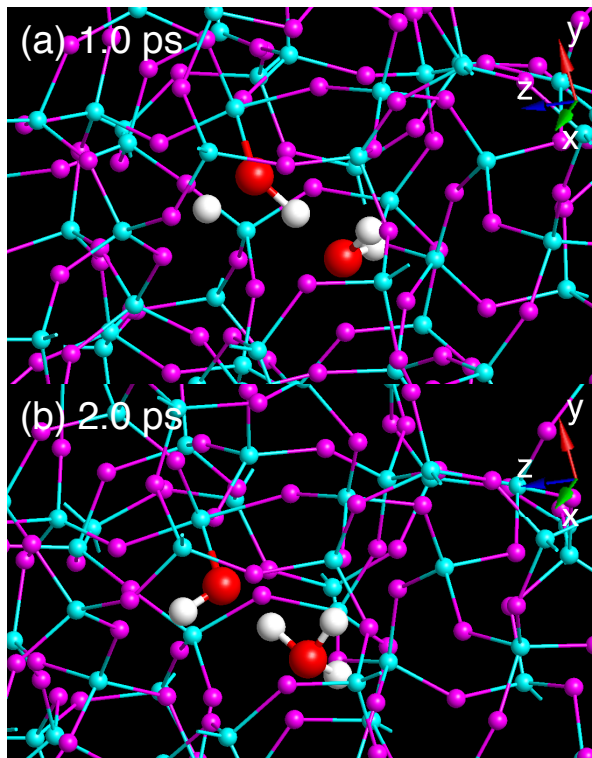

Figure 7.9. Snapshots in case 1x: (a) at 1.0 ps and (b) at 2.0 ps.

In the remaining nine cases with no bond breaking, a water dimer decomposes into two water monomers, and the monomers move within the void or diffuse into a neighboring void. A water monomer adsorbs at a Si on the void surface for a duration of about 1 ps. Hence, condition (i) in Section 7.4.1 is not satisfied. From the short times of the adsorbing state at 400 K, we assume that the adsorption energy of a water monomer is less than 0.1 eV even under high compression.

We also perform the hybrid QM-CL simulations with gradual expansion of the present silica glass. We find in all cases that a water dimer decomposes into two water monomers and that no Si-O bond breaking occurs. Condition (i) is thus not satisfied.

7.5 Discussion and Concluding Remarks

It has been suggested from the results of experiments[6,7] that water molecules migrate from a moist environment into silica glass through voids. To confirm this, we analyze the possible formation of a network of voids in the present silica glass. To identify the void network, we set virtual grid points in a simple cubic structure (the side of each cube is 0.2 Å). If no atom exists within a distance of 2.0 Å from a point, it is regarded as a void point. The value of 2.0 Å roughly corresponds to the interaction range between Si and O. Figure 7.10(a) shows the void points by yellow spheres in the sliced region $x =[0,30]$ Å, $y =[0,30]$ Å, and $z =[0,10]$ Å of the present silica glass (density of 2.18 g/cm^3). As we see in Figure 7.10(a), the void points form connected paths throughout the system, *i.e.*, a void network. In the case of α-quartz (density of 2.43 g/cm^3), the void points do not form connected paths throughout the system as shown in Figure 7.10(b). The size of a void in α-quartz appears to be smaller than that in the silica glass. A former GGA-DFT calculation[30] gave the insertion energy of a water molecule into a void of α-quartz as high as 1.2−1.5 eV, which supports the view given above. The existence of the void network in the present silica glass suggests that a water molecule can diffuse into the interior of silica glass. Two water molecules that diffuse in silica glass can form a dimer in a relatively large void (*i.e.*, positive formation energy).
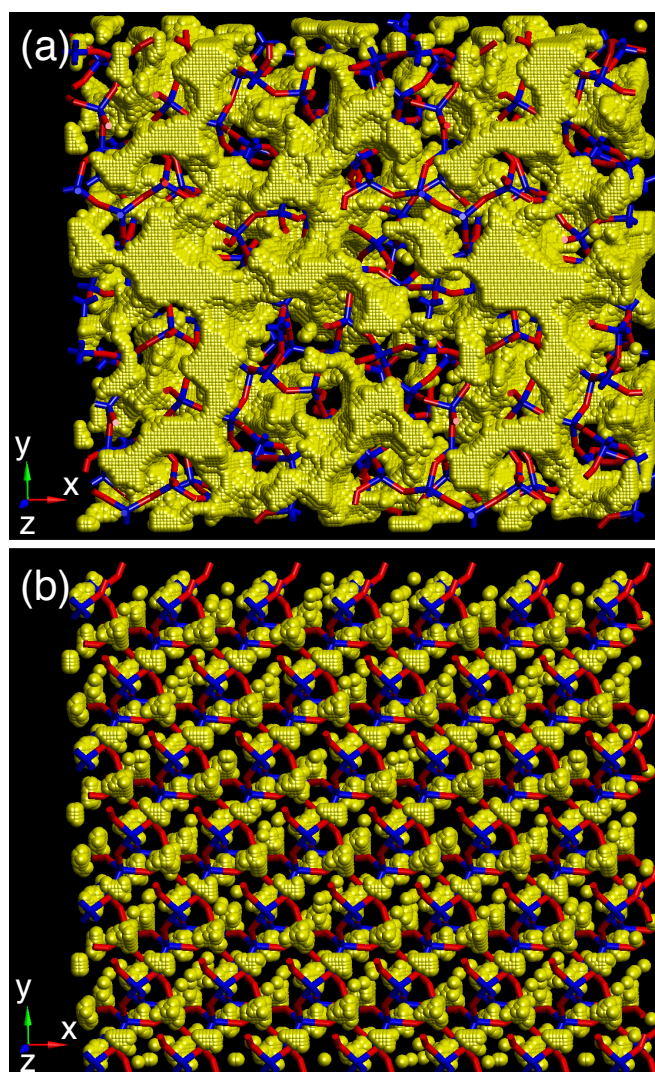
Figure 7.10. Void points plotted in yellow for (a) present silica glass and (b) α-quartz. The Si and O are drawn as bonds only.

To summarize this paper, we performed the hybrid QM-CL simulation of a 4,608-atom silica glass at 400 K with a water monomer or dimer inserted in a void. During a simulation run, the system was gradually compressed or expanded to analyze possible Si-O bond breaking involving the water. In the cases of a water monomer, we found that the water monomer moves to various locations within the void and that no Si-O bond-breaking reactions involving the water occur. In the cases of a water dimer, we found that Si-O bond breakings occur through three steps in 3 out of the 24 cases of compression:

(i) H-transfer as $2H_2O \rightarrow OH^- + H_3O^+$ accompanied by the adsorption of OH^- at a strained Si to make it five-coordinated, (ii) the breaking of a Si-O bond that originates from the five-coordinated Si, and (iii) H-transfer from H_3O^+ to the O of the broken Si-O bond. In two out of the three cases, steps (ii) and (iii) occurred instantaneously.

A separate DFT calculation confirmed that the barrier energy to bond breaking decreases when a SiO_4 unit is deformed from a regular tetrahedron by the compression of the system. The barrier energy of a water-induced reaction under compression is smaller in the case of a water dimer than in the case of a water monomer. In the case of a water dimer, the barrier energy decreases significantly and the heat of formation becomes exothermic when the silica glass is compressed further. We demonstrated the existence of a void network throughout the present silica glass, which suggests that a water molecule can diffuse into the interior of the silica glass. The principal finding obtained through the present simulation, that is, a Si-O bond in silica glass breaks easily in the presence of a water dimer when the silica glass is compressed, suggests that silica glass should not be set in a compressive situation, such as bending or local heating, in a moist environment when it is used for mission-critical applications.

1) M. Tomozawa, in *Silicon-Based Materials and Devices* ed. H. S. Nalwa (Academic Press, New York, 2001), Vol. 1, p. 127.

2) H. Hosono, in *Defects in SiO₂ and Related Dielectrics* ed. G. Pacchini (Kluwer Academic Publishers, Dordrecht, 2000), p. 213.

3) J. Senior, *Optical Fiber Communications: Principles and Practice* (Prentice Hall, New Jersey, 2008).

4) M. Shiozawa, T. Watanabe, R. Imai, M. Umeda, T. Mine, Y. Shimotsuma, M. Sakakura, K. Miura, and K. Watanabe, J. Laser Micro/Nanoeng. **9**, 1 (2014).

5) A. Deptuła, M. Miłkowska, W. Łada, T. Olczak, D. Wawszczak, T. Smolinski, F. Zaza, M. Brykala, A. G. Chmielewski, and K. C. Goretta, New J. Glass Ceram. **1**, 105 (2011).

6) K. M. Davis and M. Tomozawa, J. Non-Cryst. Solids **185**, 203 (1995).

7) K.M. Davis and M. Tomozawa, J. Non-Cryst. Solids **201**, 177 (1996).

8) T.A. Michalske and S.W. Freiman, Nature **295**, 511 (1982).

9) B. Lawn, *Fracture of Brittle Solids* (Cambridge University Press, New York, 1993), p. 172.

10) J. E. Del Bene, K. Runge, and R. J. Bartlett, Comput. Mater. Sci. **27**, 102 (2003).

11) T. Bakos, S.N. Rashkeev, and S. T. Pantelides, Phys. Rev. Lett. **88**, 055508 (2002).

12) T. Bakos, S.N. Rashkeev, and S. T. Pantelides, Phys. Rev. B **69**, 195206 (2004).

13) J. P. Perdew, K. Burke, and M. Ernzerhof, Phys. Rev. Lett. **77**, 3865 (1996); (Erratum) Phys. Rev. Lett. **78**, 1396 (1997).

14) I. G. Batyrev, B. Tuttle, D. M. Fleetwood, R. D. Schrimpf, L. Tsetseris, and S. T. Pantelides, Phys. Rev. Lett. **100**, 105503 (2008).

15) S. Ogata, E. Lidorikis, F. Shimojo, A. Nakano, P. Vashishta, and R. K. Kalia, Comput. Phys. Commun. **138**, 143 (2001).

16) S. Ogata, F. Shimojo, R. K. Kalia, A. Nakano, and P. Vashishta, Comput. Phys. Commun. **149**, 30 (2002).

17) S. Ogata, Phys. Rev. B **72**, 045348 (2005).

18) L. V. Woodcock, C. A. Angell, and P. Cheeseman, J. Chem. Phys. **65**, 1565 (1976).

19) P. Vashishta, R. K. Kalia, J. P. Pinó, and I. Ebbsjö, Phys. Rev. B **41**, 12197 (1989).

20) B. Vessal, M. Amini, and C. R. A. Catlow, J. Non-Cryst. Solids **159**, 184 (1993)

21) A. Takada, P. Richet, C.R.A. Catlow, and G.D. Price, J. Non-Cryst. Solids **354**, 181 (2008).

22) M. P. Allen and D. Tildesley, *Computer Simulation of Liquids* (Clarendon, Oxford, 1987).

23) T. Kouno and S. Ogata, J. Phys. Soc. Jpn. **77**, 054708 (2008).

24) S. Ogata, Y. Abe, N. Ohba, and R. Kobayashi, J. Appl. Phys. **108**, 064313 (2010).

25) N. Ohba, S. Ogata, T. Kouno, and R. Asahi, Comput. Mater. Sci. **108**, 250 (2015).

26) M. C. Payne, M. P. Teter, D. C. Allan, T. A. Arias, and J. D. Joannopoulos, Rev. Mod. Phys. **64**, 1045 (1992).

27) N. Ohba, S. Ogata, T. Kouno, T. Tamura, and R. Kobayashi, Comput. Phys. Commun. **183**, 1664 (2012).

28) S. Ogata, N. Ohba, and T. Kouno, J. Phys. Chem. C **117**, 17960 (2013).

29) N. Troullier and J. L. Martins, Phys. Rev. B **43**, 1993 (1991).

30) R. M. Van Ginhoven, H. Jónsson, B. Park, and L. R. Corrales, J. Phys. Chem. B **109**, 10936 (2005).

31) K. P. Driver, R. E. Cohen, Z. Wu, B. Militzer, P. López Ríos, M. D. Towler, R. J. Needs, and J. W. Wilkins, Proc. Natl. Acad. Sci. U. S. A. **107**, 9519 (2010).

32) H. J. C. Berendsen, J. P. M. Postma, W. F. van Gunsteren, A. DiNola, and J. R. Haak, J. Chem. Phys. **81**, 3684 (1984).

33) K. Muralidharan, J. H. Simons, P. A. Deymier, and K. Runge, J. Non-Cryst. Solids **351**, 1532 (2005).

34) R. S. Mulliken, J. Chem. Phys. **23**, 1833 (1955).

Acknowledgment

First and foremost, I would like to thank my supervisor, Professor Shuji Ogata, for his guidance throughout my studies. I appreciate that you gave me the opportunity to summarize my studies. I wish to thank Assistant Professor Ryo Kobayashi, Assistant Professor Tomoyuki Tamura, and the members of Ogata Laboratory in Nagoya Institute of Technology for helpful discussions.